Imaging clusters and their dynamics with single-shot coherent diffraction

Alessandro Colombo
ETH Zürich, John-von-Neumann-Weg 9, 8093 Zürich, Switzerland
alcolombo@phys.ethz.ch

Daniela Rupp
ETH Zürich, John-von-Neumann-Weg 9, 8093 Zürich, Switzerland
ruppda@phys.ethz.ch

in *Structural Dynamics with X-ray and Electron Scattering*
ed. K. Amini, A. Rouzée, and M. J. J. Vrakking

Coherent Diffraction Imaging with short-wavelength free-electron lasers has opened up the possiblity to determine the structure of especially fragile, short-lived or unique nanoscale particles within a single irradiation. It also has enabled novel approaches for investigating intense laser-matter interaction with unprecedented spatial and temporal resolution. Atomic clusters are ideal model systems for such investigations, thanks to their simple electronic structure and their highly controllable composition and morphology. This chapter aims at providing a comprehensible, but comprehensive, introduction to the research field of Coherent Diffraction Imaging of clusters, carrying the reader through the details of single-shot single-particle coherent diffraction experiments, the fundamental building blocks of the data analysis and the theoretical foundations for the interpretation of the results. The discussion is accompanied with references to the most up to date scientific works and reviews on the different topics, with a final focus on the promising outlook of coherent diffraction imaging of clusters with intense attosecond pulses.

5.1 Introduction

Diffraction before destruction[151,39] has been a key vision driving the development and construction of extreme ultraviolet (XUV) and X-ray Free-Electron lasers (FELs; see Chapter 8)[193,61,5,102,50,107,144]. Here, an interference pattern of a single, free-standing molecule from a single illumination with an intense X-ray pulse is recorded (see Figure 5.1).

The pulse is intense enough to measure a diffraction pattern with sufficient signal-to-noise ratio for retrieving the molecule's structure, and at the same time short enough to outrun the rapid destruction of the molecule due to ionization and charge-driven explosion following X-ray irradiation.

The quest for imaging single free molecules and the concept of diffraction before destruction have attracted widespread attention because of the large number of very important "soft-matter" molecules with crucial roles in life-sciences, such as membrane proteins, for which the standard way of crystallization and subsequent synchrotron-based X-ray diffraction is not feasible[7]. Furthermore, the "snapshot" technique of CDI can be utilized in pump-probe measurements, making photoexcited dynamics in molecules directly visible[35], such as the first steps of photosynthesis or the molecular mechanisms of vision. Structure determination of bio-samples at FELs has been both a story of success and great challenges[7]. Single viruses, cell organelles and bacteria were successfully imaged[201,89,228] and hundreds of new molecular structures have been determined *via* serial femtosecond nanocrystallography[38,74,235], in particular a large number of previously inaccessible membrane proteins[a]. The first single-shot single-molecule diffraction patterns, however, could be obtained only very recently[58], and they are still far too weak to provide atomic resolution. The first simulations of single-molecule CDI[151] over two decades ago had already predicted challenging requirements for pulse parameters in terms of intensity and duration, which have come into reach only recently[55,167]. The pioneering theoretical study[151] and subsequent work[93,92,149,213] also indicated that "ultrafast radiation damage" would be a main bottleneck of single-molecule CDI, and in accordance, intense X-ray matter interaction has been in the focus of XFEL science from the very beginning.

Atomic clusters have served as prototypical model systems with tunable size and complexity in intense light-matter interaction studies throughout all wavelength regimes. They have also played an important role in developing our current understanding of the intricate processes triggered in any matter at the focus of an intense X-ray pulse. In particular, experiments on single clusters have pushed the field far beyond the mere study of radiation damage. For the first time, the exact structure of fragile and non-depositable gas-phase clusters and nanodroplets can be determined. Also, near-background free spectroscopy from clusters, resolved for cluster size and laser power density, became possible through single-cluster CDI (see concept in Figure 5.2).

Arguably, the most exciting aspect is imaging laser-induced dynamics in single clusters through "X-ray movies", yielding unprecedented insight into highly excited matter on the

[a] `https://blanco.biomol.uci.edu/mpstruc/`

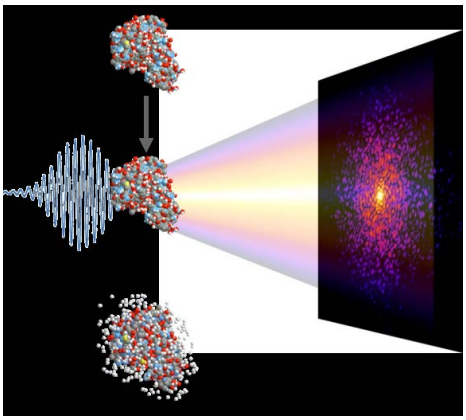

Figure 5.1: Concept of *Diffraction before Destruction*. A single protein in free flight is intercepted by an intense coherent X-ray pulse. The diffracted light, captured with a large-area detector, is sufficiently bright for decoding the molecule's structure. The molecule explodes quickly, but the pulse is already over when atomic motion sets in. Molecules reprinted from Reference [151] with permission from Springer Nature, Copyright 2000.

nanoscale. In this regard, the current development of intense attosecond pulses from FEL and HHG sources around the world[55,136,17,152] opens up an exciting opportunity. The realm of electron dynamics is reached, a perspective discussed at the end of this chapter.

The heart of this chapter is a step-by-step introduction into the theory behind the imaging method (see Section 5.2). Here, we aim at providing a solid starting point for students and scientists interested in CDI experiments at FELs. We introduce the fundamental building blocks of the imaging problem, familiarize the reader with available imaging strategies, and point out common practical pitfalls, often overlooked by scientific literature. In terms of applications, will emphasize recent results and novel opportunities for single cluster CDI, while giving concise summaries elsewhere, as actual reviews exist on the CDI method[109,64,134,207,153,222], bio-applications of CDI[201,57,35,212,150,186], CDI of helium nanodroplets[220,209], and cluster science at FELs[33,104].

5.2 A gentle introduction to single-shot single-particle Coherent Diffraction Imaging

Coherent Diffraction Imaging (CDI) is an experimental technique that images isolated samples by collecting their scattering signal. The most common way in which the term imaging is intended is the so-called *direct* imaging, like for optical or electron microscopes up to telescopes. There, the lenses in the experimental apparatus are responsible for

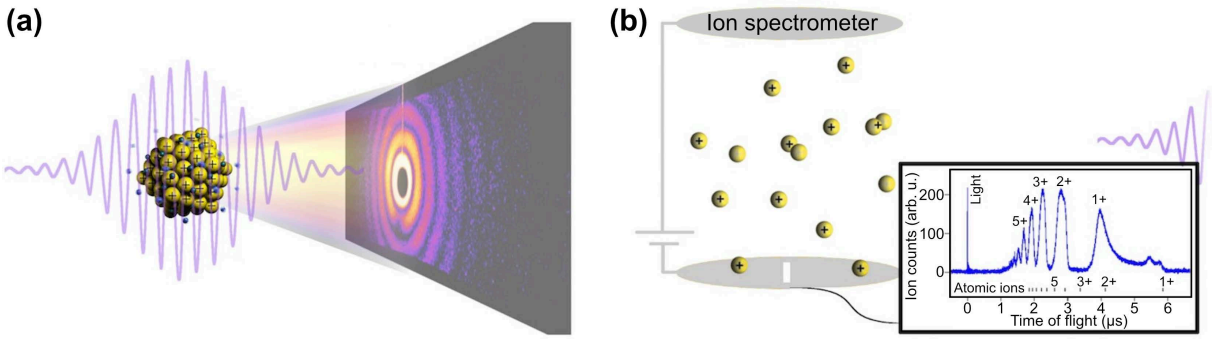

Figure 5.2: Combined single-cluster CDI and ion spectroscopy. (a) The interaction of a cluster with a short-wavelength pulse produces a diffraction pattern encoding the cluster size and focal intensity. (b) The cluster is also excited and highly ionized, and it ultimately disintegrates. Measured ion time-of-flight spectra from single clusters can be sorted by the diffraction information. An exemplary ion time-of-flight spectrum of a single xenon cluster shows that high charge states up to 5+ are clearly separable even though the ions posses high kinetic energies.

directly providing an image[b] (and thus spatial properties) of the sample.

However, when *imaging* is employed with the term *diffraction*, the perspective changes. CDI is a *lens-less* imaging technique, whereby no lenses are used in the experiment. This makes CDI the method of choice for those measurements which cannot use lenses, like in the case of XUV and (soft) X-ray FELs. The side-effect of the absence of lenses is that the radiation recorded by the detector is no more a direct visualization of the sample's spatial distribution. This renders CDI an *indirect* imaging technique: the sample's image is retrieved by means of sophisticated analysis methods, which play the role of *virtual lenses*.

5.2.1 The inverse scattering problem

The theory behind CDI can be conveniently introduced through a simplified view on light-matter interaction, which can be easily described in a semi-classical way. When light interacts with a sample, the oscillating electric field drives the material's electrons. In response, the electrons become emitters of spherical waves that are coherent with the incoming light. This simple view[c] describes a completely *elastic scattering*, as the photon energy is conserved during the scattering event. The coherent fields scattered by the

[b] In a broad sense. For light scattering, this is usually related to the electronic density distribution. A different example is Transmission Electron Microscopy, where the "image" reveals the atomic potential.

[c] Going into the details of light-matter interaction and scattering is beyond the scope of this chapter. We warmly recommend References [24] and [158] for insights into first principles, and References [82] and [239] for the link to diffraction theory.

emitters at different locations in space interfere, giving rise to the diffraction pattern. In a CDI experiment, light is recorded in the so-called *far-field* condition, which depends on the sample spatial extension and on the employed radiation wavelength. The validity of this condition is not a concern for CDI experiments in the X-ray regime[37], as explained in Reference [109]. We can state that the field $\Psi(\vec{q})$ scattered by a sample seen in *far-field* is given by:

$$\Psi(\vec{q}) \propto \int \mathrm{d}\vec{r}\, \rho(\vec{r})\, e^{i\vec{q}\cdot\vec{r}} \tag{5.1}$$

Here, $\rho(\vec{r})$ can be addressed as the *scattering density*, which tells, in a first approximation, the number of scatterers (electrons) present at a given location in space $\vec{r}$. The coordinate $\vec{q}$ is called *momentum transfer* and, roughly speaking, provides the direction in which the light is emitted. Equation 5.1 is based on the Born approximation[25,109], which assumes that light travelling through the sample is not affected by sample material, apart from the single scattering event (see Section 5.2.3). In practice, Equation 5.1 gives the scattered field as function of the momentum transfer $\vec{q}$ as nothing more than the three-dimensional Fourier Transform of the *scattering density* $\vec{\rho}$. The field $\Psi(\vec{q})$ is not experimentally accessible, and only its intensity $I(\vec{q})$ can be measured, given by

$$I(\vec{q}) = |\Psi(\vec{q})|^2 \propto \left|\mathcal{F}_{3\mathrm{D}}\left[\rho(\vec{r})\right](\vec{q})\right|^2 , \tag{5.2}$$

where $\mathcal{F}_{3\mathrm{D}}$ denotes the Fourier transform in the three-dimensional spatial domain. Second, only monochromatic light is employed[d], which implies that a small fraction of the reciprocal coordinates $\vec{q}$ are experimentally accessible, as the recorded data is a two-dimensional surface in the 3D Fourier domain. The relationship between the recorded data and its coordinates in the reciprocal space is sketched in Figure 5.3a. The momentum transfer $\vec{q}$ is defined as the difference between the wavevector of the incident light $\vec{k}_0$ and the wavevector of the scattered light $\vec{k}$ at a given scattering angle[e] θ, *i.e.* $\vec{q} = \vec{k}_0 - \vec{k}$. Thanks to the *elastic* nature of the scattering process, the photon energy is conserved, implying $\left|\vec{k}_0\right| = \left|\vec{k}\right|$. As a consequence, the accessible momentum transfer lie on a spherical surface in the Fourier domain, referred to as *Ewald sphere* (see right of Figure 5.3a for a 3D render of the Ewald sphere).

It is convenient to separate the momentum transfer $\vec{q}$ into two components. One component is $\vec{q}_\perp$, perpendicular to the beam propagation direction. The second component $\vec{q}_\parallel$ is instead parallel to the beam. Their values can be expressed as function of the scattering angle θ:

$$|\vec{q}_\perp(\theta)| = |\vec{k_0}|\sin(\theta) \qquad \left|\vec{q}_\parallel(\theta)\right| = |\vec{k_0}| \cdot [1 - \cos(\theta)] \tag{5.3}$$

When the scattering angle reached by the light detector is sufficiently large (see example shown in Figure 5.3) the curvature of the Ewald sphere allows to record significant infor-

[d]The monochromatic assumption is valid in most cases. However, polychromatic[133] or broadband[236] pulses are also employed for some applications, which are not discussed in this section.

[e]Warning: in some contexts, and especially in crystallography, this angle is often called 2θ, where theta is the Bragg angle. Here, we call scattering angle θ the quantity equivalent to twice the Bragg angle.

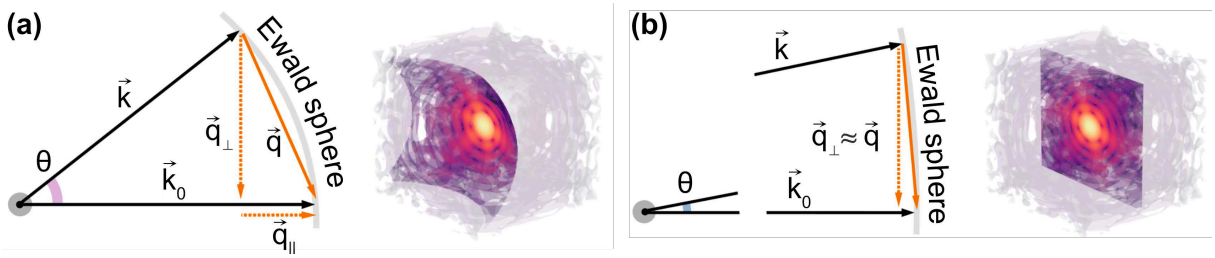

Figure 5.3: Geometry of monochromatic elastic scattering. a) Relevant quantities in reciprocal space; incoming wavevector $\vec{k}_0$, scattered wavevector $\vec{k}$ for a given scattering angle θ and respective momentum transfer $\vec{q}$ with parallel component $\vec{q}_\parallel$ and orthogonal component $\vec{q}_\perp$. Right: portion of the Fourier domain accessible *via* monochromatic light scattering, commonly known as Ewald sphere. b) *Small-angle* scattering regime: the parallel component of the momentum transfer $\vec{q}_\parallel$ is negligible. The portion of the Fourier domain experimentally accessible can be approximated by a plane passing through the origin of the reciprocal coordinates.

mation both on the orthogonal plane and on the axis parallel to the beam. This regime is known as *wide-angle* scattering, where partial 3D information is recorded in a single shot.

The situation drastically changes in the so-called *small-angle* scattering regime (see sketch in Figure 5.3b). In such a case, the scattering angle is small enough to neglect the parallel component of the momentum transfer $\vec{q}_\parallel(\theta)$. In practice, this means that the portion of the Ewald sphere accessible by the detector is small enough to approximate it to a flat slice, orthogonal to the beam propagation direction and passing through the origin of the Fourier domain. It is then possible to take advantage of the *Fourier slice theorem*, which is a well-known "trick" in the field of Computational Tomography. Brought into the CDI framework, it allows to implement the following: as long as the recorded data is lying on the plane orthogonal to the beam ($\perp$) in Fourier space, the values on the slice are the 2D Fourier Transform of the scattering density ρ projected onto the beam propagation axis ($\parallel$). In mathematical form, this means:

$$\mathcal{F}_{3D}\left[\rho(\vec{r})\right](\vec{q}_\perp, q_\parallel = 0) = \mathcal{F}_{2D}\left[\int_\parallel \rho(\vec{r})\right](\vec{q}_\perp) \tag{5.4}$$

Thus, the actual data recorded by the detector in the small angle case (*i.e.* the amplitude of the scattered field on the orthogonal plane $I(\vec{q}_\perp)$) can be expressed as

$$I(\vec{q}_\perp) \propto \left|\mathcal{F}_{2D}\left[\rho_{2D}(\vec{r}_\perp)\right](\vec{q}_\perp)\right|^2 , \tag{5.5}$$

where $\rho_{2D}(\vec{r}_\perp)$ denotes the projection of the scattering density in parallel direction. Due to the low scattering angle θ the recorded parallel component of $\vec{q}$ vanishes (see Equation5.3). As $\vec{q}_\parallel$ carries information in beam propagation direction (*i.e.* on the sample *depth* information), the spatial distribution on the depth direction is, then, lost when only $\vec{q}_\parallel = 0$ is accessible.

Equations 5.2 and 5.5 are a concise solution to the *direct scattering problem*, where the scattered field Ψ (or its amplitude I) is computed from the knowledge of the scattering density ρ. However, the aim of CDI is to approach the riddle from the opposite direction and retrieve the scattering density ρ from the scattered field amplitude I. This is called the *inverse scattering problem*, and they way in which it can be approached strongly differs between the *wide-angle* and *small-angle* regimes. For *wide-angle* scattering, partial 3D information information about ρ is accessible. However, its main drawback is that the retrieval of the 3D sample structure is highly challenging, as it will be discussed in Section 5.2.3. On the other hand, *small-angle* diffraction data only give access to a 2D projection of scattering density ρ as suggested by Equation 5.5. Nevertheless, established methods for the retrieval of the density projection ρ exist since many years, and already proved their consistency and effectiveness. The next section will provide an introduction to these algorithmic methods, giving insights into what can be addressed as the virtual *lenses of small-angle CDI*: phase retrieval algorithms.

5.2.2 Small-angle Coherent Diffraction Imaging

To approach the topic from the *imaging* perspective, it is convenient to reformulate Equation 5.1, which present a solution to the *direct scattering problem*, in its *inverse* form for the small angle case, by taking advantage of the Fourier Slice Theorem

$$\rho(x, y) = \mathcal{F}^{-1}\left[\Psi(q_x, q_y)\right](x, y)\,, \tag{5.6}$$

where $\mathcal{F}^{-1}$ indicates the operation of Inverse Fourier Transform (IFT)[f].

As mentioned in the previous section, only information about the modulus of Ψ is experimentally accessible (*i.e.* $|\Psi| = \sqrt{I}$ where I is the field intensity recorded by the scattering detector). The field phases ϕ are irretrievably lost[g] in the measurement process. It is then convenient to rewrite Equation 5.6 by explicitly separating the modulus and phase components of the scattered field as it follows:

$$\rho(x, y) = \mathcal{F}^{-1}\left[\sqrt{I(q_x, q_y)}e^{i\phi(q_x, q_y)}\right](x, y) \tag{5.7}$$

As long as we trust the fact that any function has a unique Fourier representation (*i.e.* the Fourier domain is a *complete* basis), Equation 5.7 makes it clear that, for *small-angle CDI*, retrieving the phases $\phi(q_x, q_y)$ is equivalent to recovering the scattering density ρ. This is the reason why, in this context, the *inverse scattering problem* is often called the *phase retrieval problem*[175,207,64].

[f]Here, we introduce some changes in the mathematical notation that will be valid along the full section. From now on, the spatial coordinates will only refer to the 2D orthogonal plane, indicated as x, y for the real space and q_x, q_y for the Fourier domain. Furthermore, the Fourier Transform (FT) operation $\mathcal{F}$ acts in the two-dimensional space. Please, also note that we replaced the term $\propto$ with $=$ for the sake of simplicity.

[g]Why are phases lost? To keep it short, detectors measure photon counts, which are proportional to the square field modulus. Are they really irretrievable? Not really, keep on reading.

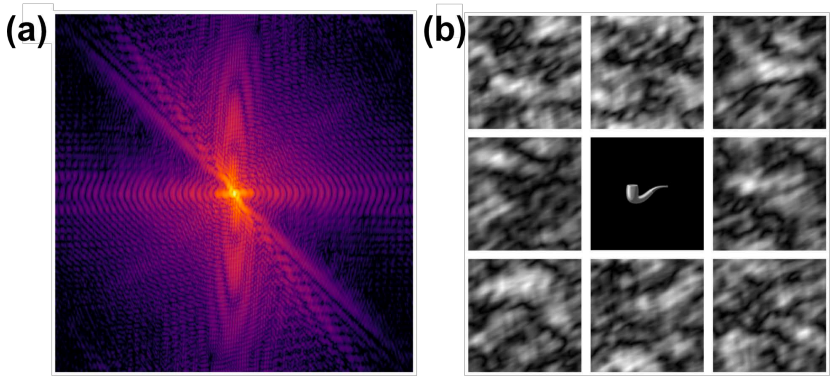

Figure 5.4: The role of the field phases. (a) Simulated diffraction pattern in logarithmic color scale, representing the only experimentally accessible data. (b) All but the central picture are obtained by assigning random phases to the diffraction pattern in (a), and then inverting the field to obtain a spatial distribution by performing an inverse FT. The central picture in (b) is instead the original image (*i.e.* with the *correct* phases) from which the simulation in (a) was calculated.

There are several ways to intuitively evaluate the amount of information carried by the field's phase[h]. Here, we try to address this point by studying the result of a random assignment of the phases values in the reciprocal space. In this regard, we temporarily leave the formal mathematical treatment of the scattering problem and directly dive into its numerical translation[i]. The first numerical implementation performs a *direct scattering* simulation, following Equation 5.5. The scattering density $\rho(x, y)$ is encoded into a matrix `rho[i,j]`. The simulation is numerically achieved by performing a Discrete Fourier Transform (DFT) on the matrix `rho[i,j]`, and then computing its squared absolute value, as described by the following script:

```
# The import of the numpy library is necessary for complex mathematical
    operations
# like the DFT. This line will be omitted in the next code listings
import numpy as np

def get_simulated_pattern(rho):
  # Calculate the 2D DFT of the input data, and shift the frequency
    domain
```

[h] And it turns out that the amount of information provided by the Fourier phases is actually even more than the one from the amplitudes, as nicely investigated in Reference [143].

[i] The numerical examples will be presented in Python3 language, due to its clarity and popularity. Readers not familiar with Python language shouldn't be afraid, as the examples provided here will be easily understandable without any specific Python knowledge, and all numerical operations will be exhaustively commented. The presented scripts are not to be intended as full standalone scripts, but just snippets for a practical understanding of numerical operations.

```
  # to have the (0,0) component in the centre
  field = np.fft.fftshift(np.fft.fft2(rho))
  # Calculate the diffraction pattern as the square modulus of the
   scattered field.
  pattern = np.abs(field)**2
  return pattern
```

This operation produces a two-dimensional matrix, of the same size as the input matrix `rho`, which provides a simulated diffraction pattern (*i.e.*, a solution to the *direct scattering problem*). A possible output of this function is shown in Figure 5.4a. We can visualize in real space the effect of assigning random phases to the diffraction pattern *via* the following script:

```
def assign_random_phase(pattern):
  # Create a matrix of random numbers between -pi and pi, of size equal
  # to the pattern matrix
  phases = np.random.uniform(-np.pi, np.pi, size = pattern.shape)
  # Create a field that combines the input pattern with random phases
  field = np.sqrt(pattern) * np.exp(1j*phases)
  # Compute the real-space image by inverting the field via an inverse
   DFT,
  # after having shifted the frequencies back
  rho = np.fft.ifft2(np.fft.fftshift(field))
  return rho
```

Possible outputs of the `assign_random_phase` function are shown in Figure 5.4b together with the original density placed in the centre. There are two key that are apparent in Figure 5.4b. First, any information about the overall shape of the pipe and its main features is completely lost when phases are randomly assigned. It is then possible to create an infinite amount of $\rho(x, y)$ having the same diffraction pattern, but have completely different real-space representations. This already suggests that further information is needed to address the *phase problem*. The second observation already hints towards which type of information could be employed. In fact, all the scattering densities produced with a random assignment of phases have non-zero values spread around the full matrix `rho`, while only the *correct* density is spatially confined to a specific region of the real space.

This confined space is described, in this context, as a *support function*. The support function is numerically implemented as a binary function, which can assume only two values, 0 and 1 (see Figure 5.5a). It is worth noting that it is possible to create an infinite amount of spatial densities that are "contained" in a support function (see Figures 5.5b-d), similarly to the considerations made about Figure 5.4. However, it can be mathematically proven[86] that a *unique* solution[j] to the *phase retrieval problem* exists if and only if the original scattering density is *spatially confined*[k,192,139]. We can then state that:

[j]The *unicity* of the solution has to be interpreted in a broad sense, as there are, in practice, many ambiguous solutions. However, this aspect will be discussed later to avoid interruptions of the discussion thread.

[k]Technically, this spatial confinement is required to satisfy the *oversampling condition*, such that the

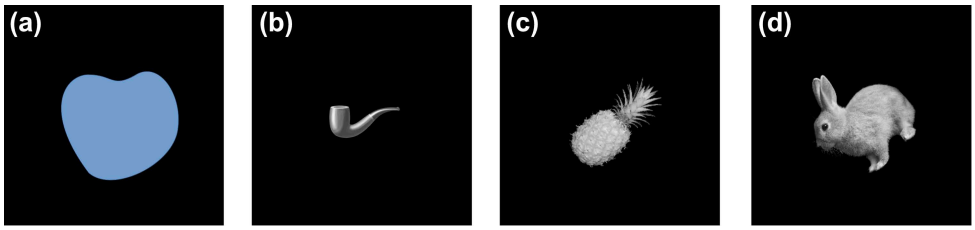

Figure 5.5: The support function. In a), a possible *support function* is shown. In b), c) and d), three different spatial distributions compatible with the support function in a). It can be demonstrated that only one of them can have the same diffraction pattern shown in Figure 5.4 (guess which one).

> *There exists only one spatially confined scattering density with a given Fourier amplitude, which represents the solution to the phase retrieval problem.*

Once we "proved" that, under the given conditions, a solution exists[86,64], the next step is to find it (*i.e.* to actually *solve* the *phase problem*). Solving the phase problem means finding the density distribution ρ_{sol} that is spatially confined and whose Fourier amplitude is compatible with the experimental diffraction pattern. For an easier and more intuitive understanding, it is now convenient to change the perspective from which we look at the problem, and describe it in terms of two *sets*[60,129,134] (see Figure 5.6).

The set I (see green shaded in Figure 5.6) is the collection of all spatial distributions that are compatible with the diffraction pattern (*i.e.* whose squared Fourier amplitude is equal to the scattering data shown in Figure 5.4a). Then, all densities in Figure 5.4b belong to the set I. On the other hand, the collection of all the densities which are compatible with a given *support function* (like the one shown in Figure 5.5a) is referred to as set S (pink shaded in Figure 5.6). Densities in Figures 5.5b-d all belong to such a set. The solution to the phase problem can be now visualized as the intersection between the sets I and S. The expression

$$\mathsf{I} \cap \mathsf{S} = \{\rho_{\text{sol}}\} \tag{5.8}$$

is equivalent to stating that the solution ρ_{sol} is unique. Now that the phase problem and its solution have been defined, strategies to find such a solution will be discussed.

Phase retrieval algorithms

Following Equation5.8, the solution to the phase problem must satisfy both the *intensity constraint* and the *support constraint*. The first step in solving the phase problem is to define an effective way to *apply* these constraints to a generic density distribution ρ.

spatial extension of the support function is, in pixels, not greater than half the size of the full matrix. Jump to Section 5.2.2 for further considerations

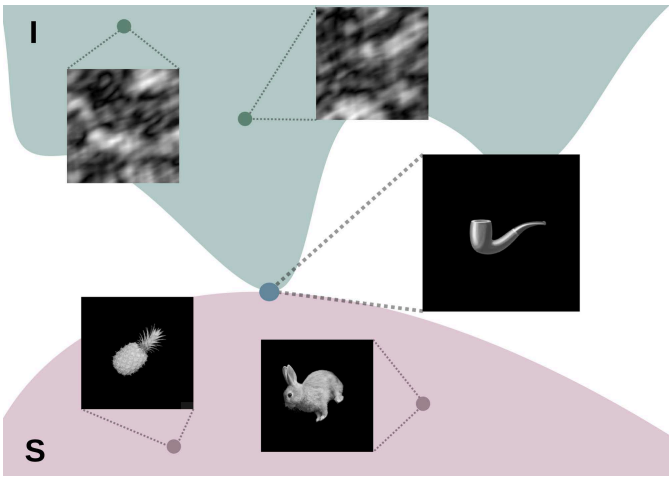

Figure 5.6: Qualitative representation of the phase problem in terms of sets. The 2D coordinates in the picture have to be interpreted as a low-dimensional representation of the values of the density ρ. A point in this space corresponds to a given combination of pixel values (*i.e.* to a well defined density matrix). The green set, labelled as I, in the upper part of the figure contains all the density distributions that have the same Fourier intensities, as those shown in Figure 5.4b. The pink set S is, conversely, the collection of all spatial distributions that have non-zero values only within the support function, as the ones shown in Figure 5.5. Theoretically, the intersection between the sets contains a single element (here, represented by the pipe) which is the solution to the phase retrieval problem.

For the intensity constraint, we define the operator P_{I} which acts on a generic spatial density ρ, given by

$$P_{\mathsf{I}}\,\rho = \mathcal{F}^{-1}\left[\sqrt{I}\frac{\tilde{\rho}}{|\tilde{\rho}|}\right], \tag{5.9}$$

where $\tilde{\rho} = \mathcal{F}[\rho]$[1]. The operator P_{I} acts on a density function ρ by calculating its Fourier transform $\tilde{\rho}$, replacing its modulus with the experimental one $\sqrt{I}$, and performing an inverse FT back to the real space. For any density ρ, the result $P_{\mathsf{I}}\,\rho$ belongs to the set I. On the other hand, the operator P_{S} acts on a generic spatial density ρ as

$$P_{\mathsf{S}}\,\rho = \rho \cdot S\,, \tag{5.10}$$

where S is the support function, whose values are $S(x,y) = 1$ for those spatial coordinates where the density is allowed to have non-zero values (for example, see the blue area in Figure 5.5), or $S(x,y) = 0$ elsewhere. Similarly to what is observed for P_{I}, the result of $P_{\mathsf{S}}\,\rho$ belongs to the set S for any density ρ. The most straightforward numerical implementation of the operators P_{I} and P_{S} is given below:

[1]For the sake of brevity, the dependence on the spatial coordinates x, y for real-space functions and on the reciprocal coordinates q_x, q_y for functions in Fourier domain has been omitted.

```python
def P_I(rho, modulus):
  # Compute the field of rho
  field = np.fft.fftshift(np.fft.fft2(rho))
  # Replace the current Fourier modulus with the experimental data
  field_new = modulus * field/np.abs(field)
  # Compute the real-space density with the upgraded field.
  rho_new = np.fft.ifft2(np.fft.fftshift(field_new))
  return rho_new

def P_S(rho, support):
  # Compute the real-space density with the upgraded field.
  rho_new = rho * support
  return rho_new
```

It is now worth noting that the two operators in Equation5.9 and Equation5.10 are actually *projectors* on the sets I and S, respectively[m]. A qualitative representation of the action of the two projectors P_I and P_S is given in Figure 5.7a. Their effect is shown on a starting density ρ that does not belong to neither I or S. The outcome of the projector is to produce a density in the closest position of the respective set (*i.e.* to provide the spatial distribution that satisfies the respective constraint and is as similar as possible to the original density ρ[n]). These two projectors represent the fundamental building blocks of *phase retrieval algorithms*. This can be intuitively deduced by observing the "dynamics" of the alternate application of P_I and P_S onto a density ρ, as sketched in Figure 5.7b. This alternate application of the projectors makes the density *jump* between the two sets. The implications of using the projection operation is that each "jump" is shorter than the previous one (*i.e.* by such a use of the projectors, the values of ρ evolve in a way that *minimizes* the distance[o] between the two sets, I and S).

The first, most trivial, phase retrieval algorithm, which is exactly built in this way, is called *Error Reduction* algorithm[72] due to its property of reducing the distance between the two sets (*i.e.* the *error* of the *reconstruction*) at each *iteration*. A single iteration of the *Error Reduction* (ER) algorithm can be easily expressed, again, in terms of operators as

$$ER = P_\mathsf{S} P_\mathsf{I}\,, \tag{5.11}$$

such that a given number n of *Error Reduction* iterations can be conveniently written as ER^n. The outcome of a given number of algorithm iterations is addressed as *reconstruction*. The first algorithm iteration requires a starting density ρ. Such a density, often called *starting guess*, doesn't have to satisfy any particular condition (like the pineapple in Figure 5.7b. The iterative nature of the reconstruction process is the reason why this

[m] This can be easily demonstrated by checking if they are *idempotent* (which is the the definition of a projector). In fact, if they are applied more than once, the result does not change (*i.e.* $P_\mathsf{I}^2\,\rho = P_\mathsf{I}\,\rho$. and $P_\mathsf{S}^2\,\rho = P_\mathsf{S}\,\rho$).

[n] This statement can be dangerous for the health of mathematicians. Please, handle with care.

[o] The concept of minimizing a distance is fundamental and it will be discussed in a later section.

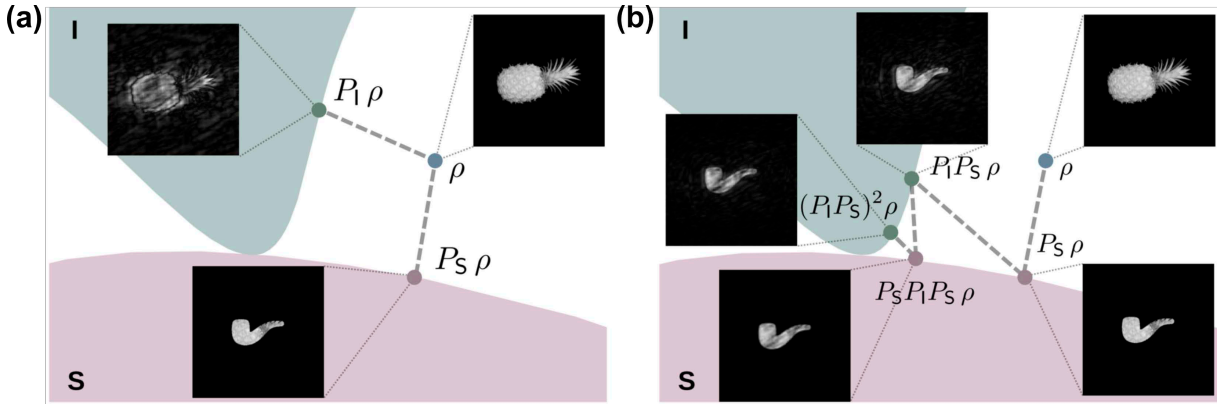

Figure 5.7: (a) Qualitative representation of the action of projectors onto the two sets. The blue dot, which is outside both the sets S and I, stands for a density which is incompatible with both the support and intensity constraints, like the pineapple. The two projector operators provide, as output, the density *closest* to the pineapple that belongs to the respective sets. (b) Illustration of the alternate action of the two projections on a starting density. The two projectors are applied in an alternate manner to a starting density. The nature of this process, based on projections, is such that the trajectory moves towards a configuration of (local) minimum distance between the two sets.

imaging approach is also known as "Iterative Phase Retrieval" (IPR). A straightforward numerical implementation of the ER algorithm is given in the following script:

```
def ER(rho, modulus, support, iterations):
  '''
  Execute a given number of Error Reduction iterations on the starting
   guess rho
  '''
  # Loop over the amount of iterations
  for n in range(iterations):
    # Apply the intensity projector
    rho = P_I(rho, modulus)
    # Apply the support projector
    rho = P_S(rho, support)
  return rho
```

Although the ER algorithm is elegant and simple to use, it has limited effectiveness. The main culprit is the nature of the intensity constraint, and in particular into the shape of the set I. In fact, the set S has the convenient feature of being a *convex set* (*i.e.* any linear combination of densities belonging to the set still belongs to it). This is definitely not the case for set I.[p] The different shapes of the two sets can be qualitatively reproduced by using convex and non-convex morphologies (see Figure 5.6). Although not

[p]Proving this aspect goes beyond the scope of this chapter, and we warmly suggest to give a read to the enlightening review of phase retrieval algorithms in Reference [134]

being mathematically rigorous, it helps to incorporate the intuition that such a non-convex shape of the set I has the unavoidable effect of creating *local minima* of the sets distance. The ER algorithm, due to its nature, hardly escapes from this trap and always fails to reach the correct solution. This issue was already clear to J.R. Fienup, the pioneer of phase retrieval, who in the 1970's already proposed an alternative algorithm: the *Hybrid Input-Output* (HIO)[71]. Again, an iteration of the HIO algorithm can be expressed in terms of projectors as

$$HIO = P_{\mathsf{S}}P_{\mathsf{I}} + (\mathbf{1} - P_{\mathsf{S}})(\mathbf{1} - \beta P_{\mathsf{I}})\,, \tag{5.12}$$

where $\mathbf{1}$ is the identity operator. The first part of this expression, $P_{\mathsf{S}}P_{\mathsf{I}}$, is equivalent to the ER algorithm in Equation5.11. The second part can be interpreted as a "correction". The first important thing to note is that such a correction is only applied to the components of ρ *orthogonal* to the support set S, thanks to the operation $\mathbf{1} - P_{\mathsf{S}}$[q]. In practice, this means that only coordinates of ρ outside the support function are affected. Those values are then suppressed by a quantity βP_{I} *via* the operation $\mathbf{1} - \beta P_{\mathsf{I}}$. The HIO operator can be translated into numerical code in the following way:

```
def HIO(rho, modulus, support, iterations, beta):
  # Loop over the amount of iterations
  for n in range(iterations):
    # Apply the intensity projector
    rho_I = P_I(rho, modulus)
    # Apply the support projector and the correction to the orthogonal
   component
    rho_S = P_S(rho_I, support) + (1-support)*(rho-beta*rho_I)
    rho = rho_S
  return rho
```

The Hybrid Input-Output is still among the most effective and widespread phase retrieval algorithms. Since its conception, several iterative algorithms with improved performances have been developed, based on peculiar combinations of the projector operators. The reader now has the necessary knowledge to enjoy dedicated technical papers about these improved iterative algorithms[13,129,60,155], starting from a comparison given in Reference [134]. Further algorithmic improvements have been achieved by leaving the "pure" application of projectors[40] or even combining the iterative methods with genetic algorithms[42]. When approaching small-angle CDI, the understanding of phase retrieval algorithms is often considered the main obstacle to overcome in setting up a proficient data analysis framework. However, this often turns out to not be the case. Most of the problems concern aspects that are rarely mentioned in scientific literature and will be discussed in the following sections.

[q]This operation results in the components of ρ orthogonal to the set S only because P_{S} is an *orthogonal projector*.

Phase retrieval as an optimization problem

The difference between two densities ρ_1 and ρ_2 is represented, under the perspective of sets, as the *distance* between two "points" in the space of the possible configurations. This space of configurations is the space where all spatial distributions ρ exist, of which I and S are subsets. Such a space is of extremely high dimensionality since for a diffraction pattern of $N \times N$ pixel values the spatial densities belong to a space of size $\mathbb{R}^{N^2}$.[r] The visualization in terms of sets shown in Fig. 5.6 is a simplified view of this space of configurations in $\mathbb{R}^2$. The most straightforward way in which a *distance* can be calculated is through the Euclidean metric. Given the Euclidean norm as $\|\vec{x}\|^2 = \sum_i x_i^2$, the *distance* between two densities is given by $D[\rho_1, \rho_2] = \|\rho_2 - \rho_1\|$. This way, we can compute how far ρ is from its projection on the two sets I and S (*i.e.* $D[\rho, P_\mathsf{I}\,\rho]$ for set I and $D[\rho, P_\mathsf{S}\,\rho]$ for set S).

It is possible to "build" functions that evaluate the *error* of the reconstruction ρ by computing the distance between two alternated projections on the two sets. In particular, for a generic density ρ, we first apply a projection on one of the two sets (*i.e.* $P_\mathsf{S}\,\rho$ or $P_\mathsf{I}\,\rho$) and then compute the distance between this projection and a subsequent one on the other set (see Figure 5.8a). These two error values can be numerically computed as

$$\begin{aligned} E_\mathsf{S}[\rho] &= D[P_\mathsf{I}\,\rho, P_\mathsf{S} P_\mathsf{I}\,\rho] = \sqrt{\sum_{ij} (1 - S)|\rho_\mathsf{I}|^2}\,, \\ E_\mathsf{I}[\rho] &= D[P_\mathsf{S}\,\rho, P_\mathsf{I} P_\mathsf{S}\,\rho] = \sqrt{\sum_{ij} \left(|\tilde{\rho}_\mathsf{S}| - \sqrt{I}\right)^2}\,, \end{aligned} \tag{5.13}$$

where $\tilde{\rho}_\mathsf{S}$ is the FT of the density projected into set S, ρ_I is the density projected on set I, and S is the support function. In practice, E_S gives the amount of density outside the support function for a density whose diffraction pattern is the experimental one. On the other hand, E_I tells us how far from the experimental data is the Fourier amplitude of a density fully contained in the support function[s]. The two error functions are, in principle, equivalent, but E_I is often preferred because it is easier to normalize and involves a direct comparison with the diffraction pattern[t].

The search for the solution to the phase problem, *i.e.* the intersection $\mathsf{I} \cap \mathsf{S}$, is equivalent to the search for the density ρ such that $E[\rho] = 0$ (see Figure 5.8a). However, this is not the case when dealing with experimental data, that is intrinsically[u] affected by noise. The side-effect of noise is that, in a realistic case, there is no density ρ compatible with both

[r] In general, scattering densities are complex valued, thus belonging to the space $\mathbb{C}^{N^2}$, but this will be a discussion topic for Section 5.2.2

[s] The reader may have noted that E_I is computed in the Fourier space, and not in real space. The Fourier Transform operation is unitary, which means that the norm is conserved. Thus, the error can be equivalently computed in real or Fourier space, and the choice of the latter is just for convenience.

[t] For further discussion on the error function, for example about its normalization or the inclusion of experimental noise, please refer to References [70,134,109].

[u] Don't forget that light detectors count the number of photons that reach each pixel. This means that, at least, *Poisson* noise affects experimental data. See the dedicated discussion in Section 5.2.2.

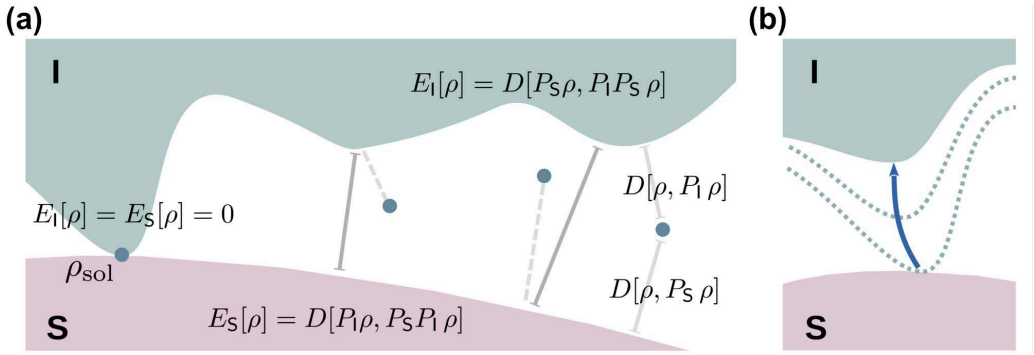

Figure 5.8: (a) The error value of a reconstruction can be visualized in terms of distances (here shown as continuous gray lines) between projections on the two sets I and S. The solution ρ_{sol} is, in theory, the one for which the error is 0, *i.e.* it belongs to both sets. (b) Due to noise, the two sets do not intersect any more and the phase problem turns into the problem of finding the density ρ_{sol} with minimal error.

constraints at the same time (*i.e.* $\mathsf{I} \cap \mathsf{S}$ is an empty set as shown in Figure 5.8b). The phase retrieval problem then becomes the search of the density ρ which minimizes the distance of the two sets, that is:

$$\rho_{\mathrm{sol}} \equiv \{\rho : E[\rho] < E[\sigma] \,\forall\, \sigma \neq \rho\} \tag{5.14}$$

Equation 5.14 changes the perspective under which the phase retrieval problem is observed, turning it into a full-fledged *optimization problem* for the error E. Furthermore, the lowest reachable error, that is $E[\rho_{\mathrm{sol}}]$, is not known *a priori*. Its value strongly depends on the "structural properties" of the sets I and S, which are in turn connected to the features of the experimental data and the support function, as discussed in the following sections.

The role of the support function

The definition of a support function is pivotal for rendering the phase problem solvable. As described in the introduction to this section, in theory the support function doesn't have to perfectly fit the sample shape, but it just needs to ensure that the *oversampling* condition is met. For example, this implies that any of the support functions shown in Figure 5.9a is enough to guarantee that the *pipe* density is the only solution. However, the *landscape* of the error function strongly depends on how the support function is defined. For example, the different supports A-D in Figure 5.9a are linked to a pictorial representation of their corresponding set S (see Figure 5.9b). As each support function is contained in the larger ones, then the same happens for the sets (*i.e.* $D \subset C \subset B \subset A$).

The two blue lines in Figure 5.9b highlight local minima of the error function when support A is considered. These local minima, far away from the correct solution, are avoided when the support function is made tighter. This effect seems of little importance

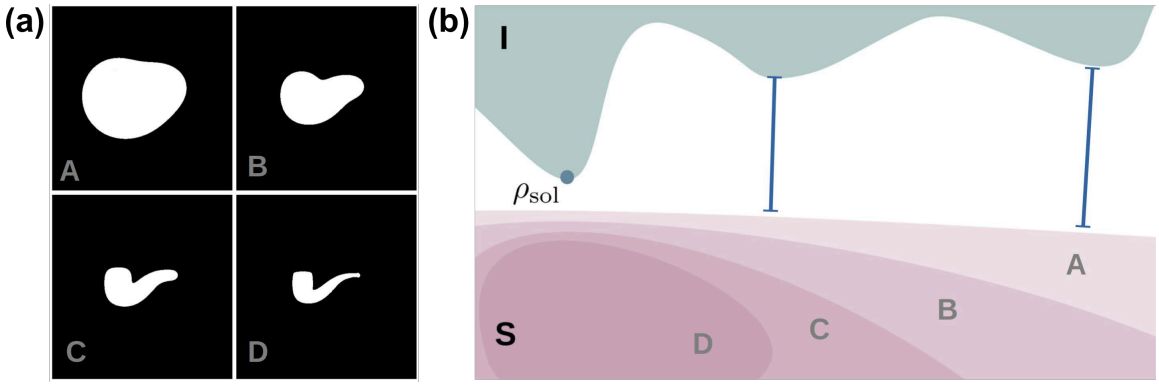

Figure 5.9: The effects of the support shape on the phase problem. (a) Different support shapes with decreasing size, labeled as A,B,C and D. All of them are compatible with the pipe and are sufficient to ensure the existence of a unique solution. However, the existence of a solution doesn't tell anything about the possibility to find it. (b) Graphical representation of the change in shape of the set S, depending on the support size. For the looser support function A, the size of set S is bigger, introducing local optima of the error function that vanish for tighter supports.

when represented in two dimensions, but it has dramatic consequences when considering the real problem, which lives in a N^2-dimensional space. For this reason a tight support function must be used for practical applications. The precise knowledge of the support function (*i.e.* the overall shape of the sample under study) is a strong limitation for the application of CDI, as the sample architecture is, in most cases, unknown. However, a simple and effective solution was provided in the groundbreaking work in Reference [135], which introduced the *shrink-wrap* algorithm. The concept behind the *shrink-wrap* is to retrieve the correct support shape along with its respective density. The first step of the algorithm is to perform a smoothing operation on the current density estimate ρ, by a convolution operation with a gaussian function of width σ. The smoothed density, ρ_σ, is then used as a reference to estimate the new support function:

$$SW[\rho] = \begin{cases} 1 & \text{where } \rho_\sigma > \tau \cdot \max[\rho_\sigma] \\ 0 & \text{elsewhere} \end{cases} \tag{5.15}$$

In practice, a threshold is applied to the smoothed density estimate ρ_σ: the new support function is set to 1 where values of ρ_σ are above this threshold value, and to 0 where they are below. This threshold value is defined as a fraction τ of the maximum value of ρ_σ. The quantity σ is expressed in pixels, and it usually takes values up to a few pixels. Typical values for τ are, instead, around a few % of the maximum value of ρ_σ. This operation is performed once every several iterations of iterative algorithms, and the exact values of σ and τ are dependent on the properties of the sample and the quality of experimental data. A possible numerical implementation of the *shrink-wrap* algorithm is listed below:

```python
# Here we import a gaussian filter for smoothing implemented in the
    scipy modulus.
from scipy.ndimage import gaussian_filter as smooth

def SW(rho, sigma, tau):
  # Apply the gaussian smoothing
  rho_smooth = smooth(rho, sigma)
  # Initialize the new support with zero values
  support = np.zeros(rho.shape)
  # Calculate the new support function from the smoothed density
  support[rho_smooth > tau*np.amax(rho_smooth)]=1
  return support
```

Thanks to the *shrink-wrap* algorithm, the initial support can be considerably loose[v]. Different methods can be used to deduce a loose starting support without any particular knowledge of the sample. For a deeper insight into this topic, we warmly recommend Reference [135].

Due to the presence of noise, a practical problem when the support function is retrieved during the reconstruction process is that, for shrinking support sizes, the error value of the solution (*i.e.* the minimum distance between the two sets) increases (see Figure 5.9). This aspect has three important practical consequences. First, the error value of the reconstruction often increases during the reconstruction process. Second, two reconstructions can be compared based on their error value only if the support size is the same. Third, a *wrong* reconstruction with a loose support function often has error values lower than the *correct* reconstruction with a tight support function. Thus, when the support function is also retrieved, the error value as defined in Equation 5.13 is, in general, not a good metric to evaluate the reconstruction quality both in its absolute and relative sense.

Dealing with missing data

A striking feature of experimental data is the lack of diffraction in some areas of the detector. This depends in part due to the structure of the detector itself, organized in separated "tiles", such that stripes of missing data often cover the whole detector surface. However, the *always* missing portion of experimental data is the one close to the detector centre. For high-intensity light sources in the XUV and X-ray regime, the scattering cross-section of materials is very low, such that only a small fraction of the incoming light undergoes scattering in the sample. For this reason, a large amount of photons (*i.e.* high radiation intensity) has to be produced to obtain meaningful diffraction signal in a single laser shot[w]. The majority of this radiation simply proceeds past the interaction region, and could irretrievably damage the detector components. For this reason, scattering detectors contain a hole in the middle and cannot record data close to the centre. The

[v] the only constraint that it must satisfy is, in principle, the oversampling condition.

[w] At the end of the story, that's the reason why Free Electron Lasers are necessary.

spatial coordinates at which scattering data is missing are often encoded in a matrix, known as *mask*, which has values of 1 where pixels are missing, or 0 otherwise. The action of the intensity projector P_{I} is then adapted to take the mask M into account:

$$P_{\mathsf{I}}\,\rho = \mathcal{F}^{-1}\left[M \cdot \tilde{\rho} + (M-1)\cdot\sqrt{I}\frac{\tilde{\rho}}{|\tilde{\rho}|}\right] \tag{5.16}$$

In practical terms, P_{I} in Equation 5.16 replaces $|\tilde{\rho}|$ with $\sqrt{I}$ only where $M = 0$. This adds an *intensity retrieval problem* to the *phase retrieval problem*, as the missing intensities, which cannot be constrained, have to be retrieved along with the phases. The effects of missing diffraction data are, in first approximation, similar to the effects of a looser support (see Figure 5.9). With less available data, the intensity constraint becomes looser and looser, affecting the error landscape and causing the algorithms to stagnate in local minima of the error function.

Furthermore, the Fourier domain has peculiar properties when dealing with isolated samples, and, rephrasing a famous statement from Orwell's *Animal Farm*, "all pixels are equal but some are more equal than others". In fact, the central data of the diffraction contains the coordinates of the momentum transfer q close to 0. This corresponds to low-resolution information on the sample[x]. This is intuitively shown in simulated diffraction patterns of an increasingly bigger pipe (see top row in Figure 5.10) that are made more realistic by removing data usually not accessible by the scattering detector. If the field's values in that part are set to 0, and the field is inverted back to the real space (see bottom row in Figure 5.10), the resulting sample image is roughly a *high-pass* filtered version of the original one[y]. In particular, the leftover information for the first, smaller, pipe in Figure 5.10 still contains relevant features of the sample. Increasing the sample size, the overall features of the sample begin to be lost, up to the point where most low-resolution spatial information is completely missing as bigger samples have relatively more information closer to the centre of the pattern. It is already possible to guess how phase retrieval algorithms can retrieve the missing intensities (e.g., by carefully looking at Figure 5.10). In fact, setting the missing intensities to 0 provides a real-space image of the sample that is no more completely compatible with the support constraint, if the provided support function is close enough to the actual sample shape (*i.e.* density values different from 0 appear outside the pipe boundaries). This incompatibility, which allows phase retrieval algorithms to restore the missing data thanks to the application of the support projector P_{S}, reduces with increasing size of the sample (see the bigger pipe in Figure 5.10). The larger the sample, the harder the retrieval of missing intensities will be. The missing central data is, for practical applications, the true limiting factor for the maximum size of samples that can be successfully retrieved.

[x] for a more careful discussion about resolution, see Section 5.2.2.

[y] In a similar way, a Gaussian smoothing is a low-pass filter (*i.e.* high q values are suppressed).

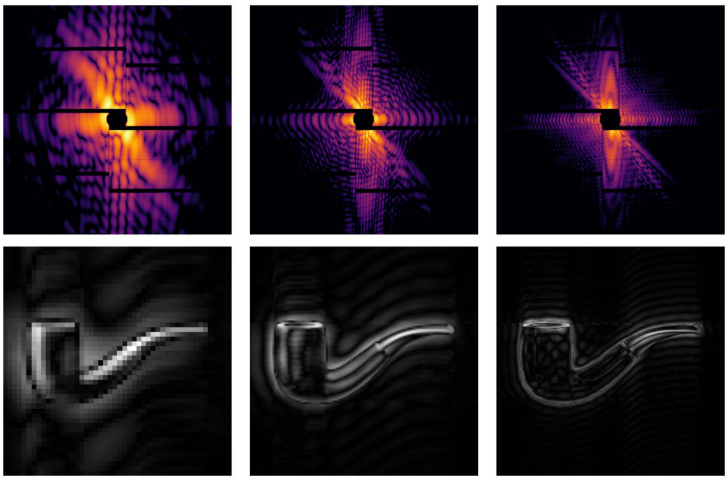

Figure 5.10: Effects of missing diffraction data. Upper row: Diffraction patterns simulated for pipes of increasing size. Missing values in real experimental data are set to zero. Lower row: pipe image obtained with the *masked* field intensity in the upper row, giving a real-space qualitative representation of the information available to phase retrieval algorithms, which also have to retrieve the missing scattering amplitude along with the missing phases.

The concept of oversampling

Oversampling is a key concept in CDI[139]. There are slightly different approaches to interpret the *oversampling* condition. Here, we proceed in the most intuitive and simple way, while we suggest to refer to References [138] and [109] for a more rigorous and correct treatment of the topic. Despite having shown the density functions ρ as real-valued functions (or, better, real valued $N \times N$ matrices), their values are, in general, complex numbers[z]. Not all the values of ρ have to be retrieved, as those outside the support function are constrained to 0, such that only the remaining values inside the support represent the *unknowns* of the phase problem. Their amount equals to twice the support size in pixels, where the factor of two comes from the complex nature of the density values. If the density values within the support are addressed as the *unknowns* of the phase problem, the experimental values (*i.e.* the pixels in the diffraction pattern) are a full-fledged set of *equations*. The ratio between the amount of pixels in the diffraction data and the the amount of pixels in the support function is known as *oversampling ratio* σ, given by

$$\sigma = \frac{N^2}{\sum_{i,j} S_{ij}}\,, \tag{5.17}$$

where the support function is now indicated as a matrix S_{ij} with values 0 or 1, and N is the linear dimension of the diffraction pattern. To render the problem solvable, it

[z]The reason why the density must be complex will be discussed in the next Section 5.2.2.

is necessary to have more *equations* than *unknowns*. As long as the density values to be retrieved belong to $\mathbb{C}$, this only happens when $\sigma \geq 2$. The oversampling condition described above is necessary, but actually not sufficient to ensure a unique solution. In fact, the set of *equations* of the problem (*i.e.* the pixels in the diffraction data) also have to be *independent*, which means that they must provide additional and not redundant information. For a deeper discussion of this topic, the reader is referred to Reference [109].

Complex-valued density: what CDI sees

In general, the scattering density ρ is a complex-valued function. Earlier we linked the scattering density ρ with the spatial density of the electrons (which are the fundamental scattering "units" for light). CDI can thus resolve different materials within the sample, thanks to their different electron density. This picture is a very simplified view on light-matter interaction, and does not consider *how* electrons respond to the incoming radiation. Deriving the behaviour of electrons in their interaction with light is a wide topic and goes well-beyond the scope of this chapter. The reader is recommended to consider References [23] and [158] for further details. Here, it is sufficient to state that the response of the electrons to the incoming light is fully encoded in the complex refractive index n. Under some approximations[158], completely valid[aa] in the X-ray regime, we can state that the scattering density $\rho(\vec{r})$ is linked to the sample's spatial distribution of the complex refractive index $n(\vec{r})$ by

$$\rho(\vec{r}) \propto 1 - n(\vec{r})^2 = 1 - [1 - \delta(\vec{r}) + i\beta(\vec{r})]^2 \approx 2[\delta(\vec{r}) - i\beta(\vec{r})]\,, \tag{5.18}$$

where the complex refractive index is expressed as $n = 1 - \delta + i\beta$. This is a convenient notation when dealing with photon energies in the X-ray regime, where the refractive index of materials is very close to unity[95]. The values of δ and β are then much smaller than 1, allowing the last approximation step in Equation 5.18[ab]. Here, it is only necessary to note that, in the *small-angle* regime, only the projection of the scattering density $\rho(x, y)$ is imaged. Its values are related to the optical properties of the sample integrated along the beam propagation direction, as given by:

$$\rho(x, y) \propto \int_{\parallel} [\delta(\vec{r}) - i\beta(\vec{r})] = \delta(x, y) - i\beta(x, y) \tag{5.19}$$

An example of a complex-valued scattering density is given in Figure 5.11. All scattering patterns shown so far were *centrosymmetric*, *i.e.* $I(q_x, q_y) = I(-q_x, -q_y)$. This is directly derived from the fact that the Fourier transform of a real-valued function is *hermitian*[ac]. This is no more the case for an entirely complex-valued density (e.g. asymmetries of the diffraction data are visible in the left panel of Figure 5.11). It is common,

[aa] almost. See Section 5.2.3

[ab] A deep understanding of the effects of n in the scattering signal is pivotal for the development for data analysis methods in the *wide-angle* scattering regime. See Section 5.2.3

[ac] A *hermitian* function has the property $f^*(x) = f(-x)$, where * denotes the complex conjugate. The modulus of such functions is then centre-symmetric around 0.

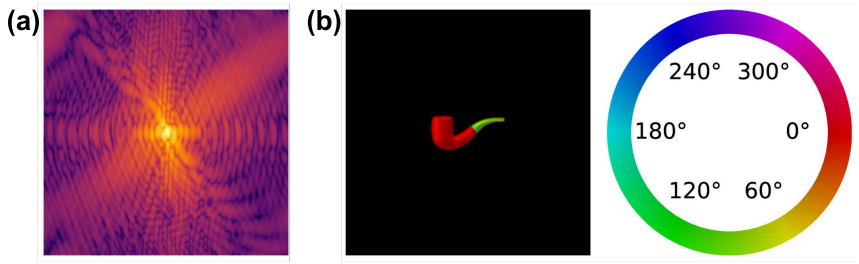

Figure 5.11: A complex-valued density distribution and its simulated diffraction pattern. The real-space phase of the sample is encoded in the hue. We note that an imaginary part different from zero results in a non-centrosymmetric diffraction pattern.

and convenient, to restrict the "complexity" of the reconstruction values when performing phase retrieval[134]. In particular, the support projector P_S is often modified to also constrain the positive value of the real part, which means, in numerical terms, that all pixels of ρ that have negative real part are set to zero. In this way, the unknowns of the phase problem (*i.e.* the density values) are still allowed to be complex, but their value is restricted to half of the complex plane. This constraint is often valid for small variations of the refractive index[134].

Equation 5.19 explains why a complex-valued spatial density ρ is required to correctly describe the sample. Still, the story is not over. For example, when an optically homogeneous sample is considered (*i.e.* made of the same material, or different components with similar optical properties) δ and β maintain constant values within the sample, and zero outside. The result of the integral in Equation 5.19 can be then reformulated in the following way:

$$\rho(x,y) \propto \int_{\parallel} S(\vec{r})[\delta - i\beta] = D(x,y)[\delta - i\beta] = D(x,y)|\delta - i\beta|e^{\Phi} \tag{5.20}$$

Here, $S(\vec{r})$ can be imagined as a 3D support function which describes the sample's extension, and $D(x,y)$ is a 2D function which describes the sample's depth as function of the projection coordinates. As $\delta - i\beta$ is now a constant complex number, it can be separated into the its constant modulus and constant phase Φ components. If we now calculate the diffraction pattern of the density distribution in Equation 5.20, it turns out that the intensity of the scattered field is:

$$I(q_x,q_y) \propto \left|\mathcal{F}\left[D(x,y)|\delta - i\beta|e^{\Phi}\right](q_x,q_y)\right|^2 = |\delta - i\beta|^2 \left|\mathcal{F}[D(x,y)](q_x,q_y)\right|^2 \tag{5.21}$$

Thanks to the properties of the Fourier Transform, and due to the fact that only the modulus squared of the field is experimentally detectable, any global phase added to the scattering density ρ does not change the scattering pattern. Thus, this information is not accessible *via* phase retrieval, and *phase contrast* only arises when materials with different ratios between δ and β are inhomogeneously distributed into the sample. The fact that a global real-space phase value does not change the scattering signal is a hint that there

are actually infinite solutions to the phase problem, and it only has a unique solution in a broad sense. This is just one among the possible *ambiguities*, as explained in the next section.

Ambiguity of the solution

As mentioned in the previous section, the existence of a unique solution to the phase problem has to be intended in a broad sense, as there is, in practice, an infinite amount of solutions. This ambiguity arises because there are some properties of the sample which are encoded only in the field's phases, and cannot be thus retrieved. These ambiguities directly derive from the properties of the Fourier Transform. A first example was discussed in the previous section by Equation 5.21, where a constant phase factor doesn't change the diffraction pattern. This is visually presented in Figure 5.12, where the density in Figure 5.12b is obtained by a constant phase factor from Figure 5.12a. Furthermore, given a density distribution $\rho(x, y)$, both $\rho(x_0 + x, y_0 + y)$ and $\rho^*(-x, -y)$ have the same scattered field's amplitudes (where ρ^* stands for the complex conjugate operation). The former means that the diffraction pattern is *invariant* under a translation of the density to x_0, y_0 (see Figure 5.12c). The latter signifies that the diffraction signal is *invariant* under coordinates inversion and complex conjugation of the density (see Figure 5.12d). It is easy to show that also any combination of these operations represents a solution (see Figure 5.12e).

In general, this multitude of solutions does not represent a problem, as all of them are easily relatable to each others through simple mathematical operations. When dealing with data analysis based on phase retrieval, it is a common practice to consider the final solution as the average of different reconstructions from different starting conditions[223]. As different reconstruction processes will certainly provide different spatial distributions (like the ones in Figure 5.12), it is then necessary to "reshift" these solutions to a common reference before any averaging or comparison. A useful trick is to take advantage of the *cross-correlation* operation. An intuitive meaning of the cross-correlation $f \star g$ between two functions f and g is that its maximum value gives the degree of similarity between the two functions[ad].

As mentioned before, in the case where two solutions to the same phase retrieval problem ρ_1 and ρ_2 are compared, it is necessary to resolve the ambiguities that exist between the two. If ρ_2 is considered as the reference, the first step is to check which of $\rho_1(x, y)$ and $\rho_1^*(-x, -y)$ is most similar to ρ_2. To do so, two cross correlations $R(x, y) = \rho_1(x, y) \star \rho_2(x, y)$ and $R^*(x, y) = \rho_1^*(-x, -y) \star \rho_2(x, y)$ have to be computed. As the

[ad]The cross correlation can be efficiently computed *via* the *convolution theorem*. The convolution between two functions f and g, denoted as $f * g$, is given by the inverse FT of their product in Fourier space, *i.e.*:

$$f * g = \mathcal{F}^{-1}\left[\mathcal{F}[f] \cdot \mathcal{F}[g]\right] \tag{5.22}$$

The cross-correlation between two signals $f(x)$ and $g(x)$ is then the convolution of $f^*(-x) * g(x)$.

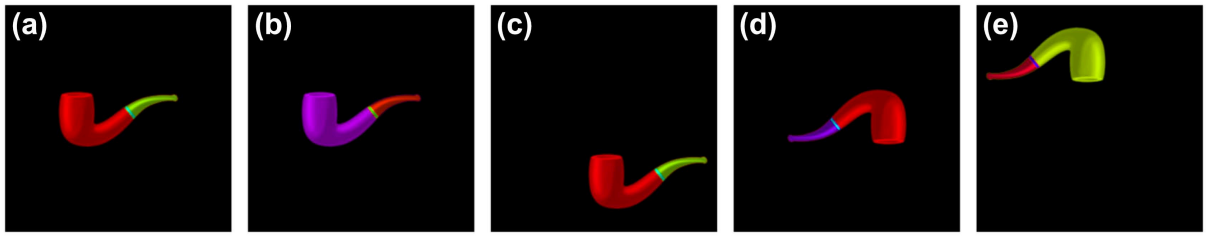

Figure 5.12: Ambiguities of the solution to the phase problem. (a) A complex-valued density function is shown. Its real-space phase is encoded in the hue, following the scheme shown in Figure 5.11. (b) A constant phase value is added to the density. (c) The density is translated. (d) The complex conjugate of the density. Its spatial coordinates are inverted in sign. (e) A density resulting from the combination of the three operations in (b)-(d). All the densities shown here have the same Fourier amplitudes, and are, thus, all valid solutions to the same phase retrieval problem.

maximum value of the cross-correlation provides the similarity between the two densities, it is intuitively clear that if $\max(R) < \max(R^*)$ then it is necessary to "flip" ρ_1 (see Figure 5.12d). Furthermore, the coordinates x, y of the maximum cross-correlation value encode the relative shift between the two functions. For two perfectly overlapping densities, the maximum value is at coordinates $(0, 0)$. In general, if the maximum value of the cross-correlation R (or R^*) is placed at coordinates (x_0, y_0), this provides to the amount of spatial shift (in pixels) that must be applied to ρ_1 in order to overlap with ρ_2 (*i.e.* the translation operation in Figure 5.12c). Finally, the phase of $\max(R)$ (or $\max(R^*)$) yields the phase-shift to add to ρ_1 such that it matches the phase of ρ_2 (*e.g.* in the case shown in Figure 5.12b). Thanks to this trick, different outcomes of a phase retrieval reconstruction can be spatially compared with each other, and operations like averaging are now meaningful.

An additional, more practical, problem, that affects the phases of the real-space density reconstruction arises from the choice for the coordinates of the centre of the diffraction pattern. In fact, the scattering pattern has to be "prepared" for a phase retrieval algorithm such that, for a pixel resolution $N \times N$, the central peak of the diffraction corresponding to the momentum transfer $(0, 0)$ is placed at the coordinate `[N/2, N/2]` in the scattering matrix (or at `[0,0]` when frequencies are shifted). When dealing with real data, it is often a difficult task to identify the correct centre, as this data is missing due to the detector hole (see Figure 5.10). The real-space effect for different centre position coordinates of the diffraction (see Figure 5.13), highlights how it affects the reconstruction result. In particular, such shifts of the diffraction pattern cause a linear drift of the reconstructions phases, which becomes already dramatic even for a centre misplacement of just a few pixels. This effect can be corrected in post-processing, by correctly reshifting the reconstruction FT at the end of the reconstruction process. However, an incorrect diffraction centre position can prevent the convergence of the iterative algorithms, especially when

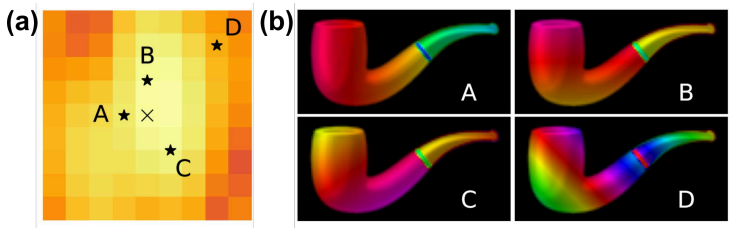

Figure 5.13: Effects of the incorrect centering of diffraction patterns. On the left: close up of the central part of the diffraction pattern. The × marker indicates the correct centre, which produces the "correct" reconstructions in Figure 5.12. Markers A-D indicate different choices of the pattern centre. On the right: the effect of the different centre positions on the real-space phases of the pipe.

the positivity the real part of ρ is constrained (see Section 5.2.2).

The resolution(s) of CDI

When dealing with the term *resolution*, it is not uncommon to confuse between the detector resolution (affecting the diffraction data) and the reconstruction resolution (determining the smallest real-space feature that can be *resolved*, see Figure 5.14).

Recalling the introduction to CDI, it was shown that, in the case of small-angle scattering, only the components of the momentum transfer $\vec{q}$ orthogonal to the beam propagation direction ($\vec{q}_\perp$) are accessible by the detector (see Figure 5.3). This is strictly dependent on how far the scattering detector is from the *interaction region*[ae], which influences the maximum scattering angle $\theta_{\max}$ that the detector can record. From simple geometrical considerations, the magnitude of the momentum transfer $q = |q_\perp|$ recorded by the detector as function of the scattering angle is $q(\theta) = k_0 \cdot \sin(\theta) = \frac{2\pi}{\lambda} \cdot \sin(\theta)$ where $k_0 = \frac{2\pi}{\lambda}$ is the magnitude of the wavevector of the incoming radiation at a wavelength λ. The signal recorded by the detector at given scattering angle θ, and thus, at a given magnitude of the momentum transfer q, is directly relatable to a real-space length scale D *via* the relationship $D = \frac{\pi}{q}$. This relationship (derived from the properties of the Fourier Transform and strictly connected to the Bragg's law) then gives the smallest "size unit" δ in the real-space, corresponding to the value of D at the maximum recorded scattering angle:

$$\delta = \frac{\pi}{q(\theta_{\max})} = \frac{\lambda}{2\sin(\theta_{\max})} \tag{5.23}$$

This "size-unit" δ is the *pixel size* of the reconstruction, giving a conversion scale between pixels and metres, also called the *half-period* resolution. The real-space *resolution* of CDI is instead often considered to be the *full-period* resolution, equal to 2δ [af].

[ae] The interaction region is where light interacts with the sample, and thus where the scattering events take place.

[af] The reason for this choice comes from the Shannon's sampling theorem.

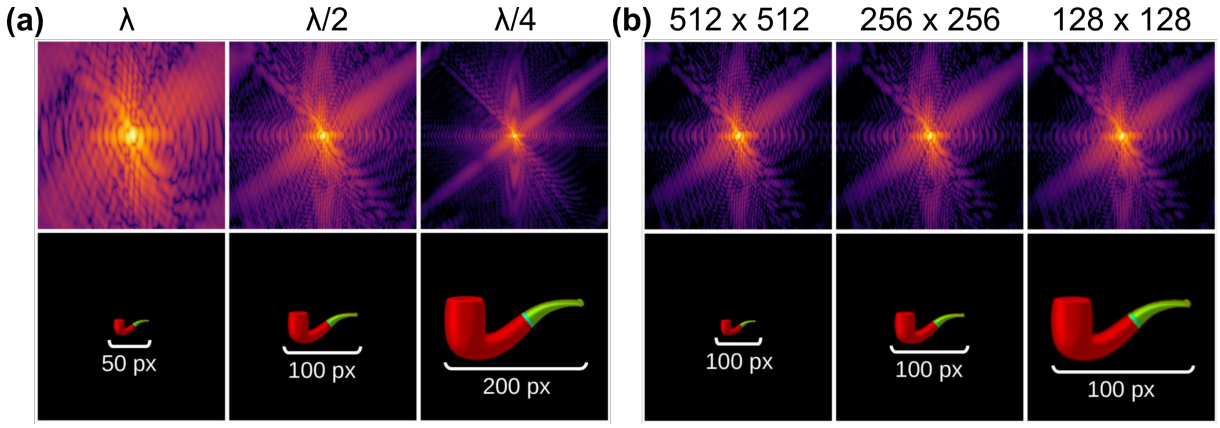

Figure 5.14: The CDI resolutions. (a) Effect of different photon energies on the reconstruction resolution. From left to right, the photon energy is doubled at each step. The real-space reconstruction of the pipe contains an increasing amount of pixels, thus providing information on the sample at higher resolution. The size of the diffraction pattern remains constant at 256x256 pixels. The same effect can be obtained by keeping λ constant and increasing the maximum recorded scattering angle θ_{max}. (b) Effect of different detector resolutions. From left to right, λ and θ_{max}) are constant, but the pixels size is doubled. The actual resolution at which the sample is imaged does not change. Sampling at higher frequency in the reciprocal space only adds regions of zeros around the sample. Therefore, the pixel resolution of the detector affects the maximum size of a sample that can be retrieved.

Equation 5.23 nicely highlights the possibility to tune the CDI resolution. The spatial resolution can be enhanced by increasing the maximum recorded scattering angle θ_{max} (by moving the detector closer to the interaction region, but without leaving the small-angle scattering approximation) or by increasing the photon energy (*i.e.* reducing the wavelength of the incoming radiation). An example of the latter case is given in Figure 5.14a, where the photon energy is doubled at each step. For the same sample, the respective reconstruction is increased by a factor two each time in terms of pixels, as the physical pixel size is halved.

It is worth noting that the resolution of CDI is not connected to the resolution of the detector. This result, which is quite surprising only at a first glance, is highlighted well by Figure 5.14b. In this example, the diffraction data is acquired at the same experimental conditions (*i.e.*, the detector reaches the same scattering angle), but with different pixel resolution. The detector pixel size does not influence the size (in pixels) of the reconstructed pipe, but only the total size of the matrix in which the pipe is "immersed". Thus, increasing the *sampling rate* of the scattering signal only increases the zero-value region around the pipe in real-space. Still, the use of scattering detectors with high pixel count carries undeniable advantages. The first is that the number of *equations* of the

phase problem increases, thus augmenting the oversampling ratio σ in Equation 5.17. This allows to image bigger samples at the same spatial resolution[ag]. Thus, as long as the *oversampling condition* is met (*i.e.*, σ is big enough), it is often convenient to scale down the diffraction data by a *binning operation*. This does not affect the reconstruction resolution (see Figure 5.14b) and considerably speeds up the reconstruction process[ah].

Consequences of noise

Noise intrinsically affects diffraction data. Two main sources of noise can be distinguished, *thermal noise* and *statistical noise*. Thermal noise can be modeled as a uniform, incoherent signal that independently affects each pixel of the diffraction detector. Statistical noise, instead, comes from the intrinsically discrete nature of the radiation. Modern scattering detectors at FEL facilities[214,118,146] are often capable of *single photon sensitivity* (*i.e.* they can distinguish single photon events[34]). This performance is achievable because the strength of the thermal noise, which uniformly affects all the detector pixels, is kept substantially below the signal strength provided by a single photon that impinges on the detector pixel. Here, we only deal with *statistical noise*, and other sources of signal disturbance are neglected. The single-photon sensitivity of pixel in such detectors renders them "photon counters". The statistical behaviour of these *photon events* for a single detector pixel then follows a Poisson probability distribution[ai]. The scattering signal $I_m(q)$ measured by a detector pixel at coordinates $\vec{q}$ can be then modeled as:

$$I_m(q) = \mathcal{P}[I(q)]\,, \tag{5.25}$$

where $I(q)$ is the "exact intensity" (expressed in unit of photons), and $\mathcal{P}[\mu]$ is a Poisson-distributed random number with average μ. Unlike a normal distribution, which requires two parameters (mean μ and standard deviation σ) to produce a random number, the standard deviation of a Poisson number is not a free parameter. It is strictly dependent on the average value, in the form of $\sigma = \sqrt{\mu}$. A common way to express the amount of information contained in a signal in relation to its noise is the Signal-to-Noise Ratio

[ag] A more rigorous explanation involves the sampling theorem, and a parallelism with the real-space resolution δx. As δx depends on the maximum magnitude of the recorded q, then similarly δq (the detector pixels size in Fourier space) affects the maximum size of a retrievable sample. For a more rigorous treatment, see Reference [109].

[ah] For each step of iterative algorithms, a forward and a backward Discrete Fourier Transform (DFT) must be computed. The computing time of the DFT, when computed *via* the Fast Fourier Transform[45], scales as $N^2 \log(N)$, where N is the linear dimension in pixels of the matrix. A simple 2×2 binning operation in the diffraction data reduces the computing time of the DFT by a factor of greater than four.

[ai] The Poisson probability distribution is given by:

$$P(\mu_p, n) = \frac{\mu_p^n e^{-\mu_p}}{n!} \tag{5.24}$$

For example, the probability of measuring 3 photons for a given *exposure time* on a pixel whose signal should be, on average, 1.6, is given by $P(1.6, 3)$.

(SNR), defined as the ratio between the average signal and its standard deviation[aj] (*i.e.*, $\mathrm{SNR} = \frac{\mu}{\sigma}$). Due to the statistical behaviour of photons, the SNR of diffraction data is not constant but depends on the "exact" intensity I:

$$\mathrm{SNR}[I] = \frac{I}{\sqrt{\mathcal{I}}} = \sqrt{I} \tag{5.26}$$

The weaker is the signal I, the worse the SNR, up to the point where $\mathcal{I}$ approaches few counts and the SNR approaches 1 (that is, signal and noise have comparable magnitude). In FEL experiments [ak], and especially in the X-ray region where materials are highly transparent to light, it is very common to have large parts of the scattering signal characterized by very low photon statistics, often approaching zero. As the scattering signal for isolated samples strongly decreases with the distance from the central diffraction peak, this low-intensity region is always placed in the outer region of the detector, which collects data corresponding to high q values. High q values correspond to high resolution information, as highlighted by Equation 5.23. This, in turn, means that noise in diffraction data limits the *actual* spatial resolution of CDI (as exemplified by Figure 5.15a). Here, we address this important topic in a highly simplistic manner, and we refer the reader to the analysis in Reference [99] for a more complete and correct view on the topic.

The actual CDI resolution is, in this case, not defined by the maximum scattering angle θ_{max}, but by the maximum scattering angle at which light can be effectively recorded, θ_{eff}. For example, an increase in θ_{max} would just decrease the pixel size in real space (see second and third case shown in Figure 5.15a) but would not carry an improvement in the effective spatial resolution (as no additional information would be recorded).

As discussed above, another option to increase resolution is to increase the photon energy of the radiation. For example, doubling the photon energy theoretically leads to halving of the pixel size in the real space representation (see Figure 5.14a). However, the refractive index of materials, and thus their "scattering strength", dramatically drops with increasing photon energy, thus lowering the amount of scattered photons and the effective resolution (see Figure 5.15a), up to the point where increasing the photon energy is actually counter-effective[al].

The effect of low photon statistics is even more dramatic when dealing with real diffraction data, where the central part of the scattering image is missing. The same

[aj] There are actually different ways to define the SNR. This definition is mostly used when dealing with strictly positive signals, like in imaging processing.

[ak] For applications where the *illumination time* can be freely decided (like in diffraction experiments at synchrotrons), the SNR value can be indefinitely increased, up to the point when significant SNR is obtained all over the diffraction data. Such an approach is not viable for FEL diffraction experiments, where the femtoseconds pulse duration is a key feature in both imaging ultrafast dynamics and avoiding signal degradation from the sample damage by the intense ultrashort pulse (the *diffract and destroy* concept[39]). Furthermore, due to the sample destruction, the same sample usually cannot be imaged with multiple pulses. Thus, the photons available for scattering in FEL experiments are only the ones contained in a single femtosecond pulse.

[al] This aspect represents one of the main limiting factors for FEL science towards imaging of single atoms and molecules, along with the problem of *radiation damage*[213].

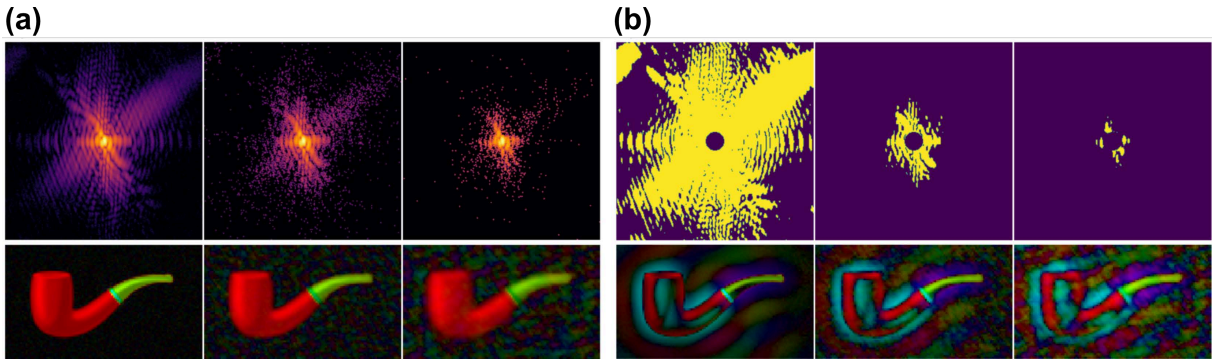

Figure 5.15: The effects of noise. (a) Simulated diffraction patterns with decreasing signal strength and noise from Poisson statistics. Corresponding complex densities in lower row. The effect of losing information at high scattering angle is to reduce the actual resolution of the reconstruction, which appears smoother. (b) Realistic data with missing center information. A mask is applied to patterns in (a) and the regions where the SNR value is above 1 are highlighted in yellow color (upper row). These can be addressed as areas of meaningful data. Lower row: left-over information with similar effects to Figure 5.10.

diffraction patterns shown in Figure 5.15a are now replicated in Figure 5.15b, where the central part is now removed to simulate the detector hole that accommodates the transmitted beam of the laser pulse. Due to the decrease in the scattering signal with increasing distance from the centre, the lower the diffraction *brightness*, the higher the relative fraction of usable information present in the central portion of the scattering data. When that information is lost due to the detector's hole, the deterioration of the leftover information becomes dramatic. The three cases in Figure 5.15b have, in theory, the same *oversampling ratio*, as it was defined in Equation 5.17. However, it is now clear that, in the case of noisy data, the amount of pixels containing meaningful information on the sample is much lower than the total number of pixels in the matrix. We can roughly estimate that pixel values are usable only when the signal is distinguishable from the noise (*i.e.* when the SNR value is greater than a given threshold). These pixels are highlighted in the first row of Figure 5.15b, for a conservative choice of a SNR threshold of one. It is convenient here to define the relative information actually provided by a diffraction pattern as $\eta = \frac{\sum \mathrm{SNR}_>}{N^2}$, where $\mathrm{SNR}_>$ is a binary map which has a value of one where the diffraction data has useful SNR. It is now intuitively clear that the actual oversampling ratio σ required to uniquely identify a solution to the phase problem has to be higher than two and, in particular, it can be estimated at a value of $\frac{2}{\eta}$. The value of η cannot be perfectly known *a priori*, because the SNR calculation would require knowing the exact field. Still, it can be roughly estimated by counting the number of pixels in the experimental data that have values higher than one photon count. It is not uncommon in FEL data to have $\eta < 0.2$ (*i.e.* only 20 % of the measured data carries significant information). This is the reason why, in most real-case applications, phase retrieval is

successful only when the oversampling ratio $\sigma \gg 2$.

A real-life example

Here, we apply our observations about noise and missing data on real FEL data and respective phase retrieval results using the example of a representative diffraction pattern (see Figure 5.16) from an experimental campaign at the Maloja endstation of SwissFEL[215].

One aspect that has not been discussed yet, but is of practical importance, is how to identify relevant and representative patterns out of a large data set. Also rare events can be pivotal for the understanding of the target under study, which are even harder to find. Ideally, this identification and classification of typical and rare patterns is already possible during the experimental campaign. This requires fast methods that can deal with huge data sets. To this end, sophisticated analysis pipelines have been developed in the community[90,49]. Furthermore, machine learning techniques have been recently applied on single-particle CDI data sets to take over the time-consuming manual classification procedures[240,160,6,56,19,243,91,237,244].

The pattern discussed here (see Figure 5.16) was obtained with the Jungfrau scattering detector[146,96] from an isolated argon cluster using a photon energy of 1000 eV. The large-area diffraction detector, containing 2048×2048 pixel, was placed at a distance from the interaction region that allows the recording of scattered light up to a scattering angle of 13°.

It is possible to derive *via* Equation 5.23 the equivalent real-space pixel size of the pattern shown in Figure 5.16a. As 1000 eV corresponds to a wavelength $\lambda = 1.24$nm, the pixel size in real space is $\delta = \frac{1.24\,\mathrm{nm}}{2\sin(13°)} \approx 2.7\,\mathrm{nm}$, which is the real-space dimension of a single pixel in the reconstruction shown in Figure 5.16c. In reality, the area of meaningful SNR covers only around 5 % of the actual matrix surface, which has two main implications. First, a successful reconstruction in these brightness conditions could be attempted when the sample size is small enough to reach an oversampling ratio $\sigma \gtrsim 40$[am]. Furthermore, the spatial distribution of this significant data is, as expected, focused around the centre and only reaches one third of the full detector dimension, which corresponds to a scattering angle of roughly 4°. Thus, the effective minimum size of features that can be spatially resolved are around three pixels, and no information below this dimension can be retrieved. This is immediately visible in the reconstruction shown in Figure 5.16, where features that should be in principle sharp, like the cluster edge, are instead smoothed over few pixels.

The discussion made so far is mainly qualitative. A formally correct treatment and evaluation of the actual resolution of CDI would involve not only a more careful analysis

[am] An additional problem that may affect experimental data comes from the signal saturation in high-intensity pixels, as detectors are capable of recording signal up to a maximum value. Those areas where the detector's signal is saturated cannot be used for imaging and thus need to be excluded similarly to the missing pixels in the central hole. However, this is a merely technical limitation, and new detectors are less and less affected by this problem, thanks to their high *dynamic range*.

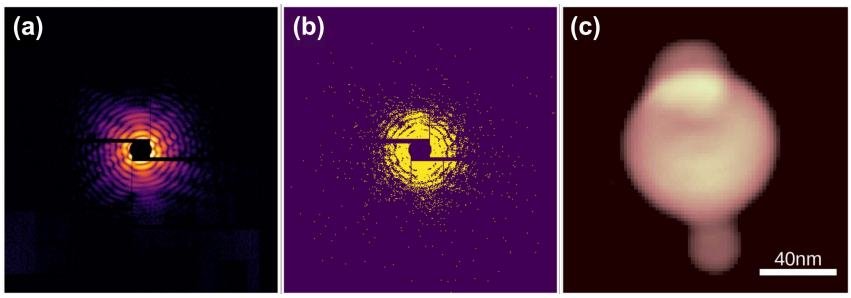

Figure 5.16: Example of real FEL experimental data[189] from the Maloja instrument at SwissFEL[215]. (a) Experimental diffraction pattern. (b) Region of photon counts greater than 1, highlighted in yellow. (c) Absolute value of the reconstruction retrieved from (a). The argon cluster in the reconstruction appears as an agglomerate of 3 spheres of different sizes (see Section 5.3.1). Note the brighter signal in the reconstruction where two spherical sub-clusters overlap, visualizing that small-angle CDI has access to the projection (*i.e.* integral) of the optical properties along the beam propagation direction. Courtesy of Mario Sauppe (ETH Zürich).

of the SNR, but also an evaluation of the reconstruction process itself[an]. To take into account the latter aspect, statistical methods that involve many reconstruction processes are employed, like the Phase Retrieval Transfer Function[223,109]. This aspect goes beyond the scope of this chapter, and we suggest Reference [109] for further information.

5.2.3 Wide-angle Coherent Diffraction Imaging

As introduced in Section 5.2.1, the wide-angle regime is reached when the component of the recorded momentum transfer parallel to the beam propagation direction $q_{\parallel}$ becomes non-negligible, and in reciprocal space, the portion of the *Ewald sphere* covered by the detector cannot be approximated any more by a flat surface.

Coming from the perspective of the *small-angle* scattering regime, it means that the Fourier Slice Theorem is no longer applicable, and not only the 2D projection of the sample refractive index, but its three-dimensional distribution affects the scattering signal. This last sentence is formulated in terms of the *direct scattering problem* (*i.e.* how to simulate the scattered field from a density distribution) and tells us that the full knowledge of the 3D sample morphology is required to achieve a wide-angle scattering simulation.

If we approach the topic under the *inverse scattering problem* point of view, *wide-angle* CDI allows to capture, in a single two-dimensional diffraction shot, three-dimensional information on the sample. Under this view, this technique opens the exciting possibility for the study of ultrafast phenomena by capturing three-dimensional movies of nanomatter.

[an]The fact that the diffraction data contains information up to a maximum spatial resolution does not imply that phase retrieval algorithms are then really able to achieve it.

The reason why, so far, no such movies have been experimentally demonstrated is due to intrinsic complications of wide-angle data analysis, which is an active field of research.

Dealing with the third dimension

Similarly to what has been presented in Section 5.2.2, we now identify the spatial resolution of wide-angle scattering. It depends on the maximum momentum transfer at which data is recorded, which reaches different magnitudes on the orthogonal direction $q_\perp$ and parallel direction $q_\parallel$. Considering the geometry in Figure 5.3, we find $|\vec{q}_\perp(\theta)| = |\vec{k_0}|\sin(\theta)$ and $\left|\vec{q}_\parallel(\theta)\right| = |\vec{k_0}| \cdot [1 - \cos(\theta)]$. The theoretical *half-period* resolution (see Section 5.2.2) on the orthogonal plane $\delta_\perp$ and on the depth axis $\delta_\parallel$ can be then calculated as:

$$\begin{aligned} \delta_\perp &= \frac{2\pi}{|\vec{q}_\perp(\theta_{\max})|} = \frac{\lambda}{\sin(\theta_{\max})} \\ \delta_\parallel &= \frac{2\pi}{\left|\vec{q}_\parallel(\theta_{\max})\right|} = \frac{\lambda}{1 - \cos(\theta_{\max})} \end{aligned} \tag{5.27}$$

Two fundamental considerations must be examined before diving into the data analysis methods. First, significant values for $q_\parallel$ when compared to $q_\perp$ start to appear at $\theta_{\max} = 20°$, where $\delta_\parallel \approx 6\delta_\perp$. Due to the $1 - \cos(\theta)$ in the denominator in Equation 5.27, the increase in depth resolution is dramatic for a scattering angle of 30°-50°. However, the strong decrease in the scattering signal makes it challenging to measure data at such high scattering angles in practice (see discussion in Section 5.2.2).

A second, even more determining aspect is that the information is only partial. In the *small-angle* scattering regime, knowledge about the 2D amplitude of the field scattered by a 2D sample is almost[ao] complete, such that "only" the phases have to be retrieved. When moving to the three-dimensional case, the Fourier representation of the 3D scattering density ρ lies in three dimensions as well, but only a 2D slice of it (the *Ewald's sphere*, see Figure 5.3)) is known.[ap]. Additional strong constraints are, then, necessary to approach 3D imaging from single wide-angle shots. Furthermore, the fact that the

[ao] due to the presence of a hole in the detector, as well as noise in the data (see Sections 5.2.2 and 5.2.2).

[ap] A direct extension of the small-angle approach to the wide-angle case is, in principle, straightforward under a numerical point of view. The density function ρ and its support function S can be defined as three-dimensional tensors, and 2D phase retrieval algorithms can be directly generalized to the 3D case without substantial modifications. This approach is known in literature as *Ankylography*[171]. However, since its disclosure to the scientific community, the method has raised doubts about its consistency and reliability[234], due intrinsic "dimensional deficiency" that renders the 3D case an *ill-posed* problem. A straightforward definition of "ill-posed problem" says that such problems either have no solutions, or too many, or the procedure to reach them is unstable (see Reference [106] for a generic introduction to the topic). This deficiency derives from the action of the projector $P_\mathfrak{l}$ (see Section 5.2.2) which, in this case, constrains only a tiny fraction (just on the Ewald sphere) of the total amount of Fourier amplitudes. For this reason, Ankylography turned out to be impractical for real applications, as the loose intensity constraint cannot ensure a unique solution to the phase problem.

intensity constraint is not strong enough has also the practical implication that information cannot be effectively "back-propagated" to the real space. For these reasons, the most effective wide-angle single-shot imaging approach so far attempted is based on *fitting forward simulations of constrained sample's models*.

The three-dimensional imaging problem

Coherent Diffraction Imaging based on forward fitting is strictly related to the optimization problem encountered in the small-angle inverse scattering problem. In particular, it can be expressed in terms of an optimization problem similarly to Equation 5.14:

$$\vec{p}_{\text{sol}} \equiv \{\vec{p} : E[\vec{p}] < E[\vec{s}] \,\forall\, \vec{s} \neq \vec{p}\} \tag{5.28}$$

Here, the dependence on the matrix ρ has been replaced with a more generic vector $\vec{p}$, which contains the *parameters* necessary to define the sample properties depending on the *model* in use. For example, in the case of a simple sphere with uniform refractive index, $\vec{p} = \{r, \delta, \beta\}$ because the architecture of a homogeneous sphere and its response to the incoming light are completely defined by its radius and its refractive index $n = 1 - \delta + \mathrm{i}\beta$.

Similarly to the small-angle case, the optimization target E in Equation 5.28 tells us how much the density reconstruction $\rho(\vec{p})$ defined by the set of parameters $\vec{p}$ is compatible with the experimental diffraction pattern I, given by

$$E[\vec{p}] = \|I - S(\vec{p})\|\,, \tag{5.29}$$

where $S(\vec{p})$ is a function that *simulates* the diffraction pattern (*i.e.*, that solves the *direct scattering problem*) for a scattering density defined by the parameters $\vec{p}$.

The minimization problem (Equation 5.28) of the error function E (Equation 5.29) makes it clear why this imaging approach is based on *fitting* of *forward simulations*. In regards to the *fitting* aspect, there are different strategies to deal with the *minimization* of $E[\vec{p}]$ as a function of its parameters $\vec{p} = \{p_1, p_2, ...\}$. This topic is not strictly related to coherent diffraction and will not be treated here. Some applications of peculiar optimization strategies applied to CDI can be found in References [42] and [44]. Independently on the employed approach, all optimization algorithms require a large amount of evaluations of the optimization target E, which turns into the evaluation of the *simulation function* S. For this reason, fast and effective simulation methods are fundamental building blocks for wide-angle single-shot three-dimensional coherent diffraction imaging based on fitting of forward simulations, as discussed below.

Forward simulations

Forward simulation methods can be used for solving the *direct scattering problem* (*i.e.* for calculating the field scattered by a real-space distribution of a sample's electronic density). In principle, the scattered field can be computed *exactly* by solving Maxwell's equations for light traveling in the sample. For very simple sample shapes, the field equation can

be even solved analytically, like in the case of spheres with uniform refractive index, or spherical core-shell structures. Their analytical solutions are known as *Mie solutions*, and come with the great advantage of providing extremely fast and accurate simulations of the scattering signal. However, the main drawback is the limited range of applicability.

Still, Mie simulations are being proficiently used to retrieve information from architecturally simple systems[31], like uniform nanodroplets of superfluid helium (see Figure 5.17) or core-shell arrangement of neutral and and ionized matter in spherical xenon clusters[182].

The topological restrictions of Mie simulations can be overcome by numerically solving Maxwell equations, for example *via* Finite Difference Time Domain (FDTD) simulations[217,229] or using Green's function based approaches such as the discrete dipole approximation (DDA)[170,187]. However, these simulations methods are unpractical for fitting procedures due to their high computational cost[aq]. In this context, approximate simulation methods come into play.

Among approximated approaches to the direct scattering problem, the three-dimensional FT of the scattering density ρ (see Section 5.2.1) is by far the most efficient and straightforward, in numerical terms. Still, this method relies on the Born approximation which completely neglects any interaction between light and matter apart from the single scattering events. Thanks to the material's refractive index value being close to one in the X-ray regime, this approximation is sufficient to interpret the output of phase-retrieval results as the projection of the sample's optical properties[ar]. However, its deviations from the exact field are strong enough, expecially in the XUV energy range and at high scattering angles, to prevent successful imaging attempts[12].

It has been demonstrated that first-order "corrections" to the Born's approximation restore sufficient similarity between the exact and simulated field to allow forward fitting approaches[12,44]. When a monochromatic plane wave propagates in matter with constant refractive index $n = 1 - \delta + \mathrm{i}\beta$ in a direction z, its electric field $E(z)$ is described by the plane wave:

$$E(z) = E_0 e^{\mathrm{i}k_0 nz} = E_0 e^{\mathrm{i}k_0(1-\delta+\mathrm{i}\beta)z} = E_0 e^{\mathrm{i}k_0 z} e^{-k_0\beta z} e^{-\mathrm{i}k_0\delta z} = E_0 e^{\mathrm{i}k_0 z} C(z,\delta,\beta) \qquad (5.30)$$

Here, E_0 is the incoming field amplitude and k_0 is the radiation wavevector. In practical terms, this wave can be split into two components. The first component $E_0 e^{\mathrm{i}k_0 z}$ is the equation of a monochromatic field travelling in vacuum (where $\delta = \beta = 0$). The second term $C(z,\delta,\beta) = e^{-\beta z} e^{-\mathrm{i}k_0\delta z}$ is a complex function which encodes the modification of the field's amplitude $e^{-\beta z}$ and phase $e^{-\mathrm{i}k_0\delta z}$. The imaginary part β of n is often called the *absorption coefficient*, and causes an exponential decrease in the field strength[as].

[aq] The time-to-solution (*i.e.* for a single simulation) is a pivotal aspect when dealing with fitting routines

[ar] *i.e.*, for phase retrieval results, the Born approximation means that the retrieved density is an approximation of the refractive index projection. Stronger deviations from this approximation make such an interpretation more incorrect, but do not prevent in most cases the convergence of phase retrieval algorithms to a reconstruction strongly connected with the sample's topological properties.

[as] This is the well-known Beer-Lambert law[14]. Johann Heinrich Lambert already noted, back in the 18th century, that light is exponentially absorbed by matter depending on the material thickness.

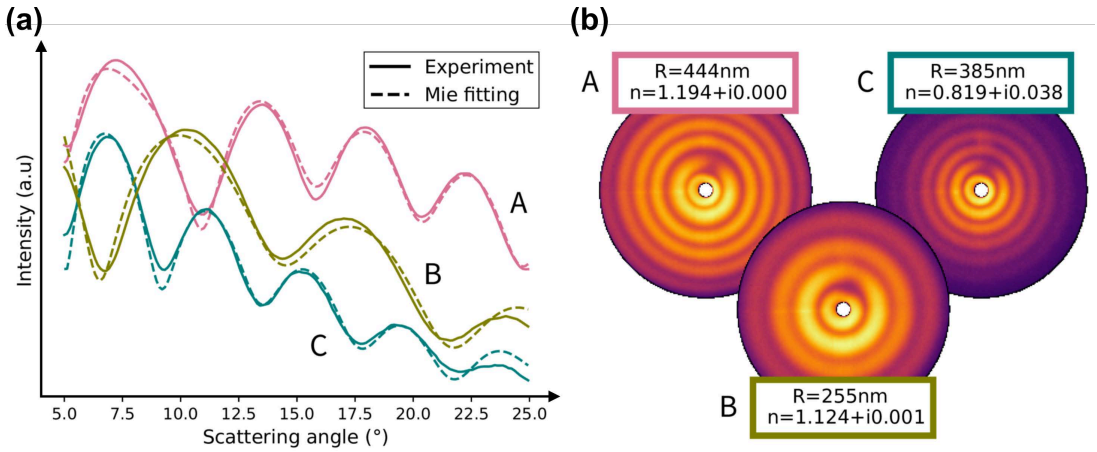

Figure 5.17: Example of wide-angle imaging performed *via* Mie fitting. Helium nanodroplets are imaged[94] at a photon energy of 21 eV at the LDM instrument of FERMI[131]. (a) Experimental radial profiles of three different diffraction patterns, and respective Mie fits. (b) Values of radius R and complex refractive index n resulting from the fitting of the radial profiles are assigned to the respective diffraction pattern[94]. Courtesy of Linos Hecht (ETH Zürich).

Conversely, δ, also known as *refraction coefficient*, modifies the "effective wavelength" of the radiation, thus introducing a phase-shift of strength $k_0\delta z$ with respect to light travelling in vacuum.

It is possible to apply this correction factor C to a simulation made *via* the Born approximation, by subdividing the sample into slices in the real domain (see Figure 5.18). The scattering for each slice is then computed by using an electric field that has been shaped by the previously encountered slices[43]. This approach is based on the Multi-Slice Fourier Transform (MSFT), an efficient method to compute partial 3D Fourier Transforms[47,202,172] (see also Figure 5.20 below).

However, the MSFT approach previously presented is again not good enough when moving towards larger values of the refractive index commonly found in the XUV regime and/or close to the material's electronic resonances. This incompatibility comes from two physical effects that are still neglected. On the one hand, Equation 5.30 exactly tells us how light travels within a uniform medium, but does not describe the refraction effects caused by interfaces of different materials (or between the sample and vacuum). In fact, when the refractive index is a function of the spatial coordinates, gradients of $n(\vec{r})$ lead to the deviation of light, such that the approximation of a plane wave is no longer valid within the sample when the value of such gradients becomes appreciable. On the other hand, the light scattered by a given sample slice (see Figure 5.18) still interacts with the subsequent slices (*i.e. secondary scattering* can happen). Simulation methods which, at least partially, include these "second-order" effects are fundamental to deal with wide-

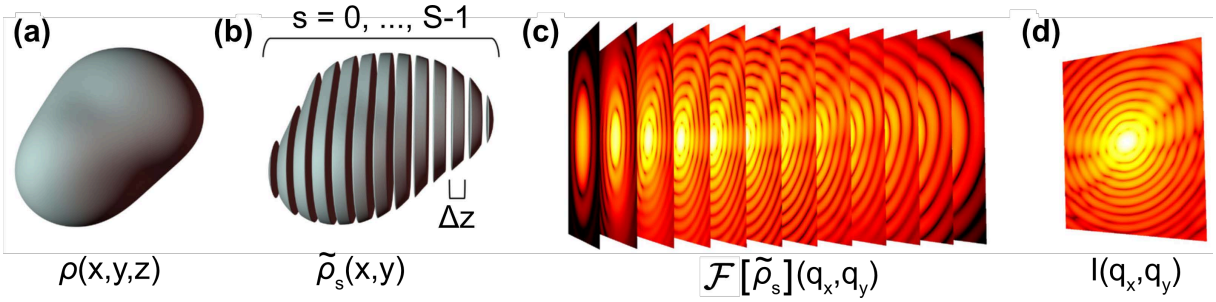

Figure 5.18: MSFT-based simulation method. (a) Rendering of the 3D sample density. (b) The density domain divided into slices. (c) The field scattered from the slices, obtained by combining the slices refractive index with the field shaped by the preceeding ones. (d) The final diffraction pattern is obtained from the sum of all the slices fields. Figure adapted from Reference [43] with permission of the corresponding author.

angle CDI of samples whose refractive index varies more than $\approx 5\,\%$ from vacuum, as highlighted in Reference [43]. Improved methods are under development[226], which would dramatically increase the range of applicability of forward fitting methods for CDI.

5.3 Imaging the morphology of clusters

The diffraction-before-destruction principle was first demonstrated on a nanostructure etched into a membrane[36] using a single pulse from the first short-wavelength FEL FLASH in Hamburg[193,176]. Shortly after, also first single-shot single-particle CDI experiments were carried out on aerosols[22,21], atomic clusters[29], nanoparticles[20,128], and single viruses[57].

For many systems, structure determination is typically the main goal of single-particle CDI. The fragility of "soft matter" systems, such as viruses or membrane proteins as a strong motivator for single-particle CDI was already mentioned. Also studies on aerosols, such as soot nanostructures, were guided by the goal of avoiding structural changes during deposition[22,21,127]. In contrast, cluster experiments usually investigate light-induced dynamics, and determining the particle morphology is therefore rather a characterization step. Nevertheless, lightly bound and short-lived rare-gas clusters and nanodroplets cannot be deposited and studied with electron microscopy. Therefore, CDI provided for the first time direct insight into their structure. While metal nanoparticles are much more stable towards deposition on a substrate, gas-phase produced metal clusters are also known to change their structure during landing on a surface[110,231]. Results on the morphologies of both cluster types are presented below. We also recommend the review article by Sun and colleagues[215], which gives a compact overview of single-particle CDI experiments, highlighting the Maloja endstation at SwissFEL as an ideally suited instrument for this

line of research.[at]

5.3.1 Understanding the growth of rare-gas clusters

Rare-gas clusters are generated by expanding gas at a certain temperature and pressure from a reservoir through a small nozzle into vaccuum[88,199]. In this supersonic jet, the random velocities of the gas atoms in the reservoir are transformed into directed motion, and the relative velocities (and thus the gas temperature) drop dramatically. Accordingly, the trajectory in the phase diagram may cross the vapor pressure curve and condensation sets in[88]. As the atomic density drops along the jet, monomer addition becomes less important, but the clusters can keep growing by coagulation of smaller clusters into larger ones. Theoretical simulations explaining experimental size distributions confirmed this physical picture of monomer addition and coagulation[210]. But without any single-particle imaging methods available for these fragile systems, it remained unclear whether the energy freed in the coagulation events suffices to re-melt the two clusters into a spherical single cluster or whether a non-spherical shape would freeze out[au]. Indeed, CDI of individual xenon clusters revealed that spherical clusters are produced in parallel[av] to twin and triple shapes up to hailstone-like particles[29,178,179] (see representative images from recent high-resolution CDI experiments[189,215] in Figure 5.19a).

5.3.2 Structures of helium nanodroplets and embedded dopants

Helium nanodroplets can be considered the prototypical model system for light-matter interaction studies as they remain liquid[aw] and can therefore not freeze-out in non-spherical shapes as the other rare-gas clusters do. Also, the electronic structure can be assumed to be simple: the atoms contain only two electrons and are very weakly bound. Nevertheless, helium nanodroplets exhibit a plethora of unexpected and quite fascinating phenomena related to their superfluidity that are a lively topic of current research and have been reviewed recently in a book[209]. Here, we give a brief summary on CDI of helium nanodroplets and hightlight a few examples and else refer to the CDI chapter[220] in the above mentioned book and a review paper[80]. The large body of original

[at] In terms of structure determination methods closely related to single-particle CDI, we want to mention experiments at higher photon energies, where X-ray diffraction is sensitive to the crystal lattice of the object under study. Single-shot single-particle Bragg diffraction has been obtained from rare-gas clusters[69] and water / ice microdroplets[203,63]. Another novel CDI-related technique is in-flight holography[85] using simple-structured strong scatterers such as xenon clusters as reference objects for Fourier transform holography of single viruses.

[au] This is only relevant for the noble gases neon, argon, krypton and xenon, as helium clusters remain liquid even though they cool to temperatures below 1 K. Their morphology is discussed in the following section.

[av] This agrees well with Bragg diffraction studies on single rare-gas clusters, finding that individual clusters had either fcc or hcp crystal structure, or were phase mixes, probably from twinned clusters[69].

[aw] Helium refrains from freezing up to high pressures even at 0 K.

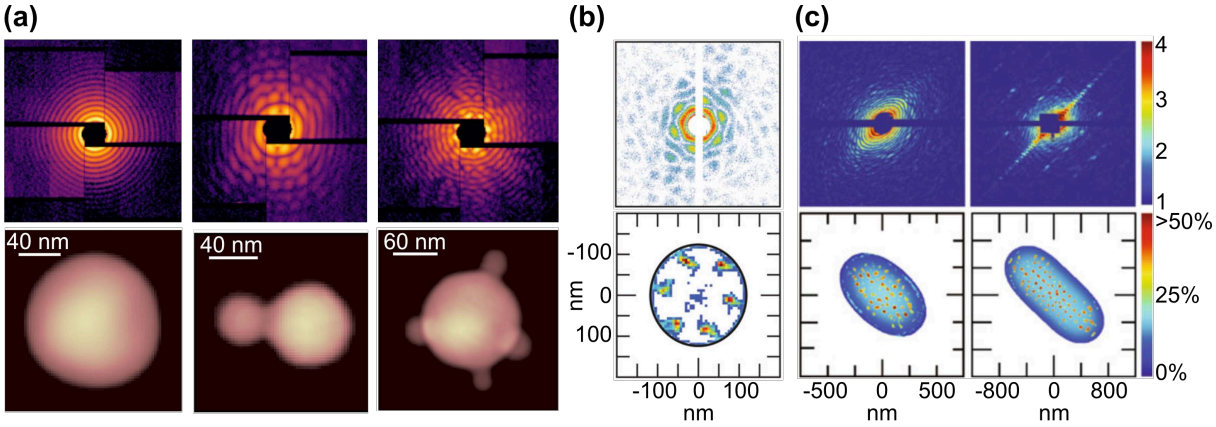

Figure 5.19: Small-angle CDI results on rare-gas clusters and helium droplets. (a) Large argon clusters grow by coagulation. Often, spherical shapes are reached but also twin structures or hailstones are formed. Diffraction data[189] obtained at the Maloja instrument at SwissFEL[215], courtesy of Mario Sauppe (ETH Zürich). (b) Diffraction pattern and reconstructed density of a spherical ^{4}He droplet with xenon-dressed vortex lattice[105]. Reprinted with permission of American Physical Society, Copyright 2016. (c) Patterns and reconstructions of strongly deformed oblate and prolate helium droplets reveal that they also contain vortex lattices[157]. Reprinted with permission from American Physical Society, Copyright 2020.

work[81,218,105,16,181,122,157,230,65,219,66,227], however, testifies that CDI of helium nanodroplets has become a very successful branch of X-ray FEL science on its own.

In the pioneering experiment of the Vilesov group and collaborators[81], liquid helium was sprayed into vacuum forming nanodroplets. From the diffraction patterns in this and subsequent experiments[81,16,181,122], it became obvious that while the majority of droplets were indeed round, some deviated from spherical shape up to rare, quite strongly deformed shapes. Furthermore, many droplets contained dense lattices of quantum vortices[81,218,105,157], a fascinating phenomenon made visible by doping the helium droplets with xenon atoms (see Figure 5.19b,c).

While quantum vortices in ^{4}He are a very interesting phenomenon, they can also be an obstacle for certain research directions: in the presence of quantum vortices, most atoms or molecules picked up by a droplet get stuck at the vortice sites[46]. This disturbes, for example the study of how electrons distribute on the surface of a charged droplet[66] and dominates the arrangements of nanostructures forming in the ultracold environment[81,218,105,157] instead of being governed by the mutual interaction between the dopant atoms or molecules[221]. In this regard, a recent collaborative study could clarify regimes for the creation of vortex-free nanodroplets up to a size of 10^8 atoms[227].

A profound understanding of the shapes of spinning liquid droplets could be developed, both in the presence[230,65] and absence[81,16,181,122] of friction, tracing them from round to

oblate to prolate shapes, rather closely following classical predictions[122] (see examples of oblate and prolate droplets, identified from their features at wide scattering angles in Figure 5.20a).

5.3.3 Metal clusters and nanoparticles

Early CDI experiments of metal clusters created in a magnetron sputter source[87] with wide-angle CDI (see also Section 5.2.3) revealed a number of very symmetric, streaked patterns[12], which were analysed *via* forward-fitting based on ideal polyhedron models. The matches indicated that structural motifs such as icosahedra or dodecahedra which are only energetically favourable at very small sizes persist up to very large sizes under the rather cold growth conditions applied in the experiment[12]. Only through the development of a more general forward-fitting algorithm[43,44], it became possible to detect imperfections that result from the rather extreme growth conditions, such as rounded edges, mixed structural motifs, and even agglomerates (see Figure 5.20b).

Besides creating metal clusters in the gas phase, it is also possible to wet-chemically produce metal nanoparticles (and other materials) and spray them into vacuum. This approach has gained importance for time-resolved experiments as both spraying[18] and particle production techniques[169,132,154] have matured over the last years. Metal nanoparticles are now available in a broad range of materials (or combinations thereof) and shapes, with narrow distributions of size and shape[10]. While they can be pre-characterized *via* electron microscopy, the CDI characterizations often show deviations[162] that can be induced by the spray solvent or through the size selection effect of CDI[117], enhancing the large tail of a broad size distribution.

5.4 Clusters in intense short wavelength pulses

Our current understanding of the interaction between intense X-ray pulses and nanoscale matter has been largely developed in experimental and theoretical work on clusters. In this section, the experimental and theoretical findings are presented in the framework of a generally accepted physical picture of the dynamics proceeding in three phases. This model was developed in the XUV regime and refined in the X-ray range. We recommend the chapter by Bostedt et al.[33] in Reference [104], where the development is discussed by wavelength regimes from near-edge photon energies to phenomena involving core electrons. Particularly clear insights on X-ray induced dynamics have been gained by the novel method of combined single cluster imaging and ion spectroscopy, which will be also introduced in the following.

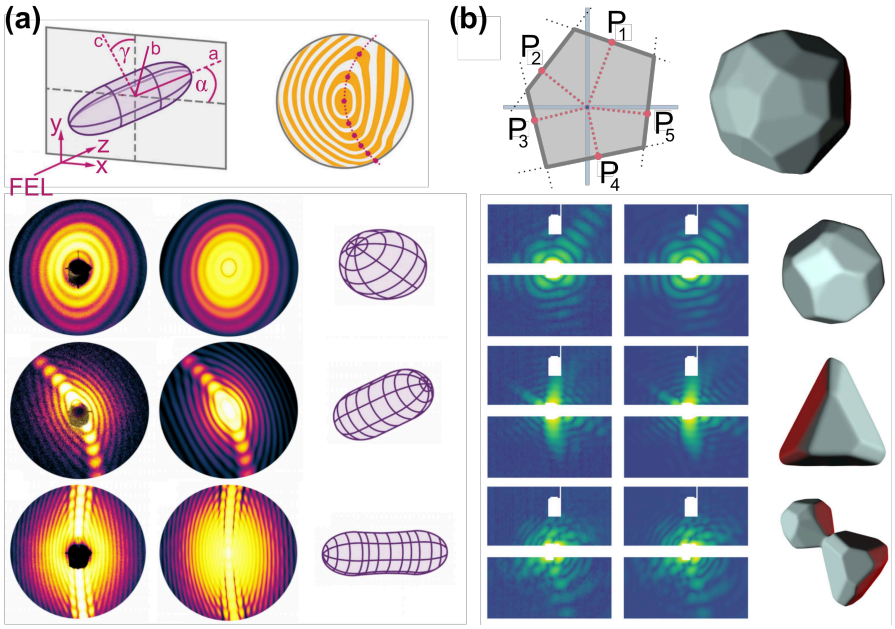

Figure 5.20: Three-dimensional structure determination *via* single-shot wide-angle CDI. (a) Imaging results on spinning superfluid helium nanodroplets. A simple parametric shape model is used and peculiar features produced in a wide-angle diffraction pattern guide the fitting (upper row). Experimental data (left column) and simulated patterns (central column) match well, revealing oblate, elongated architectures of the helium droplets (adapted from Reference [122] with permission of the corresponding author). (b) 3D imaging results on silver clusters with shape parametric model (upper row) constructed by flat facets that define a compact domain in space. Experimental data (left column) and retrieved patterns (center column) and 3D shapes (right column) of single silver clusters and agglomerates (adapted from Reference [44] with permission of the corresponding author).

5.4.1 The role of cluster experiments at short wavelength FELs

Clusters are ideal model systems of solid density but isolated in the gas phase[173]. Compared to bio-molecules, their complexity is drastically reduced. Rare-gas clusters, as the prototypical target for laser-matter interaction experiments, are easily created by expanding gas through a small nozzle into vacuum. Typically, the average cluster size can be chosen *via* the expansion conditions[88], thus scaling the parameters from single atoms and dimers to a few hundreds, millions, or even 10^{11} atoms per cluster, bridging the regimes of atomic / molecular physics and solid state physics. Also, a wide range of other materials or combinations of materials can be used for creating nanoscale particles that either form in or can be brought into the gas phase. Because of their rather simple handling on the one side and the strong measurement signals obtained on the

other, atomic clusters have very regularly been the target of choice in experiments in the start-up and commissioning phases of short-wavelength FELs and their respective endstations[233,28,29,176,62,27,32,131,156,121,238,77,200,104,2,215].

Already the first experiments on clusters at the XUV-FEL FLASH[233], at that time still called *Tesla-test facility 2*, started out with a surprise; the ionization states measured were higher than expected, and in particular higher than or at least almost as high as the ionization states of atomic gas irradiated with the same intensities[233,232,196]. In the long-wavelength regime, due to *inverse bremsstrahlung heating*[ax] and subsequent impact ionization, the interaction with clusters is always producing higher charge states as with atomic gas[51], but this process scales with the square of the wavelength and thus should have negligible influence in the VUV and XUV regime[183]. Sparked by the first interesting observations, a large number of theoretical works[184,188,208,183,241,67,9,242,3,4,161,114,159] and subsequent experimental studies at FELs[232,119,120,26,98,224,75,30,31,83,194,225,76,156,121,148,147,216,84,73,180,69,115,116,97,185] and HHG sources[196–198] were carried out, leading to an ever deeper understanding of the key mechanisms in the short wavelength regime.

5.4.2 Interaction model in three phases

In a widely accepted simple model[233,183], we view the intricate evolution of clusters induced by intense short-wavelength pulses as a dynamics in three phases (see Figure 5.21). At the beginning of the short-wavelength pulse, the individual atoms of the clusters are photoionized, analog to isolated atoms in a gas, and the cluster environment plays only a minor role. This is in particular true for van-der Waals bound rare-gas clusters with atomic-like electronic structure. Photoionization in the short-wavelength regime, even with very intense pulses, is dominated by sequential single-photon absorption[211,79]. Transient resonances in the ionisation sequence can play an important role[108,177,137,174,117]. At higher photon energies inner-shell holes are created followed by Auger-Meitner decay and thus the creation of additional free electrons[9].

The second phase starts when electron emission, or 'outer ionization', becomes frustrated and a nanoplasma is formed[26,9]. Still, 'inner ionized' electrons are separated from their parent ions but they stay bound to the charge of the cluster compound. Further interaction channels open up, such as electron impact ionization[3,147]. The distinction between *inner and outer ionization*[124] was already used in the IR regime, where the initial ionization by multiphoton absorption or tunneling leads to electrons without any residual energy that subsequently are accelerated in the slowly changing electromagnetic field[112,183]. Already the first few electrons are thus bound to the cluster compound until

[ax]The mechanism is called inverse bremsstrahlung because energy is directly transferred from light field to electron. A free electron in vaccuum gains kinetic energy in a light pulse but it looses it again when the pulse is over, as it just follows the light field. Scattering events occurring in a dense nanoplasma, however, bring accelerated electrons out of phase with respect to the light field, and the free electrons can thus accumulate energy.

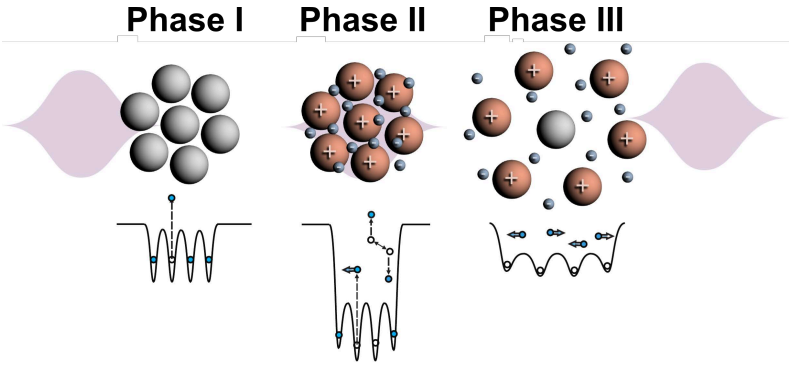

Figure 5.21: Simple picture of laser-cluster interaction in three phases. Phase I: on a few-femtosecond time scale, the atoms are photo-ionized and the cluster environment plays a minor role. Phase II: through charging, the cluster potential becomes deeper and electron emission is frustrated. A nanoplasma forms and evolves during the tens or hundreds of femtosecond pulse. Phase III: the cluster disintegrates within few pico- to nanoseconds. Also, recombination and relaxation processes take place. Potential wells adapted from reference [9] with permission of the corresponding author.

they become hot enough to leave the cluster. In the short wavelength regime, the formation of a nanoplasma is instead delayed due to significant *residual energy* of the electrons[ay], that allows them to leave the cluster until it has accumulated a charge creating a potential as deep as the residual energy[26,8]. The turning point of frustrated emission can be estimated *via* the frustration parameter[9] that compares the number of created plasma electrons with the number of electrons that can leave the cluster, the latter being estimated from the simple equation of a probe charge leaving a charged sphere's surface.

In case of an ongoing irradiation after emission frustration, a cloud of quasi-free electrons is formed and subsequently thermalizes. Its hot tail can boil off[120,30], resulting in further charging and deepening of the cluster potential. Until ionic motion becomes significant, only a few processes can add or take energy from the electron cloud. In addition to cooling by thermal emission[30], energy can dissipate by inelastic collisions of electrons with atoms or ions in the cluster (*i.e.* impact ionization or collisional excitation[147]). A gain in electron temperature results from ongoing photoionization[8] as every new electrons brings in the residual energy, and from recombination of the slowest plasma electrons with cluster ions[180], which returns the binding energy to the remaining plasma *via* a second involved electron in a three-body collision. The ionic motion can however set in very fast[83] and proceed quite far already during the pulse, in particular at high photon energies, high pulse intensities, and for small cluster sizes, thus the clear separation here is a limitation

[ay]This is the difference between photon energy and electron binding energy, or, in case of Auger-Meitner electrons, between the energy gained by relaxing one electron and the binding energy of the other.

of the simplified three-phase model.

Finally, during the third phase, when the interaction with the pulse is over, the highly excited cluster nanoplasma will disintegrate by *Coulomb Explosion* and/or *Hydrodynamic Expansion*, depending on the net charge on the cluster and the temperature of the electron cloud[9] (see Figure 5.22). Also recombination and relaxation processes are important in this phase[197,115]. While the ionization states reached within clusters and atomic gas during irradiation are similar[211,195], the final measured ionization states are usually much lower[233,232]. In the dense and fully screened part of the cluster nanoplasma, collisional processes can not only increase the charge states, they particularly also contribute to three-body recombination and thus to a lowering of the charge states[98,180]. However, recombination often occurs into highly excited Rydberg states[198] that can be re-ionized late in the disintegration, e.g. by the constant electric field of the spectrometer, which can thus increase the observed ionization states again[68].

Pure *Coulomb Explosion* occurs when all created electrons have left the cluster and it carries a positive net charge. In this limit case (which is physically possible) the subsequent disintegration is directly driven by the repulsion of the positively charged ions. A characteristic feature of Coulomb Explosion is a homogeneous intensity drop (see Figure 5.22a).

In the limit of *Hydrodynamic Expansion* (see Figure 5.22b), all created electrons have been captured by the cluster potential and screen the ions. Therefore the dense nanoplasma is net-neutral. However, the electron temperature is non-zero, thus the electron cloud will spill out of the ionic background, leading to a gradual surface softening[84,162] while inner ions stay screened and still until the ongoing expansion reaches them or they have recombined fully[73,180]. To understand the energy transfer mechanism, also referred to as *expansion cooling*, a simplified microscopical view is instructive: Fast electrons in the nanoplasma can propagate freely through the field free inner of the cluster, where the ions are screened by other electrons. When they reach the surface, entering vacuum, they leave a positive net-charge behind, pulling them back into the cluster. While they remain outside of the cluster, the surface ions are only partially screened by the electron cloud and feel a mutual repulsion. The ions accelerate away from the cluster, flattening the cluster potential. In consequence, the returning electrons will not regain their full previous velocities[az].

We note that in reality, a net-neutral nanoplasma can only be an approximation; for a finite electron temperature some electrons will always be able to leave the cluster compound. A more realistic (and in case of moderate electron temperatures as created in the XUV regime even pretty accurate) picture is the combined Coulomb Explosion of the shell and Hydrodynamic Expansion of the core[224,161]. Plasma electrons are pulled into the centre of the cluster, fully screening it and leaving an unscreened surface of ions which Coulomb explodes quickly, and a remaining quasi-neutral nanoplasma dissolving

[az] We note that it is of course also a Coulombic interaction that drives *Hydrodynamic Expansion*. This has been realized early on[145,9], but the name has led to some confusion[125].

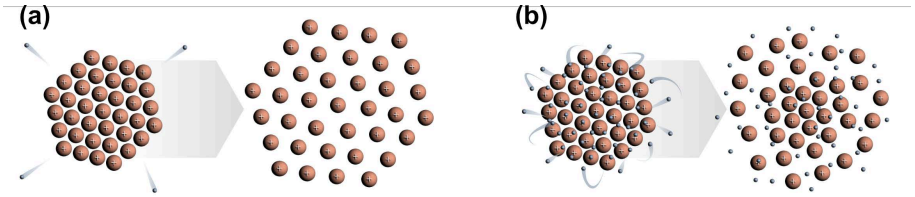

Figure 5.22: Schematics of (a) Coulomb Explosion, resulting in self-similar expansion, and (b) Hydrodynamic Expansion, leading to surface softening.

by Hydrodynamic Expansion.

5.4.3 A new quality with single cluster imaging and simultaneous spectroscopy

Conventional cluster experiments on ensembles of clusters suffer from averaging over cluster size distributions and laser intensity profiles, washing out characteristic signatures[103]. A new quality of experiments was reached by combining single-cluster imaging and simultaneous spectroscopy of ion time-of-flight spectra[29,83,180,185] (see also Figure 5.2). The diffraction pattern allows to determine particle size and FEL intensity, while ionic residuals of the interaction are measured simultaneously and sorted in post-processing on the information from the diffraction image. Also other residuals are possible to be combined with CDI such as electrons, fluorescence, or stimulated emission from clusters[15].

While ion spectra obtained from ensembles of clusters are dominated by the contribution from the wings of the focal intensity distribution[83], the brightest single-shot single-cluster spectra from xenon clusters irradiated with intense X-ray pulses yielded only high charge states, giving new insight into suppression of recombination and triggering a discussion of the contribution of re-ionization long after the interaction[197,198]. At reduced intensities and using helium nanodroplets as a more weakly interacting target, the full transition from Coulomb Explosion to Hydrodynamic Expansion could be mapped[185]. From the single-cluster spectra of xenon clusters irradiated by an order of magnitude smaller photon energy, the imprint of recombination and its previously unrecognized contribution to plasma heating was found[180].

5.5 Time-resolved imaging of structural dynamics

The femtosecond snapshots taken with single-shot single-particle CDI make the method also ideally suited for resolving changes in nanoparticles in time and space after irradiation with an optical[ba] laser pulse (see Figure 5.23).

[ba] X-ray induced dynamics can be studied by capturing two consecutive images of the same particle in X-ray-pump X-ray-probe measurements. This, however, requires ways to separate the overlaying diffrac-

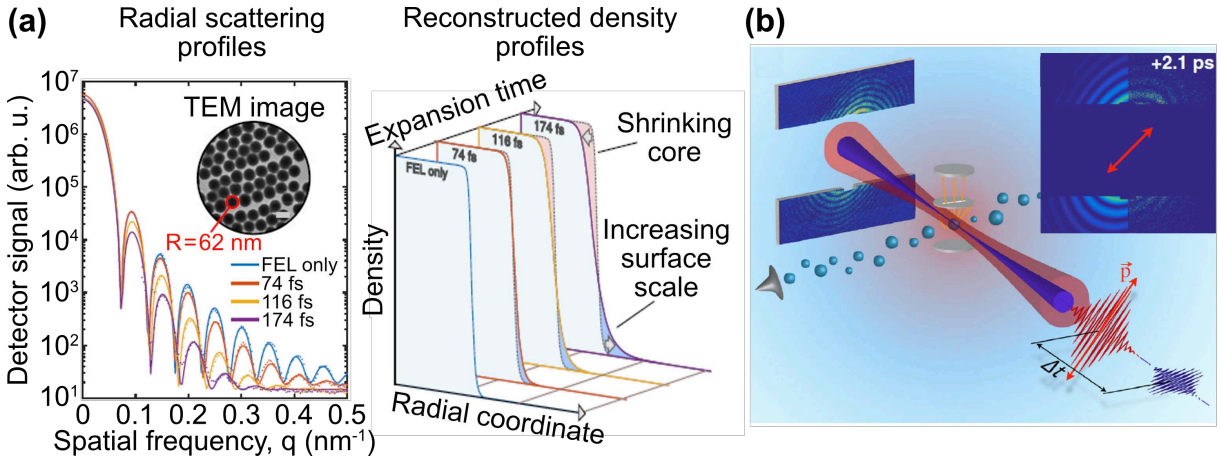

Figure 5.23: (a) Radial profiles of diffraction patterns from NIR excited nanoparticles show a decaying large-angle signal with delay. Thickness of solid core and softened surface can be reconstructed. Adapted from Reference [162] with permission of the corresponding author. (b) Sketch of experimental setup and diffraction patterns from NIR excited pure helium droplets. Their clear directionality indicates fast explosion in polarization direction.[11] Reprinted with permission of American Physical Society, Copyright 2022.

One important aspect for time-resolved imaging of unique structures such as the rare-gas or metal clusters introduced above is the fact that the structure of the original particle is not known and it may be hard to compare events from different delays. A possible strategy is to use repetitive targets, for example by controlled splitting of liquid jets[111], or by using wet-chemically produced nanoparticles with a small distribution of shapes and sizes (see TEM image in Figure 5.23 a).

The temporal resolution of such experiments is limited by the pulse durations of optical and short wavelength laser pulses, as well as the temporal jitter between both. Several methods have been developed at FELs to measure the timing jitter for each pair of pulses and to re-sort individual events based on this information[78,48]. This way, the time resolution of laser-pump X-ray-probe experiments at FEL facilities could be lowered to tens of femtoseconds[191], which is fast enough to "film" the motion of ions or atoms after laser excitation, but not for studying electron dynamics. In this respect, HHG-based sources are still superior. They are comparatively compact, avoiding a large source of jitter, and infrared and shortwave pulses are inherently fixed to sub-femtosecond accuracy with respect to each other due to the generation process. An outlook on the upcoming

tion images of pump and probe pulses. Only few attempts have been made so far[69,190,94]. The approach may become more important, as promising pathways have opened up recently with two-color FEL pulses with accurately controlled delays[130,206,168] and CDI detectors that are capable of separating different photon energies[214,118,146]. Here, we will focus on scenarios using optical pump pulses for excitation of clusters and nanoparticles.

field of CDI of electron dynamics is given in Section 5.5.4.

5.5.1 Time-resolved imaging of an expanding nanoplasma

The dynamics of clusters[84,73], nanodroplets[11] and very regular nanoparticles[162] of tens to hundreds of nanometers diameter, excited with intense near infrared (NIR) pulses results, have been investigated with time-resolved CDI. On a time-scale of femtoseconds to picoseconds (depending on the laser intensity, the size of the nanostructures, and the respective atomic masses and thus inertia) the surface of the particles softens by the dominating hydrodynamic expansion. Consequently, the diffraction signal at large angles drops and disappears[bb]. This phenomenon is exemplified in Figure 5.23 a[162]. The analysis of slope and spacing of the diffraction fringes as a function of delay allows to retrieve detailed information on the nanoplasma expansion and direct comparison with modeling[162,11]. For very large, heavy systems, the slow hydrodynamic expansion takes long enough to let the inner part of the cluster nanoplasma recombine fully and disintegrate on a nanosecond time scale as a warm cloud of neutral gas[73]. In the other limit of very light atoms using pure helium nanodroplets, a strong directionality of the nanoplasma evolution along the laser polarization axis is observed[11] (see Figure 5.23b).

5.5.2 Doping induced ignition vs. undoped helium droplet explosion

The dynamics induced by an intense NIR laser pulse in a helium nanodroplet can be strongly altered by changing from a pristine droplet to a xenon-doped system[126,141,142]. The heavier atoms are much more easily ionized by the NIR field, and theoretical modeling indicates that already a few xenon atoms in a large helium droplet suffice to ignite a nanoplasma at much reduced laser intensities. From static CDI experiments of xenon-doped helium droplets (see Fig. 5.19 b,c) it is known that the distribution of xenon within a helium droplet is governed by the localization of quantum vortices which tend to capture the xenon atoms. Accordingly, after igniting a nanoplasma in helium droplets at more moderate NIR intensities as in Reference [11], the evolution results in distinctly different patterns with particular symmetries[123] (see Fig. 5.24).

5.5.3 Resolving ultrafast melting and boiling

Slowly heated matter undergoes the well-known phase transition from solid to liquid to gaseous. For very fast laser-heating, new phenomena such as cavitation of a superheated liquid occur. In a recent experiment[53,54], Coulomb-driven strong-field effects were avoided by homogeneously heating silver clusters *via* their Mie plasmon resonance[113,59] with a

[bb] An intuitive picture is the limiting case of a fully smoothed Gaussian distribution: the Fourier transform of a Gaussian is a Gaussian, so the diffraction pattern consists only of the central maximum.

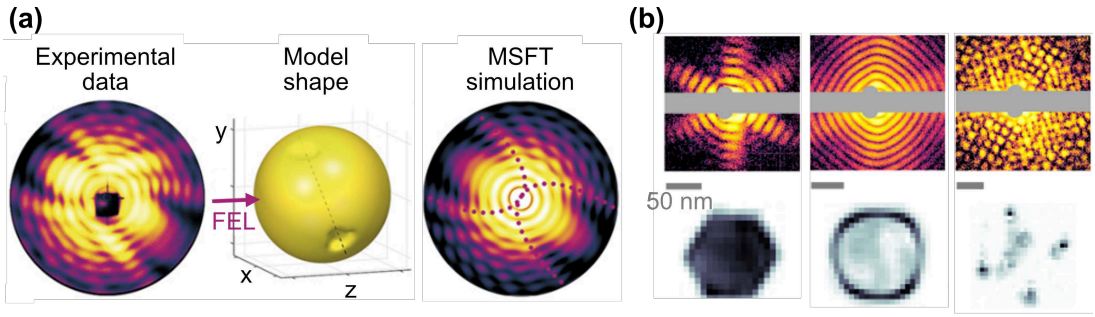

Figure 5.24: (a) Wide-angle diffraction pattern and matching simulation of a doping-ignited helium nanodroplet.[123] Figure reprinted with permission of corresponding author. (b) Hundreds of picoseconds after plasmonic excitation with a rather weak 400 nm laser, silver clusters show faceted shapes, a thin-walled bubble, or fragments.[54] Reprinted with permission from corresponding author.

rather weak 400 nm laser pulse[54] (see Figure 5.24b). At delays of hundreds of picoseconds after irradiation, still compact, faceted structures coexist with large, hollow "nanobubbles" and fragments of exploded bubbles. The results on free plasmon-heated silver nanoclusters mostly agree with previous work on NIR-heated, deposited metal nanoparticles[41,101], however, the influence of the deposition surface and possible Coulomb-driven effects in the latter experiments cannot be disentangled from the ultrafast melting process in these experiments, possibly leading to differing observations like off-center bubbles which rapture at much smaller bubble sizes[101].

5.5.4 Outlook: Towards attosecond CDI of electron dynamics

Until today, most CDI applications rely on the strong "diffraction before destruction" assumption[39], where the electronic density is considered constant throughout the duration of the X-ray pulse, and the destruction of the sample sets in only afterwards. Electron dynamics occurring during obtaining the diffraction patterns are usually neglected or seen as "ultrafast radiation damage". At the same time, it is clear that the process of CDI is intrinsically sensitive to electron dynamics[163]. Elastic light scattering takes place at the electrons bound to the nanoscale object, leading to a change in the scattering response for a strongly altered electron configuration. Experiments on single clusters have shown that ultrafast electronic changes can indeed become visible in an otherwise homogeneous nanoparticle[31,182]. With near-resonant CDI changes in the diffraction signal due to ionization could be made visible, and even some spatial information on the inhomogeneous distribution of high charge states in the nanoplasma could be extracted[182]. Utilizing the sensitivity of CDI on electronic structure as a tool is however only in its infancy because, until very recently, available FEL pulses had durations of several tens or hundreds of femtoseconds, too long to resolve electron dynamics.

Intense XUV pulse trains and even isolated attosecond pulses have been developed at HHG sources around the world within the last decade[140]. In a favourable combination of parameters, single-pulse single-particle HHG-CDI has been demonstrated[181] and first associated time-resolved experiments[245,204] using intense HHG-based XUV sources[196,205] provide a promising outlook of using HHG-based CDI in the study of electron dynamics.

Within the last few years, also the FEL community has seen a leap into the attosecond regime[55,136,17,152], driving the emergence of ideas on how to deal with broadband or polychromatic attosecond coherent diffraction images[1,236,187,133,100]. Moreover, theoretical predictions for signatures of ultrafast electron dynamics in the CDI signal[52,163,165,164,114,166] show that the extraction of "dynamic scatterer information" will require the development of novel analysis approaches.

The very first work on experimental attoCDI of isolated rare-gas clusters from the group of Tais Gorkhover[117] indicates an enhancement of the scattering signal for the shortest pulse durations, which is assigned to transient resonances. This is very exciting as it may provide better means for single-molecule imaging. X-ray pulses with parameters as projected by simulating successful single-molecule imaging[151] are just now becoming available[55], and the run for the molecular movie is not over[58], surprises are to be awaited.

Bibliography

[1] Brian Abbey, Lachlan W Whitehead, Harry M Quiney, David J Vine, Guido A Cadenazzi, Clare A Henderson, Keith A Nugent, Eugeniu Balaur, Corey T Putkunz, Andrew G Peele, et al. Lensless imaging using broadband x-ray sources. *Nature Photonics*, 5(7):420–424, 2011.

[2] Rafael Abela, Arturo Alarcon, Jürgen Alex, Christopher Arrell, Vladimir Arsov, Simona Bettoni, Markus Bopp, Christoph Bostedt, H-H Braun, Marco Calvi, et al. The swissfel soft x-ray free-electron laser beamline: Athos. *Journal of synchrotron radiation*, 26(4):1073–1084, 2019.

[3] Edward Ackad, Nicolas Bigaouette, and Lora Ramunno. Augmented collisional ionization via excited states in xuv cluster interactions. *Journal of Physics B: Atomic, Molecular and Optical Physics*, 44(16):165102, 2011.

[4] Edward Ackad, Nicolas Bigaouette, Stephanie Mack, Konstatin Popov, and Lora Ramunno. Recombination effects in soft-x-ray cluster interactions at the xenon giant resonance. *New Journal of Physics*, 15(5):053047, 2013.

[5] E Allaria, Roberto Appio, L Badano, WA Barletta, S Bassanese, SG Biedron, A Borga, E Busetto, D Castronovo, P Cinquegrana, et al. Highly coherent and stable pulses from the fermi seeded free-electron laser in the extreme ultraviolet. *Nature Photonics*, 6(10):699–704, 2012.

[6] Jakob Andreasson, Andrew V Martin, Meng Liang, Nicusor Timneanu, Andrew Aquila, Fenglin Wang, Bianca Iwan, Martin Svenda, Tomas Ekeberg, Max Hantke, et al. Automated identification and classification of single particle serial femtosecond x-ray diffraction data. *Optics express*, 22(3):2497–2510, 2014.

[7] A Aquila, A Barty, C Bostedt, S Boutet, G Carini, D DePonte, P Drell, S Doniach, KH Downing, T Earnest, et al. The linac coherent light source single particle imaging road map. *Structural Dynamics*, 2(4):041701, 2015.

[8] Mathias Arbeiter and Thomas Fennel. Ionization heating in rare-gas clusters under intense xuv laser pulses. *Physical Review A*, 82(1):013201, 2010.

[9] Mathias Arbeiter and Thomas Fennel. Rare-gas clusters in intense vuv, xuv and soft x-ray pulses: signatures of the transition from nanoplasma-driven cluster expansion

to coulomb explosion in ion and electron spectra. *New Journal of Physics*, 13(5): 053022, 2011.

[10] Kartik Ayyer, P Lourdu Xavier, Johan Bielecki, Zhou Shen, Benedikt J Daurer, Amit K Samanta, Salah Awel, Richard Bean, Anton Barty, Martin Bergemann, et al. 3d diffractive imaging of nanoparticle ensembles using an x-ray laser. *Optica*, 8(1):15–23, 2021.

[11] Camila Bacellar, Adam S Chatterley, Florian Lackner, CD Pemmaraju, Rico Mayro P Tanyag, Deepak Verma, Charles Bernando, Sean MO O'Connell, Maximilian Bucher, Ken R Ferguson, et al. Anisotropic surface broadening and core depletion during the evolution of a strong-field induced nanoplasma. *Physical Review Letters*, 129(7):073201, 2022.

[12] Ingo Barke, Hannes Hartmann, Daniela Rupp, Leonie Flückiger, Mario Sauppe, Marcus Adolph, Sebastian Schorb, Christoph Bostedt, Rolf Treusch, Christian Peltz, et al. The 3d-architecture of individual free silver nanoparticles captured by x-ray scattering. *Nature communications*, 6(1):1–7, 2015.

[13] Heinz H Bauschke, Patrick L Combettes, and D Russell Luke. Hybrid projection–reflection method for phase retrieval. *JOSA A*, 20(6):1025–1034, 2003.

[14] August Beer. Bestimmung der absorption des rothen lichts in farbigen flüssigkeiten. *Ann. Physik*, 162:78–88, 1852.

[15] Andrei Benediktovitch, Laurent Mercadier, Olivier Peyrusse, Andreas Przystawik, Tim Laarmann, Bruno Langbehn, Cédric Bomme, Benjamin Erk, Jonathan Correa, Caroline Mossé, et al. Amplified spontaneous emission in the extreme ultraviolet by expanding xenon clusters. *Physical Review A*, 101(6):063412, 2020.

[16] Charles Bernando, Rico Mayro P Tanyag, Curtis Jones, Camila Bacellar, Maximilian Bucher, Ken R Ferguson, Daniela Rupp, Michael P Ziemkiewicz, Luis F Gomez, Adam S Chatterley, et al. Shapes of rotating superfluid helium nanodroplets. *Physical Review B*, 95(6):064510, 2017.

[17] Martin Beye, Markus Gühr, Ingmar Hartl, Elke Plönjes, Lucas Schaper, Siegfried Schreiber, Kai Tiedtke, and Rolf Treusch. Flash and the flash2020+ project—current status and upgrades for the free-electron laser in hamburg at desy. *The European Physical Journal Plus*, 138(3):193, 2023.

[18] Johan Bielecki, Max F Hantke, Benedikt J Daurer, Hemanth KN Reddy, Dirk Hasse, Daniel SD Larsson, Laura H Gunn, Martin Svenda, Anna Munke, Jonas A Sellberg, et al. Electrospray sample injection for single-particle imaging with x-ray lasers. *Science advances*, 5(5):eaav8801, 2019.

[19] SA Bobkov, AB Teslyuk, RP Kurta, O Yu Gorobtsov, OM Yefanov, VA Ilyin, RA Senin, and IA Vartanyants. Sorting algorithms for single-particle imaging experiments at x-ray free-electron lasers. *Journal of synchrotron radiation*, 22(6): 1345–1352, 2015.

[20] Michael J Bogan, W Henry Benner, Sébastien Boutet, Urs Rohner, Matthias Frank, Anton Barty, M Marvin Seibert, Filipe Maia, Stefano Marchesini, Saša Bajt, et al. Single particle x-ray diffractive imaging. *Nano letters*, 8(1):310–316, 2008.

[21] Michael J Bogan, Sébastien Boutet, Henry N Chapman, Stefano Marchesini, Anton Barty, W Henry Benner, Urs Rohner, Matthias Frank, Stefan P Hau-Riege, Sasa Bajt, et al. Aerosol imaging with a soft x-ray free electron laser. *Aerosol Science and Technology*, 44(3):i–vi, 2010.

[22] Michael J Bogan, Dmitri Starodub, Christina Y Hampton, and Raymond G Sierra. Single-particle coherent diffractive imaging with a soft x-ray free electron laser: towards soot aerosol morphology. *Journal of Physics B: Atomic, Molecular and Optical Physics*, 43(19):194013, 2010.

[23] Craig F. Bohren and Donald R. Huffman. *Absorption and Scattering of Light by Small Particles*. Wiley, apr 1998. ISBN 9780471293408. doi: 10.1002/9783527618156. URL `https://onlinelibrary.wiley.com/doi/book/10.1002/9783527618156`.

[24] Craig F Bohren and Donald R Huffman. *Absorption and scattering of light by small particles*. John Wiley & Sons, 2008.

[25] Max Born. Quantenmechanik der stoßvorgänge. *Zeitschrift für Physik*, 38(11-12): 803–827, 1926.

[26] Ch Bostedt, H Thomas, M Hoener, E Eremina, T Fennel, K-H Meiwes-Broer, H Wabnitz, M Kuhlmann, E Plönjes, K Tiedtke, et al. Multistep ionization of argon clusters in intense femtosecond extreme ultraviolet pulses. *Physical review letters*, 100(13):133401, 2008.

[27] Ch Bostedt, JD Bozek, PH Bucksbaum, RN Coffee, JB Hastings, Z Huang, RW Lee, Sebastian Schorb, JN Corlett, P Denes, et al. Ultra-fast and ultra-intense x-ray sciences: first results from the linac coherent light source free-electron laser. *Journal of Physics B: Atomic, Molecular and Optical Physics*, 46(16):164003, 2013.

[28] Christoph Bostedt, Henry N Chapman, John T Costello, José R Crespo López-Urrutia, Stefan Düsterer, Sascha W Epp, Josef Feldhaus, Alexander Föhlisch, Michael Meyer, Thomas Möller, et al. Experiments at flash. *Nuclear Instruments and Methods in Physics Research Section A: Accelerators, Spectrometers, Detectors and Associated Equipment*, 601(1-2):108–122, 2009.

[29] Christoph Bostedt, Marcus Adolph, Ekaterina Eremina, Matthias Hoener, Daniela Rupp, Sebastian Schorb, Heiko Thomas, Antonio RB de Castro, and Thomas Möller. Clusters in intense flash pulses: ultrafast ionization dynamics and electron emission studied with spectroscopic and scattering techniques. *Journal of Physics B: Atomic, Molecular and Optical Physics*, 43(19):194011, 2010.

[30] Christoph Bostedt, Heiko Thomas, Matthias Hoener, Thomas Möller, Ulf Saalmann, Ionuţ Georgescu, Christian Gnodtke, and Jan-Michael Rost. Fast electrons from multi-electron dynamics in xenon clusters induced by inner-shell ionization. *New Journal of Physics*, 12(8):083004, 2010.

[31] Christoph Bostedt, Ekaterina Eremina, Daniela Rupp, Marcus Adolph, Heiko Thomas, Matthias Hoener, Antonio RB de Castro, Josef Tiggesbäumker, K-H Meiwes-Broer, Tim Laarmann, et al. Ultrafast x-ray scattering of xenon nanoparticles: imaging transient states of matter. *Physical Review Letters*, 108(9):093401, 2012.

[32] Christoph Bostedt, Sébastien Boutet, David M Fritz, Zhirong Huang, Hae Ja Lee, Henrik T Lemke, Aymeric Robert, William F Schlotter, Joshua J Turner, and Garth J Williams. Linac coherent light source: The first five years. *Reviews of Modern Physics*, 88(1):015007, 2016.

[33] Christoph Bostedt, Tais Gorkhover, Daniela Rupp, and Thomas Möller. Clusters and nanocrystals. *Synchrotron light sources and free-electron lasers: Accelerator physics, instrumentation and science applications*, pages 1525–1573, 2020.

[34] Christian Brönnimann and Peter Trüb. Hybrid pixel photon counting x-ray detectors for synchrotron radiation. *Synchrotron Light Sources and Free-Electron Lasers: Accelerator Physics, Instrumentation and Science Applications*, pages 1191–1223, 2020.

[35] Henry N Chapman. X-ray free-electron lasers for the structure and dynamics of macromolecules. *Annual review of biochemistry*, 88:35–58, 2019.

[36] Henry N Chapman, Anton Barty, Michael J Bogan, Sébastien Boutet, Matthias Frank, Stefan P Hau-Riege, Stefano Marchesini, Bruce W Woods, Saša Bajt, W Henry Benner, et al. Femtosecond diffractive imaging with a soft-x-ray free-electron laser. *Nature Physics*, 2(12):839–843, 2006.

[37] Henry N Chapman, Anton Barty, Stefano Marchesini, Aleksandr Noy, Stefan P Hau-Riege, Congwu Cui, Malcolm R Howells, Rachel Rosen, Haifeng He, John CH Spence, et al. High-resolution ab initio three-dimensional x-ray diffraction microscopy. *JOSA A*, 23(5):1179–1200, 2006.

[38] Henry N Chapman, Petra Fromme, Anton Barty, Thomas A White, Richard A Kirian, Andrew Aquila, Mark S Hunter, Joachim Schulz, Daniel P DePonte, Uwe Weierstall, et al. Femtosecond x-ray protein nanocrystallography. *Nature*, 470(7332): 73–77, 2011.

[39] Henry N Chapman, Carl Caleman, and Nicusor Timneanu. Diffraction before destruction. *Philosophical Transactions of the Royal Society B: Biological Sciences*, 369(1647):20130313, 2014.

[40] Chien-Chun Chen, Jianwei Miao, CW Wang, and TK Lee. Application of optimization technique to noncrystalline x-ray diffraction microscopy: Guided hybrid input-output method. *Physical Review B*, 76(6):064113, 2007.

[41] Jesse N Clark, Loren Beitra, Gang Xiong, David M Fritz, Henrik T Lemke, Diling Zhu, Matthieu Chollet, Garth J Williams, Marc M Messerschmidt, Brian Abbey, et al. Imaging transient melting of a nanocrystal using an x-ray laser. *Proceedings of the National Academy of Sciences*, 112(24):7444–7448, 2015.

[42] Alessandro Colombo, Davide Emilio Galli, Liberato De Caro, Francesco Scattarella, and Elvio Carlino. Facing the phase problem in coherent diffractive imaging via memetic algorithms. *Scientific reports*, 7(1):1–12, 2017.

[43] Alessandro Colombo, Julian Zimmermann, Bruno Langbehn, Thomas Möller, Christian Peltz, Katharina Sander, Björn Kruse, Paul Tümmler, Ingo Barke, Daniela Rupp, et al. The scatman: an approximate method for fast wide-angle scattering simulations. *Journal of Applied Crystallography*, 55(5), 2022.

[44] Alessandro Colombo, Simon Dold, Patrice Kolb, Nils Bernhardt, Patrick Behrens, Jonathan Correa, Stefan Düsterer, Benjamin Erk, Linos Hecht, Andrea Heilrath, et al. Three-dimensional femtosecond snapshots of isolated faceted nanostructures. *Science Advances*, 9(8):eade5839, 2023.

[45] James W Cooley and John W Tukey. An algorithm for the machine calculation of complex fourier series. *Mathematics of computation*, 19(90):297–301, 1965.

[46] François Coppens, Francesco Ancilotto, Manuel Barranco, Nadine Halberstadt, and Martí Pi. Capture of xe and ar atoms by quantized vortices in 4 he nanodroplets. *Physical Chemistry Chemical Physics*, 19(36):24805–24818, 2017.

[47] John M Cowley and A F_ Moodie. The scattering of electrons by atoms and crystals. i. a new theoretical approach. *Acta Crystallographica*, 10(10):609–619, 1957.

[48] Miltcho B Danailov, Filippo Bencivenga, Flavio Capotondi, Francesco Casolari, Paolo Cinquegrana, Alexander Demidovich, Erika Giangrisostomi, Maya P Kiskinova, Gabor Kurdi, Michele Manfredda, et al. Towards jitter-free pump-probe

measurements at seeded free electron laser facilities. *Optics express*, 22(11):12869–12879, 2014.

[49] Benedikt J Daurer, Max F Hantke, Carl Nettelblad, and Filipe RNC Maia. Hummingbird: monitoring and analyzing flash x-ray imaging experiments in real time. *Journal of applied crystallography*, 49(3):1042–1047, 2016.

[50] W Decking, S Abeghyan, P Abramian, A Abramsky, A Aguirre, C Albrecht, P Alou, M Altarelli, P Altmann, K Amyan, et al. A mhz-repetition-rate hard x-ray free-electron laser driven by a superconducting linear accelerator. *Nature photonics*, 14 (6):391–397, 2020.

[51] T Ditmire, JWG Tisch, E Springate, MB Mason, N Hay, RA Smith, J Marangos, and MHR Hutchinson. High-energy ions produced in explosions of superheated atomic clusters. *Nature*, 386(6620):54–56, 1997.

[52] Gopal Dixit, Jan Malte Slowik, and Robin Santra. Proposed imaging of the ultrafast electronic motion in samples using x-ray phase contrast. *Physical Review Letters*, 110(13):137403, 2013.

[53] Simon Dold. *Time-resolved imaging of laser-induced phase transitions in free silver nanoclusters*. PhD thesis, Universität Freiburg, 2020.

[54] Simon et al. Dold. Melting, inflation and explosion of superheated plasmonic nanoparticles. *on ArXiv XXXXXXXXXX*, 2023.

[55] Joseph Duris, Siqi Li, Taran Driver, Elio G Champenois, James P MacArthur, Alberto A Lutman, Zhen Zhang, Philipp Rosenberger, Jeff W Aldrich, Ryan Coffee, et al. Tunable isolated attosecond x-ray pulses with gigawatt peak power from a free-electron laser. *Nature Photonics*, 14(1):30–36, 2020.

[56] Tomas Ekeberg, Stefan Engblom, and Jing Liu. Machine learning for ultrafast x-ray diffraction patterns on large-scale gpu clusters. *The international journal of high performance computing applications*, 29(2):233–243, 2015.

[57] Tomas Ekeberg, Martin Svenda, Chantal Abergel, Filipe RNC Maia, Virginie Seltzer, Jean-Michel Claverie, Max Hantke, Olof Jönsson, Carl Nettelblad, Gijs Van Der Schot, et al. Three-dimensional reconstruction of the giant mimivirus particle with an x-ray free-electron laser. *Physical review letters*, 114(9):098102, 2015.

[58] Tomas Ekeberg, Dameli Assalauova, Johan Bielecki, Rebecca Boll, Benedikt J Daurer, Lutz A Eichacker, Linda E Franken, Davide E Galli, Luca Gelisio, Lars Gumprecht, et al. Observation of a single protein by ultrafast x-ray diffraction. *bioRxiv*, pages 2022–03, 2022.

[59] Mostafa A El-Sayed. Some interesting properties of metals confined in time and nanometer space of different shapes. *Accounts of chemical research*, 34(4):257–264, 2001.

[60] Veit Elser. Phase retrieval by iterated projections. *JOSA A*, 20(1):40–55, 2003.

[61] Paul Emma, R Akre, J Arthur, R Bionta, C Bostedt, J Bozek, A Brachmann, P Bucksbaum, Ryan Coffee, F-J Decker, et al. First lasing and operation of an ångstrom-wavelength free-electron laser. *nature photonics*, 4(9):641–647, 2010.

[62] Benjamin Erk, Jan P Müller, Cédric Bomme, Rebecca Boll, Günter Brenner, Henry N Chapman, Jonathan Correa, Stefan Düsterer, Siarhei Dziarzhytski, Stefan Eisebitt, et al. Camp@ flash: an end-station for imaging, electron-and ion-spectroscopy, and pump–probe experiments at the flash free-electron laser. *Journal of synchrotron radiation*, 25(5):1529–1540, 2018.

[63] Niloofar Esmaeildoost, Olof Jönsson, Trevor A McQueen, Marjorie Ladd-Parada, Hartawan Laksmono, Ne-Te Duane Loh, and Jonas A Sellberg. Heterogeneous ice growth in micron-sized water droplets due to spontaneous freezing. *Crystals*, 12(1): 65, 2022.

[64] Albert Fannjiang and Thomas Strohmer. The numerics of phase retrieval. *Acta Numerica*, 29:125–228, 2020.

[65] Alexandra J Feinberg, Deepak Verma, Sean MO O'Connell-Lopez, Swetha Erukala, Rico Mayro P Tanyag, Weiwu Pang, Catherine A Saladrigas, Benjamin W Toulson, Mario Borgwardt, Niranjan Shivaram, et al. Aggregation of solutes in bosonic versus fermionic quantum fluids. *Science advances*, 7(50):eabk2247, 2021.

[66] Alexandra J Feinberg, Felix Laimer, Rico Mayro P Tanyag, Björn Senfftleben, Yevheniy Ovcharenko, Simon Dold, Michael Gatchell, Sean MO O'Connell-Lopez, Swetha Erukala, Catherine A Saladrigas, et al. X-ray diffractive imaging of highly ionized helium nanodroplets. *Physical Review Research*, 4(2):L022063, 2022.

[67] Th Fennel, K-H Meiwes-Broer, J Tiggesbäumker, P-G Reinhard, Phuong Mai Dinh, and Eric Suraud. Laser-driven nonlinear cluster dynamics. *Reviews of modern physics*, 82(2):1793, 2010.

[68] Thomas Fennel, Lora Ramunno, and Thomas Brabec. Highly charged ions from laser-cluster interactions: local-field-enhanced impact ionization and frustrated electron-ion recombination. *Physical review letters*, 99(23):233401, 2007.

[69] Ken R Ferguson, Maximilian Bucher, Tais Gorkhover, Sébastien Boutet, Hironobu Fukuzawa, Jason E Koglin, Yoshiaki Kumagai, Alberto Lutman, Agostino Marinelli,

Marc Messerschmidt, et al. Transient lattice contraction in the solid-to-plasma transition. *Science advances*, 2(1):e1500837, 2016.

[70] C Fienup and J Dainty. Phase retrieval and image reconstruction for astronomy. *Image recovery: theory and application*, 231:275, 1987.

[71] James R Fienup. Reconstruction of an object from the modulus of its fourier transform. *Optics letters*, 3(1):27–29, 1978.

[72] James R Fienup. Phase retrieval algorithms: a comparison. *Applied optics*, 21(15): 2758–2769, 1982.

[73] Leonie Flückiger, Daniela Rupp, Marcus Adolph, Tais Gorkhover, Maria Krikunova, Maria Müller, Tim Oelze, Yevheniy Ovcharenko, Mario Sauppe, Sebastian Schorb, et al. Time-resolved x-ray imaging of a laser-induced nanoplasma and its neutral residuals. *New Journal of Physics*, 18(4):043017, 2016.

[74] Petra Fromme, William S Graves, and Jose M Martin-Garcia. Serial femtosecond crystallography: A decade at the forefront in structural biology. *eLS*, pages 1–17, 2020.

[75] H Fukuzawa, X-J Liu, G Prümper, M Okunishi, K Shimada, K Ueda, T Harada, M Toyoda, M Yanagihara, M Yamamoto, et al. Dead-time-free ion momentum spectroscopy of multiple ionization of xe clusters irradiated by euv free-electron laser pulses. *Physical Review A*, 79(3):031201, 2009.

[76] H Fukuzawa, S-K Son, K Motomura, S Mondal, K Nagaya, S Wada, X-J Liu, Raimund Feifel, T Tachibana, Y Ito, et al. Deep inner-shell multiphoton ionization by intense x-ray free-electron laser pulses. *Physical review letters*, 110(17):173005, 2013.

[77] Hironobu Fukuzawa and Kiyoshi Ueda. X-ray induced ultrafast dynamics in atoms, molecules, and clusters: experimental studies at an x-ray free-electron laser facility sacla and modelling. *Advances in Physics: X*, 5(1):1785327, 2020.

[78] Cornelius Gahl, Armin Azima, Martin Beye, Martin Deppe, Kristian Döbrich, Urs Hasslinger, Franz Hennies, Alexej Melnikov, Mitsuru Nagasono, Annette Pietzsch, et al. A femtosecond x-ray/optical cross-correlator. *Nature Photonics*, 2(3):165–169, 2008.

[79] N Gerken, S Klumpp, AA Sorokin, K Tiedtke, M Richter, V Bürk, K Mertens, P Juranić, and M Martins. Time-dependent multiphoton ionization of xenon in the soft-x-ray regime. *Physical Review Letters*, 112(21):213002, 2014.

[80] Oliver Gessner and Andrey F Vilesov. Imaging quantum vortices in superfluid helium droplets. *Annual review of physical chemistry*, 70:173–198, 2019.

[81] Luis F Gomez, Ken R Ferguson, James P Cryan, Camila Bacellar, Rico Mayro P Tanyag, Curtis Jones, Sebastian Schorb, Denis Anielski, Ali Belkacem, Charles Bernando, et al. Shapes and vorticities of superfluid helium nanodroplets. *Science*, 345(6199):906–909, 2014.

[82] Joseph W Goodman. *Introduction to Fourier optics*. Roberts and Company publishers, 2005.

[83] Tais Gorkhover, Marcus Adolph, Daniela Rupp, Sebastian Schorb, Sascha W Epp, Benjamin Erk, Lutz Foucar, Robert Hartmann, Nils Kimmel, K-U Kühnel, et al. Nanoplasma dynamics of single large xenon clusters irradiated with superintense x-ray pulses from the linac coherent light source free-electron laser. *Physical review letters*, 108(24):245005, 2012.

[84] Tais Gorkhover, Sebastian Schorb, Ryan Coffee, Marcus Adolph, Lutz Foucar, Daniela Rupp, Andrew Aquila, John D Bozek, Sascha W Epp, Benjamin Erk, et al. Femtosecond and nanometre visualization of structural dynamics in superheated nanoparticles. *Nature photonics*, 10(2):93–97, 2016.

[85] Tais Gorkhover, Anatoli Ulmer, Ken Ferguson, Max Bucher, Filipe RNC Maia, Johan Bielecki, Tomas Ekeberg, Max F Hantke, Benedikt J Daurer, Carl Nettelblad, et al. Femtosecond x-ray fourier holography imaging of free-flying nanoparticles. *Nature Photonics*, 12(3):150–153, 2018.

[86] Philipp Grohs, Sarah Koppensteiner, and Martin Rathmair. Phase retrieval: uniqueness and stability. *SIAM Review*, 62(2):301–350, 2020.

[87] H Haberland, M Karrais, and M Mall. A new type of cluster and cluster ion source. *Zeitschrift für Physik D Atoms, Molecules and Clusters*, 20(1):413–415, 1991.

[88] Otto F Hagena. Cluster ion sources. *Review of scientific instruments*, 63(4):2374–2379, 1992.

[89] Max F Hantke, Dirk Hasse, Filipe RNC Maia, Tomas Ekeberg, Katja John, Martin Svenda, N Duane Loh, Andrew V Martin, Nicusor Timneanu, Daniel SD Larsson, et al. High-throughput imaging of heterogeneous cell organelles with an x-ray laser. *Nature Photonics*, 8(12):943–949, 2014.

[90] Max F Hantke, Tomas Ekeberg, and Filipe RNC Maia. Condor: a simulation tool for flash x-ray imaging. *Journal of Applied Crystallography*, 49(4):1356–1362, 2016.

[91] Ross Harder. Deep neural networks in real-time coherent diffraction imaging. *IUCrJ*, 8(Pt 1):1, 2021.

[92] Stefan P Hau-Riege. *High-Intensity X-rays-Interaction with Matter: Processes in Plasmas, Clusters, Molecules and Solids*. John Wiley & Sons, 2012.

[93] Stefan P Hau-Riege, Richard A London, and Abraham Szoke. Dynamics of biological molecules irradiated by short x-ray pulses. *Physical Review E*, 69(5):051906, 2004.

[94] L. Hecht, J. Asmussen, B. Bastian, T. Baumann, L. Ltaief, C. Callegari, A. Colombo, S. De, A. DeFanis, M. di Fraia, S. Dold, T. Fennel, R. Hartmann, K. Kolatzki, S. Krishnan, B. Kruse, A. Lægdsmand, A. Laforge, B. Langbehn, S. Mandal, C. Medina, M. Meyer, T. Möller, R. Moshammer, Y. Ovcharenko, C. Peltz, T. Pfeiffer, P. Piseri, O. Plekan, K. Prince, M. Sauppe, M.L. Schubert, B. Senfftleben, K. Sishodia, F. Stienkemeier, R. Tanyag, P. Tümmler, A. Ulmer, S. Usenko, M. Mudrich, and D. Rupp. Two color diffractive imaging of helium nanodroplet dynamics. URL `https://physics.usc.edu/deamn22/Images/DEAMN22_program.pdf`.

[95] Burton L Henke, Eric M Gullikson, and John C Davis. X-ray interactions: photoabsorption, scattering, transmission, and reflection at e= 50-30,000 ev, z= 1-92. *Atomic data and nuclear data tables*, 54(2):181–342, 1993.

[96] V Hinger, A al Haddad, R Barten, A Bergamaschi, M Brückner, M Carulla, S Chiriotti-Alvarez, R Dinapoli, S Ebner, E Fröjdh, et al. Advancing the jungfrau detector toward low-energy x-ray applications. *Journal of Instrumentation*, 17(09): C09027, 2022.

[97] Phay J Ho, Benedikt J Daurer, Max F Hantke, Johan Bielecki, Andre Al Haddad, Maximilian Bucher, Gilles Doumy, Ken R Ferguson, Leonie Flückiger, Tais Gorkhover, et al. The role of transient resonances for ultra-fast imaging of single sucrose nanoclusters. *Nature communications*, 11(1):167, 2020.

[98] M Hoener, C Bostedt, H Thomas, L Landt, E Eremina, H Wabnitz, T Laarmann, R Treusch, ARB De Castro, and T Möller. Charge recombination in soft x-ray laser produced nanoplasmas. *Journal of Physics B: Atomic, Molecular and Optical Physics*, 41(18):181001, 2008.

[99] Malcolm R Howells, Tobias Beetz, Henry N Chapman, C Cui, JM Holton, CJ Jacobsen, J Kirz, Enju Lima, Stefano Marchesini, Huijie Miao, et al. An assessment of the resolution limitation due to radiation-damage in x-ray diffraction microscopy. *Journal of electron spectroscopy and related phenomena*, 170(1-3):4–12, 2009.

[100] Julius Huijts, Sara Fernandez, David Gauthier, Maria Kholodtsova, Ahmed Maghraoui, Kadda Medjoubi, Andrea Somogyi, Willem Boutu, and Hamed Merdji. Broadband coherent diffractive imaging. *Nature Photonics*, 14(10):618–622, 2020.

[101] Yungok Ihm, Do Hyung Cho, Daeho Sung, Daewoong Nam, Chulho Jung, Takahiro Sato, Sangsoo Kim, Jaehyun Park, Sunam Kim, Marcus Gallagher-Jones, et al. Direct observation of picosecond melting and disintegration of metallic nanoparticles. *Nature Communications*, 10(1):2411, 2019.

[102] Tetsuya Ishikawa, Hideki Aoyagi, Takao Asaka, Yoshihiro Asano, Noriyoshi Azumi, Teruhiko Bizen, Hiroyasu Ego, Kenji Fukami, Toru Fukui, Yukito Furukawa, et al. A compact x-ray free-electron laser emitting in the sub-ångström region. *nature photonics*, 6(8):540–544, 2012.

[103] Md Ranaul Islam, Ulf Saalmann, and Jan M Rost. Kinetic energy of ions after coulomb explosion of clusters induced by an intense laser pulse. *Physical Review A*, 73(4):041201, 2006.

[104] Eberhard J Jaeschke, Shaukat Khan, Jochen R Schneider, and Jerome B Hastings. *Synchrotron light sources and free-electron lasers: accelerator physics, instrumentation and science applications*. Springer, 2016.

[105] Curtis F Jones, Charles Bernando, Rico Mayro P Tanyag, Camila Bacellar, Ken R Ferguson, Luis F Gomez, Denis Anielski, Ali Belkacem, Rebecca Boll, John Bozek, et al. Coupled motion of xe clusters and quantum vortices in he nanodroplets. *Physical Review B*, 93(18):180510, 2016.

[106] Sergei Igorevich Kabanikhin. Definitions and examples of inverse and ill-posed problems. *Journal of Inverse and Ill-posed Problems*, 17:317–357, 2008.

[107] Heung-Sik Kang, Chang-Ki Min, Hoon Heo, Changbum Kim, Haeryong Yang, Gyujin Kim, Inhyuk Nam, Soung Youl Baek, Hyo-Jin Choi, Geonyeong Mun, et al. Hard x-ray free-electron laser with femtosecond-scale timing jitter. *Nature Photonics*, 11 (11):708–713, 2017.

[108] EP Kanter, Bertold Kraessig, Yongjin Li, AM March, P Ho, Nina Rohringer, Robin Santra, SH Southworth, LF DiMauro, G Doumy, et al. Unveiling and driving hidden resonances with high-fluence, high-intensity x-ray pulses. *Physical review letters*, 107 (23):233001, 2011.

[109] Richard A Kirian and Henry N Chapman. Imaging of objects by coherent diffraction of x-ray free-electron laser pulses. *Synchrotron light sources and free-electron lasers: Accelerator physics, instrumentation and science applications*, pages 1337–1397, 2020.

[110] K Koga and K-i Sugawara. Population statistics of gold nanoparticle morphologies: direct determination by hrem observations. *Surface science*, 529(1-2):23–35, 2003.

[111] Katharina Kolatzki, Marie Louise Schubert, Anatoli Ulmer, Thomas Möller, Daniela Rupp, and Rico Mayro P Tanyag. Micrometer-sized droplets from liquid helium jets at low stagnation pressures. *Physics of Fluids*, 34(1):012002, 2022.

[112] Vladimir P Krainov and Michail B Smirnov. Cluster beams in the super-intense femtosecond laser pulse. *Physics reports*, 370(3):237–331, 2002.

[113] U Kreibig and LJSS Genzel. Optical absorption of small metallic particles. *Surface Science*, 156:678–700, 1985.

[114] Björn Kruse, Benjamin Liewehr, Christian Peltz, and Thomas Fennel. Quantum coherent diffractive imaging. *Journal of Physics: Photonics*, 2(2):024007, 2020.

[115] Yoshiaki Kumagai, Zoltan Jurek, Weiqing Xu, Hironobu Fukuzawa, Koji Motomura, Denys Iablonskyi, Kiyonobu Nagaya, Shin-ichi Wada, Subhendu Mondal, Tetsuya Tachibana, et al. Radiation-induced chemical dynamics in ar clusters exposed to strong x-ray pulses. *Physical review letters*, 120(22):223201, 2018.

[116] Yoshiaki Kumagai, Zoltan Jurek, Weiqing Xu, Hironobu Fukuzawa, Koji Motomura, Denys Iablonskyi, Kiyonobu Nagaya, Shin-ichi Wada, Subhendu Mondal, Tetsuya Tachibana, et al. Real-time observation of disintegration processes within argon clusters ionized by a hard-x-ray pulse of moderate fluence. *Physical Review A*, 101 (2):023412, 2020.

[117] Stephan Kuschel, Phay J Ho, Andre Al Haddad, Felix Zimmermann, Leonie Flueckiger, Matthew R Ware, Joseph Duris, James P MacArthur, Alberto Lutman, Ming-Fu Lin, et al. Enhanced ultrafast x-ray diffraction by transient resonances. *arXiv preprint arXiv:2207.05472*, 2022.

[118] Markus Kuster, Karim Ahmed, K-E Ballak, Cyril Danilevski, Marko Ekmedžić, Bruno Fernandes, Patrick Gessler, Robert Hartmann, Steffen Hauf, Peter Holl, et al. The 1-megapixel pnccd detector for the small quantum systems instrument at the european xfel: system and operation aspects. *Journal of Synchrotron Radiation*, 28 (2):576–587, 2021.

[119] T Laarmann, ARB De Castro, P Gürtler, W Laasch, J Schulz, H Wabnitz, and T Möller. Interaction of argon clusters with intense vuv-laser radiation: the role of electronic structure in the energy-deposition process. *Physical review letters*, 92 (14):143401, 2004.

[120] T Laarmann, Marian Rusek, H Wabnitz, Joachim Schulz, ARB De Castro, P Gürtler, W Laasch, and T Möller. Emission of thermally activated electrons from rare gas clusters irradiated with intense vuv light pulses from a free electron laser. *Physical review letters*, 95(6):063402, 2005.

[121] AC LaForge, Marcel Drabbels, Nils Benedict Brauer, Marcello Coreno, M Devetta, Michele Di Fraia, P Finetti, C Grazioli, R Katzy, V Lyamayev, et al. Collective autoionization in multiply-excited systems: a novel ionization process observed in helium nanodroplets. *Scientific reports*, 4(1):3621, 2014.

[122] Bruno Langbehn, Katharina Sander, Yevheniy Ovcharenko, Christian Peltz, Andrew Clark, Marcello Coreno, Riccardo Cucini, Marcel Drabbels, Paola Finetti, Michele Di Fraia, et al. Three-dimensional shapes of spinning helium nanodroplets. *Physical review letters*, 121(25):255301, 2018.

[123] Bruno Langbehn, Yevheniy Ovcharenko, Andrew Clark, Marcello Coreno, Riccardo Cucini, Alexander Demidovich, Marcel Drabbels, Paola Finetti, Michele Di Fraia, Luca Giannessi, et al. Diffraction imaging of light induced dynamics in xenon-doped helium nanodroplets. *New Journal of Physics*, 24(11):113043, 2022.

[124] Isidore Last and Joshua Jortner. Dynamics of the coulomb explosion of large clusters in a strong laser field. *Physical Review A*, 62(1):013201, 2000.

[125] Isidore Last, Andreas Heidenreich, and Joshua Jortner. Structure and energetics of microscopically inhomogeneous nanoplasmas in exploding clusters. *Zeitschrift für Physikalische Chemie*, 235(7):815–847, 2021.

[126] TV Liseykina and D Bauer. Plasma-formation dynamics in intense laser-droplet interaction. *Physical Review Letters*, 110(14):145003, 2013.

[127] ND Loh, Christina Y Hampton, Andrew V Martin, Dmitri Starodub, Raymond G Sierra, Anton Barty, Andrew Aquila, Joachim Schulz, Lukas Lomb, Jan Steinbrener, et al. Fractal morphology, imaging and mass spectrometry of single aerosol particles in flight. *Nature*, 486(7404):513–517, 2012.

[128] Ne-Te Duane Loh and Veit Elser. Reconstruction algorithm for single-particle diffraction imaging experiments. *Physical Review E*, 80(2):026705, 2009.

[129] D Russell Luke. Relaxed averaged alternating reflections for diffraction imaging. *Inverse problems*, 21(1):37, 2004.

[130] AA Lutman, R Coffee, Y Ding, Z Huang, J Krzywinski, T Maxwell, M Messerschmidt, and H-D Nuhn. Experimental demonstration of femtosecond two-color x-ray free-electron lasers. *Physical review letters*, 110(13):134801, 2013.

[131] Viktor Lyamayev, Yevheniy Ovcharenko, Raphael Katzy, Michele Devetta, Lukas Bruder, Aaron LaForge, Marcel Mudrich, Ulrich Person, Frank Stienkemeier, Maria Krikunova, et al. A modular end-station for atomic, molecular, and cluster science at the low density matter beamline of fermi@ elettra. *Journal of Physics B: Atomic, Molecular and Optical Physics*, 46(16):164007, 2013.

[132] Zhenhui Ma, Jeotikanta Mohapatra, Kecheng Wei, J Ping Liu, and Shouheng Sun. Magnetic nanoparticles: Synthesis, anisotropy, and applications. *Chemical Reviews*, 2021.

[133] Erik Malm, Hampus Wikmark, Bastian Pfau, Pablo Villanueva-Perez, Piotr Rudawski, Jasper Peschel, Sylvain Maclot, Michael Schneider, Stefan Eisebitt, Anders Mikkelsen, et al. Singleshot polychromatic coherent diffractive imaging with a high-order harmonic source. *Optics Express*, 28(1):394–404, 2020.

[134] Stefano Marchesini. Invited article: A unified evaluation of iterative projection algorithms for phase retrieval. *Review of scientific instruments*, 78(1):011301, 2007.

[135] Stefano Marchesini, H He, Henry N Chapman, Stefan P Hau-Riege, Aleksandr Noy, Malcolm R Howells, Uwe Weierstall, and John CH Spence. X-ray image reconstruction from a diffraction pattern alone. *Physical Review B*, 68(14):140101, 2003.

[136] Praveen Kumar Maroju, Cesare Grazioli, Michele Di Fraia, Matteo Moioli, Dominik Ertel, Hamed Ahmadi, Oksana Plekan, Paola Finetti, Enrico Allaria, Luca Giannessi, et al. Complex attosecond waveform synthesis at fel fermi. *Applied Sciences*, 11(21):9791, 2021.

[137] Tommaso Mazza, M Ilchen, MD Kiselev, EV Gryzlova, TM Baumann, R Boll, A De Fanis, P Grychtol, J Montaño, V Music, et al. Mapping resonance structures in transient core-ionized atoms. *Physical Review X*, 10(4):041056, 2020.

[138] Jianwei Miao, David Sayre, and HN Chapman. Phase retrieval from the magnitude of the fourier transforms of nonperiodic objects. *JOSA A*, 15(6):1662–1669, 1998.

[139] Jianwei Miao, J Kirz, and D Sayre. The oversampling phasing method. *Acta Crystallographica Section D: Biological Crystallography*, 56(10):1312–1315, 2000.

[140] Katsumi Midorikawa. Progress on table-top isolated attosecond light sources. *Nature Photonics*, 16(4):267–278, 2022.

[141] Alexey Mikaberidze, Ulf Saalmann, and Jan M Rost. Energy absorption of xenon clusters in helium nanodroplets under strong laser pulses. *Physical Review A*, 77 (4):041201, 2008.

[142] Alexey Mikaberidze, Ulf Saalmann, and Jan M Rost. Laser-driven nanoplasmas in doped helium droplets: Local ignition and anisotropic growth. *Physical review letters*, 102(12):128102, 2009.

[143] RP Millane and WH Hsiao. The basis of phase dominance. *Optics letters*, 34(17): 2607–2609, 2009.

[144] Christopher J Milne, Thomas Schietinger, Masamitsu Aiba, Arturo Alarcon, Jürgen Alex, Alexander Anghel, Vladimir Arsov, Carl Beard, Paul Beaud, Simona Bettoni, et al. Swissfel: the swiss x-ray free electron laser. *Applied Sciences*, 7(7):720, 2017.

[145] Patrick Mora and R Pellat. Self-similar expansion of a plasma into a vacuum. *The Physics of Fluids*, 22(12):2300–2304, 1979.

[146] A. Mozzanica, M. Andrä, R. Barten, A. Bergamaschi, S. Chiriotti, M. Brückner, R. Dinapoli, E. Fröjdh, D. Greiffenberg, F. Leonarski, C. Lopez-Cuenca, D. Mezza, S. Redford, C. Ruder, B. Schmitt, X. Shi, D. Thattil, G. Tinti, S. Vetter, and J. Zhang. The jungfrau detector for applications at synchrotron light sources and xfels. *Synchrotron Radiation News*, 31(6):16–20, 2018. doi: 10.1080/08940886.2018.1528429. URL `https://doi.org/10.1080/08940886.2018.1528429`.

[147] Maria Müller, L Schroedter, Tim Oelze, Lena Nösel, Andreas Przystawik, A Kickermann, Marcus Adolph, Tais Gorkhover, Leonie Flückiger, Maria Krikunova, et al. Ionization dynamics of xuv excited clusters: the role of inelastic electron collisions. *Journal of Physics B: Atomic, Molecular and Optical Physics*, 48(17):174002, 2015.

[148] BF Murphy, T Osipov, Z Jurek, L Fang, S-K Son, M Mucke, JHD Eland, V Zhaunerchyk, Raimund Feifel, L Avaldi, et al. Femtosecond x-ray-induced explosion of c60 at extreme intensity. *Nature communications*, 5(1):4281, 2014.

[149] Karol Nass. Radiation damage in protein crystallography at x-ray free-electron lasers. *Acta Crystallographica Section D: Structural Biology*, 75(2):211–218, 2019.

[150] Johanna Nelson, Xiaojing Huang, Jan Steinbrener, David Shapiro, Janos Kirz, Stefano Marchesini, Aaron M Neiman, Joshua J Turner, and Chris Jacobsen. High-resolution x-ray diffraction microscopy of specifically labeled yeast cells. *Proceedings of the National Academy of Sciences*, 107(16):7235–7239, 2010.

[151] R. Neutze *et al.* Potential for biomolecular imaging with femtosecond X-ray pulses. *Nature*, 406(6797):752–7, 2000.

[152] Frithjof Nolting, Christoph Bostedt, Thomas Schietinger, and Hans Braun. The swiss light source and swissfel at the paul scherrer institute. *The European Physical Journal Plus*, 138(2):126, 2023.

[153] Keith A Nugent. Coherent methods in the x-ray sciences. *Advances in Physics*, 59 (1):1–99, 2010.

[154] Jose E Ortiz-Castillo, Roberto C Gallo-Villanueva, Marc J Madou, and Victor H Perez-Gonzalez. Anisotropic gold nanoparticles: A survey of recent synthetic methodologies. *Coordination Chemistry Reviews*, 425:213489, 2020.

[155] Gábor Oszlányi and András Sütő. The charge flipping algorithm. *Acta Crystallographica Section A: Foundations of Crystallography*, 64(1):123–134, 2008.

[156] Y Ovcharenko, V Lyamayev, R Katzy, M Devetta, A LaForge, P O'Keeffe, O Plekan, P Finetti, Michele Di Fraia, M Mudrich, et al. Novel collective autoionization process observed in electron spectra of he clusters. *Physical Review Letters*, 112(7):073401, 2014.

[157] Sean MO O'Connell, Rico Mayro P Tanyag, Deepak Verma, Charles Bernando, Weiwu Pang, Camila Bacellar, Catherine A Saladrigas, Johannes Mahl, Benjamin W Toulson, Yoshiaki Kumagai, et al. Angular momentum in rotating superfluid droplets. *Physical review letters*, 124(21):215301, 2020.

[158] David Paganin et al. *Coherent X-ray optics*. Number 6. Oxford University Press on Demand, 2006.

[159] Rishi Pandit, Valerie Becker, Jeremy Thurston, Kasey Barrington, Zachary Hartwick, Nicolas Bigaouette, Lora Ramunno, and Edward Ackad. Effects of tampering on rare-gas core-shell clusters irradiated by resonantly tuned soft-x-ray pulses. *Physical Review A*, 107(4):043107, 2023.

[160] Hyung Joo Park, N Duane Loh, Raymond G Sierra, Christina Y Hampton, Dmitri Starodub, Andrew V Martin, Anton Barty, Andrew Aquila, Joachim Schulz, Jan Steinbrener, et al. Toward unsupervised single-shot diffractive imaging of heterogeneous particles using x-ray free-electron lasers. *Optics express*, 21(23):28729–28742, 2013.

[161] Christian Peltz, Charles Varin, Thomas Brabec, and Thomas Fennel. Time-resolved x-ray imaging of anisotropic nanoplasma expansion. *Physical Review Letters*, 113 (13):133401, 2014.

[162] Christian Peltz, Jeffrey A Powell, Philipp Rupp, Adam Summers, Taisia Gorkhover, Markus Gallei, Ina Halfpap, Egill Antonsson, Burkhard Langer, Carlos Trallero-Herrero, et al. Few-femtosecond resolved imaging of laser-driven nanoplasma expansion. *New Journal of Physics*, 24(4):043024, 2022.

[163] Daria Popova-Gorelova. Imaging electron dynamics with ultrashort light pulses: a theory perspective. *Applied Sciences*, 8(3):318, 2018.

[164] Daria Popova-Gorelova and Robin Santra. Atomic-scale imaging of laser-driven electron dynamics in solids using subcycle-resolved x-ray-optical wave mixing. *arXiv preprint arXiv:2012.10334*, 2020.

[165] Daria Popova-Gorelova, David A Reis, and Robin Santra. Theory of x-ray scattering from laser-driven electronic systems. *Physical Review B*, 98(22):224302, 2018.

[166] Daria Popova-Gorelova, Vladislav Guskov, and Robin Santra. Microscopic electron dynamics in nonlinear optical response of solids. *arXiv preprint arXiv:2009.07527*, 2020.

[167] I Poudyal, M Schmidt, and P Schwander. Single-particle imaging by x-ray free-electron lasers—how many snapshots are needed? *Structural Dynamics*, 7(2): 024102, 2020.

[168] Eduard Prat, Philipp Dijkstal, Eugenio Ferrari, Romain Ganter, Pavle Juranić, Alexander Malyzhenkov, Sven Reiche, Thomas Schietinger, Guanglei Wang, Andre Al Haddad, et al. Widely tunable two-color x-ray free-electron laser pulses. *Physical Review Research*, 4(2):L022025, 2022.

[169] Oleksandra Pryshchepa, Paweł Pomastowski, and Bogusław Buszewski. Silver nanoparticles: Synthesis, investigation techniques, and properties. *Advances in Colloid and Interface Science*, 284:102246, 2020.

[170] Edward M Purcell and Carlton R Pennypacker. Scattering and absorption of light by nonspherical dielectric grains. *The Astrophysical Journal*, 186:705–714, 1973.

[171] Kevin S Raines, Sara Salha, Richard L Sandberg, Huaidong Jiang, Jose A Rodríguez, Benjamin P Fahimian, Henry C Kapteyn, Jincheng Du, and Jianwei Miao. Three-dimensional structure determination from a single view. *Nature*, 463(7278): 214–217, 2010.

[172] D Reinhard, BD Hall, D Ugarte, and R Monot. Size-independent fcc-to-icosahedral structural transition in unsupported silver clusters: An electron diffraction study of clusters produced by inert-gas aggregation. *Physical Review B*, 55(12):7868, 1997.

[173] Paul-Gerhard Reinhard and Eric Suraud. *Introduction to cluster dynamics*. John Wiley & Sons, 2008.

[174] Aljoscha Rörig, Sang-Kil Son, Tommaso Mazza, Philipp Schmidt, Thomas M Baumann, Benjamin Erk, Markus Ilchen, Joakim Laksman, Valerija Music, Shashank Pathak, et al. Multiple-core-hole resonance spectroscopy with ultraintense x-ray pulses. *arXiv preprint arXiv:2303.07942*, 2023.

[175] Joseph Rosenblatt. Phase retrieval. *Communications in mathematical physics*, 95 (3):317–343, 1984.

[176] Jörg Rossbach, Jochen R Schneider, and Wilfried Wurth. 10 years of pioneering x-ray science at the free-electron laser flash at desy. *Physics reports*, 808:1–74, 2019.

[177] Benedikt Rudek, Sang-Kil Son, Lutz Foucar, Sascha W Epp, Benjamin Erk, Robert Hartmann, Marcus Adolph, Robert Andritschke, Andrew Aquila, Nora Berrah, et al. Ultra-efficient ionization of heavy atoms by intense x-ray free-electron laser pulses. *Nature photonics*, 6(12):858–865, 2012.

[178] Daniela Rupp, Marcus Adolph, Tais Gorkhover, Sebastian Schorb, David Wolter, Robert Hartmann, Nils Kimmel, Christian Reich, Torsten Feigl, Antonio RB de Castro, et al. Identification of twinned gas phase clusters by single-shot scattering with intense soft x-ray pulses. *New Journal of Physics*, 14(5):055016, 2012.

[179] Daniela Rupp, Marcus Adolph, Leonie Flückiger, Tais Gorkhover, Jan Philippe Müller, Maria Müller, Mario Sauppe, David Wolter, Sebastian Schorb, Rolf Treusch, Christoph Bostedt, and Thomas Möller. Generation and structure of extremely large clusters in pulsed jets. *J. Chem. Phys.*, 141 (4):044306, jul 2014. ISSN 00219606. doi: 10.1063/1.4890323. URL `http://scitation.aip.org/content/aip/journal/jcp/141/4/10.1063/1.4890323` `http://aip.scitation.org/doi/10.1063/1.4890323`.

[180] Daniela Rupp, Leonie Flückiger, Marcus Adolph, Tais Gorkhover, Maria Krikunova, Jan Philippe Müller, Maria Müller, Tim Oelze, Yevheniy Ovcharenko, Benjamin Röben, et al. Recombination-enhanced surface expansion of clusters in intense soft x-ray laser pulses. *Physical review letters*, 117(15):153401, 2016.

[181] Daniela Rupp, Nils Monserud, Bruno Langbehn, Mario Sauppe, Julian Zimmermann, Yevheniy Ovcharenko, Thomas Möller, Fabio Frassetto, Luca Poletto, Andrea Trabattoni, et al. Coherent diffractive imaging of single helium nanodroplets with a high harmonic generation source. *Nature communications*, 8(1):1–7, 2017.

[182] Daniela Rupp, Leonie Flückiger, Marcus Adolph, Alessandro Colombo, Tais Gorkhover, Marion Harmand, Maria Krikunova, Jan Philippe Müller, Tim Oelze, Yevheniy Ovcharenko, et al. Imaging plasma formation in isolated nanoparticles with ultrafast resonant scattering. *Structural Dynamics*, 7(3):034303, 2020.

[183] U Saalmann, Ch Siedschlag, and JM Rost. Mechanisms of cluster ionization in strong laser pulses. *Journal of Physics B: Atomic, Molecular and Optical Physics*, 39(4):R39, 2006.

[184] Ulf Saalmann and Jan-Michael Rost. Ionization of clusters in strong x-ray laser pulses. *Physical review letters*, 89(14):143401, 2002.

[185] Catherine A Saladrigas, Alexandra J Feinberg, Michael P Ziemkiewicz, Camila Bacellar, Maximilian Bucher, Charles Bernando, Sebastian Carron, Adam S Chatterley, Franz-Josef Decker, Ken R Ferguson, et al. Charging and ion ejection dynamics of large helium nanodroplets exposed to intense femtosecond soft x-ray pulses. *The European Physical Journal Special Topics*, 230(23):4011–4023, 2021.

[186] Carlos Sanchez-Cano, Ramon A Alvarez-Puebla, John M Abendroth, Tobias Beck, Robert Blick, Yuan Cao, Frank Caruso, Indranath Chakraborty, Henry N Chapman, Chunying Chen, et al. X-ray-based techniques to study the nano–bio interface. *ACS nano*, 15(3):3754–3807, 2021.

[187] Katharina Sander, Christian Peltz, Charles Varin, Stefan Scheel, Thomas Brabec, and Thomas Fennel. Influence of wavelength and pulse duration on single-shot x-ray diffraction patterns from nonspherical nanoparticles. *Journal of Physics B: Atomic, Molecular and Optical Physics*, 48(20):204004, 2015.

[188] Robin Santra and Chris H Greene. Xenon clusters in intense vuv laser fields. *Physical review letters*, 91(23):233401, 2003.

[189] Mario Sauppe, Andre A Haddad, Alessandro Colombo, Linos Hecht, Gregor Knopp, Katharina Kolatzki, Bruno Langbehn, Caner Polat, Kirsten Schnorr, Zhibin Sun, Paul Tümmler, Frederic Ussling, Simon Wächter, Alex Weitnauer, Julian Zimmermann, Maha Zuod, Thomas Möller, Christoph Bostedt, and Daniela Rupp. Imaging the morphology of rare gas clusters. URL `https://www.dpg-verhandlungen.de/year/2023/conference/samop/part/a/session/27/cont`

[190] Mario Sauppe, Thomas Moeller, and Daniela Rupp. Zeitaufgelöste dynamik von clustern in intensiven extrem ultravioletten doppelpulsen; time-resolved dynamics of clusters in intense extreme ultraviolet double-pulses. Technical report, DESY-DOOR, 2020.

[191] Evgeny Savelyev, Rebecca Boll, Cédric Bomme, Nora Schirmel, Harald Redlin, Benjamin Erk, Stefan Düsterer, Erland Müller, Hauke Höppner, Sven Toleikis, et al. Jitter-correction for ir/uv-xuv pump-probe experiments at the flash free-electron laser. *New Journal of Physics*, 19(4):043009, 2017.

[192] David Sayre. Some implications of a theorem due to shannon. *Acta Crystallographica*, 5(6):843–843, 1952.

[193] Jochen R Schneider. Flash—from accelerator test facility to the first single-pass soft x-ray free-electron laser. *Journal of Physics B: Atomic, Molecular and Optical Physics*, 43(19):194001, 2010.

[194] Sebastian Schorb, Daniela Rupp, Michelle L Swiggers, Ryan N Coffee, Marc Messerschmidt, Garth Williams, John D Bozek, Shin-Ichi Wada, Oleg Kornilov, Thomas Möller, et al. Size-dependent ultrafast ionization dynamics of nanoscale samples in intense femtosecond x-ray free-electron-laser pulses. *Physical Review Letters*, 108 (23):233401, 2012.

[195] L Schroedter, Maria Müller, A Kickermann, Andreas Przystawik, Sven Toleikis, Marcus Adolph, Leonie Flückiger, Tais Gorkhover, Lena Nösel, Maria Krikunova, et al. Hidden charge states in soft-x-ray laser-produced nanoplasmas revealed by fluorescence spectroscopy. *Physical review letters*, 112(18):183401, 2014.

[196] B Schütte, M Arbeiter, Th Fennel, Marc JJ Vrakking, and Arnaud Rouzée. Rare-gas clusters in intense extreme-ultraviolet pulses from a high-order harmonic source. *Physical review letters*, 112(7):073003, 2014.

[197] B Schütte, Filippo Campi, M Arbeiter, Th Fennel, MJJ Vrakking, and Arnaud Rouzée. Tracing electron-ion recombination in nanoplasmas produced by extreme-ultraviolet irradiation of rare-gas clusters. *Physical review letters*, 112(25):253401, 2014.

[198] Bernd Schütte, Tim Oelze, Maria Krikunova, Mathias Arbeiter, Thomas Fennel, Marc JJ Vrakking, and Arnaud Rouzée. Recombination dynamics of clusters in intense extreme-ultraviolet and near-infrared fields. *New Journal of Physics*, 17(3): 033043, 2015.

[199] Giacinto Scoles. *Atomic and molecular beam methods*. Oxford university press, 1988.

[200] EA Seddon, JA Clarke, DJ Dunning, C Masciovecchio, CJ Milne, F Parmigiani, D Rugg, JCH Spence, NR Thompson, K Ueda, et al. Short-wavelength free-electron laser sources and science: a review. *Reports on Progress in Physics*, 80(11):115901, 2017.

[201] M Marvin Seibert, Tomas Ekeberg, Filipe RNC Maia, Martin Svenda, Jakob Andreasson, Olof Jönsson, Duško Odić, Bianca Iwan, Andrea Rocker, Daniel Westphal, et al. Single mimivirus particles intercepted and imaged with an x-ray laser. *Nature*, 470(7332):78–81, 2011.

[202] P G_ Self, MA O'keefe, P_R Buseck, and AEC Spargo. Practical computation of amplitudes and phases in electron diffraction. *Ultramicroscopy*, 11(1):35–52, 1983.

[203] Jonas A Sellberg, C Huang, Trevor A McQueen, ND Loh, Hartawan Laksmono, Daniel Schlesinger, RG Sierra, Dennis Nordlund, CY Hampton, Dmitri Starodub, et al. Ultrafast x-ray probing of water structure below the homogeneous ice nucleation temperature. *Nature*, 510(7505):381–384, 2014.

[204] Björn Senfftleben. *Coherent diffractive imaging of electron dynamics in the attosecond domain*. Technische Universitaet Berlin (Germany), 2023.

[205] Björn Senfftleben, Martin Kretschmar, Andreas Hoffmann, Mario Sauppe, Johannes Tümmler, Ingo Will, Tamás Nagy, Marc JJ Vrakking, Daniela Rupp, and Bernd Schütte. Highly non-linear ionization of atoms induced by intense high-harmonic pulses. *Journal of Physics: Photonics*, 2(3):034001, 2020.

[206] Svitozar Serkez, Winfried Decking, Lars Froehlich, Natalia Gerasimova, Jan Grünert, Marc Guetg, Marko Huttula, Suren Karabekyan, Andreas Koch, Vitali Kocharyan, et al. Opportunities for two-color experiments in the soft x-ray regime at the european xfel. *Applied Sciences*, 10(8):2728, 2020.

[207] Yoav Shechtman, Yonina C Eldar, Oren Cohen, Henry Nicholas Chapman, Jianwei Miao, and Mordechai Segev. Phase retrieval with application to optical imaging: a contemporary overview. *IEEE signal processing magazine*, 32(3):87–109, 2015.

[208] Christian Siedschlag and Jan-Michael Rost. Small rare-gas clusters in soft x-ray pulses. *Physical review letters*, 93(4):043402, 2004.

[209] Alkwin Slenczka and Jan Peter Toennies. *Molecules in Superfluid Helium Nanodroplets: Spectroscopy, Structure, and Dynamics*. Springer Nature, 2022.

[210] JM Soler, N Garcia, Olof Echt, K Sattler, and Ekkehard Recknagel. Microcluster growth: transition from successive monomer addition to coagulation. *Physical Review Letters*, 49(25):1857, 1982.

[211] AA Sorokin, SV Bobashev, T Feigl, K Tiedtke, H Wabnitz, and Mathias Richter. Photoelectric effect at ultrahigh intensities. *Physical review letters*, 99(21):213002, 2007.

[212] JCH Spence. Xfels for structure and dynamics in biology. *IUCrJ*, 4(4):322–339, 2017.

[213] John CH Spence. Outrunning damage: Electrons vs x-rays—timescales and mechanisms. *Structural dynamics*, 4(4):044027, 2017.

[214] Lothar Strüder, Sascha Epp, Daniel Rolles, Robert Hartmann, Peter Holl, Gerhard Lutz, Heike Soltau, Rouven Eckart, Christian Reich, Klaus Heinzinger, et al. Large-format, high-speed, x-ray pnccds combined with electron and ion imaging spectrometers in a multipurpose chamber for experiments at 4th generation light sources. *Nuclear Instruments and Methods in Physics Research Section A: Accelerators, Spectrometers, Detectors and Associated Equipment*, 614(3):483–496, 2010.

[215] Zhibin Sun, Andre Al Haddad, Sven Augustin, Gregor Knopp, Jonas Knurr, Kirsten Schnorr, and Christoph Bostedt. Ultrafast single-particle imaging with intense x-ray pulses. *Chimia*, 76(6):529–529, 2022.

[216] T Tachibana, Z Jurek, H Fukuzawa, K Motomura, K Nagaya, S Wada, Per Johnsson, M Siano, S Mondal, Y Ito, et al. Nanoplasma formation by high intensity hard x-rays. *Scientific reports*, 5(1):10977, 2015.

[217] Allen Taflove. Application of the finite-difference time-domain method to sinusoidal steady-state electromagnetic-penetration problems. *IEEE Transactions on electromagnetic compatibility*, (3):191–202, 1980.

[218] Rico Mayro P. Tanyag, Charles Bernando, Curtis F. Jones, Camila Bacellar, Ken R. Ferguson, Denis Anielski, Rebecca Boll, Sebastian Carron, James P. Cryan, Lars Englert, Sascha W. Epp, Benjamin Erk, Lutz Foucar, Luis F. Gomez, Robert Hartmann, Daniel M. Neumark, Daniel Rolles, Benedikt Rudek, Artem Rudenko, Katrin R. Siefermann, Joachim Ullrich, Fabian Weise, Christoph Bostedt, Oliver Gessner, and Andrey F. Vilesov. Communication: X-ray coherent diffractive imaging by immersion in nanodroplets. *Structural Dynamics*, 2(5), 10 2015. ISSN 2329-7778. doi: 10.1063/1.4933297. URL `https://doi.org/10.1063/1.4933297`. 051102.

[219] Rico Mayro P Tanyag, Camila Bacellar, Weiwu Pang, Charles Bernando, Luis F Gomez, Curtis F Jones, Ken R Ferguson, Justin Kwok, Denis Anielski, Ali Belkacem, et al. Sizes of pure and doped helium droplets from single shot x-ray imaging. *The Journal of chemical physics*, 156(4):041102, 2022.

[220] Rico Mayro P Tanyag, Bruno Langbehn, Thomas Möller, and Daniela Rupp. X-ray and xuv imaging of helium nanodroplets. In *Molecules in Superfluid Helium Nanodroplets: Spectroscopy, Structure, and Dynamics*, pages 281–341. Springer International Publishing Cham, 2022.

[221] R.M.P Tanyag, D. Rupp, A. Ulmer, A. Heilrath, B. Senfftleben, B. Kruse, L. Seiffert, S.M.O. O'Connell, K. Kolatzki, B. Langbehn, A. Hoffmann, T. Baumann, R. Boll, A. Chatterley, A. de Fanis, B. Erk, S. Erukala, A.J. Feinberg, T. Fennel, P. Grychtol, R. Hartmann, S. Hauf, M. Ilchen, M. Izquierdo, B. Krebs, M. Kuster, T. Mazza, K.H. Meiwes-Broer, J. Montaño, G. Noffz, D. Rivas, D. Schlosser, F. Seel, H. Stapelfeldt, L. Strüder, J. Tiggesbäumker, H. Yousef, M. Zabel, P. Ziolkowski, A. Vilesov, M. Meyer, Y. Ovcharenko, and T. Möller. *European XFEL 10th Anniversary Annual Report 2019, p. 20, Taking snapshots of nanostructures in superfluid helium droplets*. European XFEL GmbH, 2019.

[222] Pierre Thibault and Veit Elser. X-ray diffraction microscopy. *Annu. Rev. Condens. Matter Phys.*, 1(1):237–255, 2010.

[223] Pierre Thibault, Veit Elser, Chris Jacobsen, David Shapiro, and David Sayre. Reconstruction of a yeast cell from x-ray diffraction data. *Acta Crystallographica Section A: Foundations of Crystallography*, 62(4):248–261, 2006.

[224] H Thomas, C Bostedt, M Hoener, E Eremina, H Wabnitz, T Laarmann, E Plönjes, R Treusch, ARB De Castro, and T Möller. Shell explosion and core expansion of xenon clusters irradiated with intense femtosecond soft x-ray pulses. *Journal of Physics B: Atomic, Molecular and Optical Physics*, 42(13):134018, 2009.

[225] Heiko Thomas, Ahmed Helal, Kay Hoffmann, Nirmala Kandadai, John Keto, Jakob Andreasson, Bianca Iwan, Marvin Seibert, Nicusor Timneanu, Janos Hajdu, et al. Explosions of xenon clusters in ultraintense femtosecond x-ray pulses from the lcls free electron laser. *Physical review letters*, 108(13):133401, 2012.

[226] Paul Tuemmler, Björn Kruse, Christian Peltz, and Thomas Fennel. Efficient and accurate simulation of wide-angle single-shot scattering. URL `https://www.dpg-verhandlungen.de/year/2023/conference/samop/part/a/session/22/cont`

[227] Anatoli Ulmer, Andrea Heilrath, Björn Senfftleben, Sean MO O'Connell-Lopez, Björn Kruse, Lennart Seiffert, Katharina Kolatzki, Bruno Langbehn, Andreas Hoffmann, Thomas M Baumann, et al. Generation of large vortex-free superfluid helium nanodroplets. *arXiv preprint arXiv:2302.07355v2*, 2023.

[228] Gijs Van Der Schot, Martin Svenda, Filipe RNC Maia, Max Hantke, Daniel P DePonte, M Marvin Seibert, Andrew Aquila, Joachim Schulz, Richard Kirian, Mengning Liang, et al. Imaging single cells in a beam of live cyanobacteria with an x-ray laser. *Nature communications*, 6(1):5704, 2015.

[229] Charles Varin, Christian Peltz, Thomas Brabec, and Thomas Fennel. Attosecond plasma wave dynamics in laser-driven cluster nanoplasmas. *Physical review letters*, 108(17):175007, 2012.

[230] Deepak Verma, Sean MO O'Connell, Alexandra J Feinberg, Swetha Erukala, Rico Mayro P Tanyag, Charles Bernando, Weiwu Pang, Catherine A Saladrigas, Benjamin W Toulson, Mario Borgwardt, et al. Shapes of rotating normal fluid he 3 versus superfluid he 4 droplets in molecular beams. *Physical Review B*, 102(1): 014504, 2020.

[231] Alexander Volk, Philipp Thaler, Markus Koch, Evelin Fisslthaler, Werner Grogger, and Wolfgang E Ernst. High resolution electron microscopy of ag-clusters in crystalline and non-crystalline morphologies grown inside superfluid helium nanodroplets. *The Journal of chemical physics*, 138(21):214312, 2013.

[232] H Wabnitz, ARB De Castro, P Gürtler, T Laarmann, W Laasch, J Schulz, and T Möller. Multiple ionization of rare gas atoms irradiated with intense vuv radiation. *Physical review letters*, 94(2):023001, 2005.

[233] Hubertus Wabnitz, L Bittner, ARB De Castro, R Döhrmann, P Gürtler, T Laarmann, W Laasch, J Schulz, A Swiderski, K Von Haeften, et al. Multiple ionization of atom clusters by intense soft x-rays from a free-electron laser. *Nature*, 420(6915): 482–485, 2002.

[234] Ge Wang, Hengyong Yu, Wenxiang Cong, and Alexander Katsevich. Non-uniqueness and instability of 'ankylography'. *Nature*, 480(7375):E2–E3, 2011.

[235] Max O Wiedorn, Dominik Oberthür, Richard Bean, Robin Schubert, Nadine Werner, Brian Abbey, Martin Aepfelbacher, Luigi Adriano, Aschkan Allahgholi, Nasser Al-Qudami, et al. Megahertz serial crystallography. *Nature communications*, 9(1):4025, 2018.

[236] Stefan Witte, Vasco T Tenner, Daniel WE Noom, and Kjeld SE Eikema. Lensless diffractive imaging with ultra-broadband table-top sources: from infrared to extreme-ultraviolet wavelengths. *Light: Science & Applications*, 3(3):e163–e163, 2014.

[237] Longlong Wu, Shinjae Yoo, Ana F Suzana, Tadesse A Assefa, Jiecheng Diao, Ross J Harder, Wonsuk Cha, and Ian K Robinson. Three-dimensional coherent x-ray diffraction imaging via deep convolutional neural networks. *npj Computational Materials*, 7(1):175, 2021.

[238] M Yabashi, H Tanaka, T Tanaka, H Tomizawa, T Togashi, M Nagasono, T Ishikawa, JR Harries, Y Hikosaka, A Hishikawa, et al. Compact xfel and amo sciences: Sacla and scss. *Journal of Physics B: Atomic, Molecular and Optical Physics*, 46(16): 164001, 2013.

[239] Makina Yabashi, Kenji Tamasaku, Kei Sawada, Shunji Goto, and Tetsuya Ishikawa. Perfect crystal optics. *Synchrotron Light Sources and Free-Electron Lasers: Accelerator Physics, Instrumentation and Science Applications*, pages 1123–1159, 2020.

[240] Chun Hong Yoon, Peter Schwander, Chantal Abergel, Inger Andersson, Jakob Andreasson, Andrew Aquila, Saša Bajt, Miriam Barthelmess, Anton Barty, Michael J Bogan, et al. Unsupervised classification of single-particle x-ray diffraction snapshots by spectral clustering. *Optics express*, 19(17):16542–16549, 2011.

[241] B Ziaja, H Wabnitz, F Wang, E Weckert, and T Möller. Energetics, ionization, and expansion dynamics of atomic clusters irradiated with short intense vacuum-ultraviolet pulses. *Physical Review Letters*, 102(20):205002, 2009.

[242] Beata Ziaja, HN Chapman, R Santra, T Laarmann, E Weckert, C Bostedt, and T Möller. Heterogeneous clusters as a model system for the study of ionization dynamics within tampered samples. *Physical Review A*, 84(3):033201, 2011.

[243] Julian Zimmermann, Bruno Langbehn, Riccardo Cucini, Michele Di Fraia, Paola Finetti, Aaron C LaForge, Toshiyuki Nishiyama, Yevheniy Ovcharenko, Paolo Piseri, Oksana Plekan, et al. Deep neural networks for classifying complex features in diffraction images. *Physical Review E*, 99(6):063309, 2019.

[244] Julian Zimmermann, Fabien Beguet, Daniel Guthruf, Bruno Langbehn, and Daniela Rupp. Finding the semantic similarity in single-particle diffraction images using self-supervised contrastive projection learning. *npj Computational Materials*, 9(1):24, 2023.

[245] Julian Claudius Zimmermann. *Probing Ultrafast Electron Dynamics in Helium Nanodroplets with Deep Learning Assisted Diffraction Imaging*. Technische Universitaet Berlin (Germany), 2021.